INSTITUTO POLITÉCNICO DE LISBOA

Instituto Superior de Engenharia de Lisboa

Escola Superior de Tecnologia da Saúde de Lisboa

Dosimetrical studies for error acceptance in FLASH proton therapy

An MCNPX study

Jéssica Mestre Correia

Master's Final Work for obtaining the degree of Master of Science in Biomedical Engineering

Supervised by:

Professor Doutor Pedro Ferreira (Instituto Superior de Engenharia de Lisboa)

Doctor Rudi Labarbe (Ion Beam Application, Belgium)

January 2022

INSTITUTO POLITÉCNICO DE LISBOA

Instituto Superior de Engenharia de Lisboa

Escola Superior de Tecnologia da Saúde de Lisboa

Dosimetrical studies for error acceptance in FLASH proton therapy

An MCNPX study

Jéssica Mestre Correia

Master's Final Work for obtaining the degree of Master of Science in Biomedical Engineering

Supervised by:

Professor Doutor Pedro Ferreira (Instituto Superior de Engenharia de Lisboa)

Doctor Rudi Labarbe (Ion Beam Application, Belgium)

Juri:

President Professor Doutor António Silvestre (Instituto Superior de Engenharia de Lisboa)

Vogal Professor Doctor Sylvain Deffet (Université Catholique de Louvain, Belgium)

January 2022

Acknowledgments

This work wouldn't have been possible without the support of Professor Pedro Ferreira. I had the luck of having excellent Professors in my academic path and Professor Pedro Ferreira was a remarkable one. Would like to thank all the support, the shared knowledge, interest, and high demand that were key to improve this work.

To Rudi Labarbe, for his patience and kindness in answering to all the questions. I will be aways grateful for the trust, support, and guidance, always with a smile in his face.

To Lucian Hotoiu that gave me the tools for the work performed and answered to all the questions.

To Fréderic Stichelbaut, who supported me through MCNPX challenges and pointed me in the right direction at very frustrating moments. Thank you for all the patience and kindness.

To IBA, that embrace me into a passioned professional atmosphere. I was amazed to feel the cooperation between people that join their high level of expertise into developments to save someone's live.

To Sara Rosas, who helped and believed in me, without any warranties.

To José Seabra that establish the first contact point with IBA, always with a support and courage word.

To my family and friends, for the support and understanding.

To my mom, for teaching me that we can do everything we put our mind into. For always having given me the freedom to make my choices and the tools to deal with any results of it.

Last, but never least, to my fiancé, João. Who always pushed me to pursuit my dreams and follow my passion. I would never thank you enough for the support, for the reassuring comfort in weakness moments and for always walking beside me. With you, everything becomes lighter.

Resumo

A radioterapia é um tratamento que utiliza radiação ionizante para o tratamento de tumores. Entre as partículas usadas, destacam-se os protões pelo seu comportamento característico, conhecido como pico de Bragg, ao interagir com a matéria. Estas partículas permitem diminuir a dose depositada nos tecidos saudáveis adjacentes e aumentar a conformação da deposição de energia ao volume alvo da irradiação.

Nos últimos anos tem sido feito um grande esforço científico para o conhecimento e desenvolvimento da técnica terapia ultra-rápida, conhecida como terapia FLASH. Este investimento deve-se à observação de respostas diferenciadores em relação a técnicas convencionais, uma vez que foi observado em estudos pré-clinicos que os tecidos sãos reagem de uma forma diferente. As características mais promissoras desta técnica prendem-se com a observação de menores danos nos tecidos sãos adjacentes após a irradiação, em concomitância com uma eficácia anti-tumoral idêntica à conseguida com técnicas mais convencionais. No entanto, os mecanismos biológicos e celulares por detrás destas respostas permanecem incógnitos e é necessária mais pesquisa nesse âmbito.

A possibilidade de poder vir a combinar os benefícios da terapia de protões com a técnica de FLASH é extremamente promissora e o objetivo desta tese final de mestrado prende-se com o estudo dosimétrico de um dispositivo que apresenta potencialidades para a sua implementação.

O filtro de energia conformacional é uma solução de hardware apontada para a implementação desta técnica, uma vez que permite modular o feixe de protões às características do volume alvo durante uma irradiação ultra rápida (cerca de 200 mili-segundos). De forma a estudar a influência de diferentes incertezas na distribuição de dose dentro do paciente, recorreu-se a um simulador Monte Carlo, o *Monte Carlo N-particles Extended* (MCNPX). Foram simulados diversos cenários e incertezas a nível da posição do feixe, da sua angulação, de alterações na dimensão do feixe e alterações das dimensões laterais do filtro de energia conformacional. O resultado destas simulações foi comparado com uma simulação de referência e foi possível verificar que o fator que mais influencia a distribuição de dose é a translação e angulação do feixe

Uma vez que a produção de neutrões é um dos fatores a ter em conta aquando da terapia de protões, foram também simulados diversos cenários com vista a estudar os materiais para a composição do acessório e os efeitos da introdução de outros acessórios no caminho do feixe.

Palavras-chave: Radioterapia, Terapia com protões, FLASH, Filtro de energia conformacional, Neutrões.

Abstract

Radiation therapy is a treatment that uses ionizing radiation to treat tumors. Among the particles used, protons stand out for their characteristic behavior, known as Bragg peak, when interacting with matter. These particles make it possible to decrease the dose deposited on adjacent healthy tissues and increase the conformation of the energy deposition to the irradiation target volume.

In recent years a huge scientific effort has gone into the knowledge and development of the ultrafast therapy technique, known as FLASH therapy. This investment is due to the observation of differentiating responses compared to conventional techniques, since it has been observed in pre-clinical studies that healthy tissues react in a different way. The most promising features of this technique are the observation of less damage to adjacent healthy tissues after irradiation, concomitant with an anti-tumor efficacy similar to that achieved with more conventional techniques. However, the biological and cellular mechanisms behind these responses remain unknown and further research is needed.

The possibility of combining the benefits of proton therapy with the FLASH technique is extremely promising and the objective of this final master's thesis is related to the dosimetric study of a device that presents potential for its implementation.

The conformational energy filter is a hardware solution suggested for the implementation of this technique since it allows modulating the proton beam to the characteristics of the target volume during an ultra-fast irradiation (about 200 milliseconds). In order to study the influence of different uncertainties on the dose distribution inside the patient, a Monte Carlo simulator, Monte Carlo N-particles Extended (MCNPX), was used. Several scenarios and uncertainties in beam position, beam angulation, changes in beam size, and changes in the lateral dimensions of the conformal energy filter were simulated. The result of these simulations was compared with a reference simulation, and it was possible to verify that the factor that most influences the dose distribution is the beam translation and angulation.

Since the production of neutrons is one of the factors to be taken into account when performing proton therapy, several scenarios were also simulated in order to study the materials for the composition of the accessory and the effects of introducing other accessories in the beam path.

Keywords: Radiotherapy, Proton Therapy, FLASH, Conformal Energy Filter, Neutrons.

Contest

Figure content

Table content

List of abbreviations

2D	Bi-dimensional
3D	Tri-dimensional
CEF	Conformal energy filter
CSDA	Continuous-slowing-down approximation
CT	Computed Tomography
CTV	Clinical target volume
DVH	Dose- volume histogram
FLASH	ultra-high dose rates radiotherapy
FWHM	Full width at half maximum
GTV	Gross Tumor Volume
IMRT	Intensity modulated radiation therapy
INC	Intra-nuclear cascade
INP	Input
ITV	Internal target volume
LET	Linear energy transfer
MCS	Multiple Coulomb Scattering
MCNPX	Monte Carlo N-particles Extended
MeV	Mega electron-volt
NTCP	Normal tissue complication probability
OAR	Organs at risk
PET	Positron Emission Tomography
PTR	Proton therapy
PTV	Planning target volume
PTCOG	Particle Therapy Co-Operative Group
PRV	Planning organs at risk volume
R	Range
RS	Range Shifter
RT	Radiation therapy
SOBP	Spread-out Bragg peak
TCP	Tumor control probability
TPS	Treatment Planning System
TV	Target volume

1. Introduction

Radiation therapy (RT) is a therapeutic modality that uses ionizing radiation to irradiate volumes of interest inside the patient. Those volumes are mainly tumor locations, and RT can be used in combination with other treatment modalities such as surgery and chemotherapy, according to an individual clinical treatment plan. RT can be administered by internal or external sources, the last one being the most common. The most used particles are electrons and photons, administered externally by a linear accelerator. Ionizing ions are also used, in a modality known as *hadron therapy*, which uses hadrons, such as neutrons, protons, light ions and heavy ions (e.g. carbon ion). (1)

The success of RT is interconnected to the ability to maximize tumor control and limit the toxicity at normal healthy tissues. To achieve this goal, the behavior of the particles when interacting to the human body is of paramount importance.

With photon beams, the maximum dose deposition is located at superficial depth in the patient, which results in bigger dose distributions at the organs at risk (OAR) for deep seated tumor treatments. The protons are heavy charged particles and suffer different interactions with matter, comparatively to photons, resulting in different dose distributions. It is reported that proton therapy (PTR) reduces the total energy deposited in the patient by a factor of 2 to 3 compared to photon therapy.(2) The type of interactions experienced by protons are similar to those of electrons but, because of their largely superior mass, the resultant dose distributions are also quite different.(3)

The characteristic proton depth dose curve is named Bragg peak and presents a short dose build-up followed by an exponential-like decay of dose distribution, and this can produce a significant reduction in normal tissue doses proximal and distal to the target volume. The proton beam needs to be spread out laterally and longitudinally, known as Spread-out Bragg peak (SOBP), to have dimension to cover the tumor volume. This characteristic behavior allow escalation of doses in the tumor and bigger sparing of normal tissues, leading to improved local control and significant reduction in early and late side effects, comparatively to photons. (2,4)

Statistics show that, in the United States, 50% of patients receive RT during their cancer treatment and approximately 65% of adults and 80% of children survive 5 years after their diagnosis.(5) There are also a large number of treatment-related morbidities related in the literature and, with the projections pointing to the increase of the number of cancer survivals, the interest of using irradiation techniques that diminish the dose in normal healthy tissues has an extreme importance. (6,7)

The children's group receive particular attention since they are more susceptible to late adverse effects of RT, due to their longer-life expectancy. One of the possible late effects of RT is the risk of radiation induced secondary cancers.(8) Regarding the reduction of dose in normal tissue using PTR and, therefore, the potential for reduction in adverse effects, this treatment modality is often employed in pediatric treatments. A series of publications suggest that PTR is comparable to photon therapy in terms of disease control and survival rates.(4) Some of the anatomical locations where PTR is consolidated are skull based or sino-nasal malignancies and brain tumors. (4)

According to the Particle Therapy Co-Operative Group (PTCOG), in April 2021, there were 99 proton therapy facilities in clinical operation and 31 under construction, in the whole world.(9,10) The availability of PTR centers is inferior to photon therapy due to the high costs of equipment and maintenance, technical difficulty, and lack of evidence of cost-competitiveness.(7,11) Due to this, many institutions prefer to use much more mature techniques as photon intensity modulated radiation therapy (IMRT) and volumetric arc therapies.

The ultra-high dose rates radiotherapy (FLASH-RT) has been largely investigated in the last years due to the possible ability to spare normal healthy tissues during the irradiation. This modality is characterized by delivering an ultra-high dose rate, superior to 40 Gy/s. This makes the irradiation times much shorter than conventional irradiations since the irradiations take about 0.1 seconds. These short irradiation times raise the possibility of diminishing the treatment margins, since the uncertainties caused by intra-fraction motion are minimized, resulting in smaller volumes of normal tissue irradiated. Several studies in animals and cell cultures have been conducted in the last decade and the majority shows that FLASH-RT could reduce radiation-induced damage in healthy tissues, while maintaining the same anti-tumoral control levels.(12–14) Besides the potential advantages, the principle behind the FLASH effect remains unclear and need further investigation. Along with this, most of the study results are from the utilization of electron beams. Nevertheless, the studies with FLASH proton beams start to arise and highlight the same results as previous studies.

Simeonov et al. (15) proposed the utilization of a non-Uniform ridge filter (also called Conformal Energy Filter (CEF) or "hedgehog") to produce depth modulation. This approach has been tested and Patriarca et al. (16) confirmed by measurements that a ridge filter could be used to investigate possible FLASH effects in SOBP regions.

To study the behavior of the radiation when interacting with the human tissues, it is usual to appeal to computational models. Those help to have a comprehension about the interaction mechanisms in the different tissues and secondary particles produced, with high confidence level. The anatomical, physical, or computational models are known as phantoms. When dealing with

physical phantoms, it is possible to obtain a direct measurement, using diodes to measure the radiation dose administrated. The computational phantoms can also simulate the characteristics of the human body and predict the measurements, by Monte Carlo simulations. For this, it is important to specify accurate characteristics of the different tissues in the human body and the beamline.

The aim of this work is to study the impact of different errors in the dose deposition, when using a CEF to administer FLASH. For this, an assembly on MCNPX was designed and the impact on dose distribution of different induced error factors were studied in a simulated water phantom.

Those errors included a beam translation, relative to the assembly axis, different possible beam angulations, differences in the CEF density, errors in the beam width estimation and errors in the lateral dimensions of the CEF. Those errors were considered since they can arise from the CEF production phase or during the treatment. It is important to understand their impact on dose distributions since the FLASH irradiation happens in a very short period and is a hypofractionation technique, meaning that the doses administered by fraction are very high and the total number of treatments is shorter than that of conventional techniques. Thus, even minute uncertainties in the beam parameters, its position, and the composition of the materials in the beam path may cause huge variations in the deposited dose.

This work is divided in twelve chapters. The first chapter is the introduction, where a short theoretical introduction about the thesis subject is presented and where the objectives of the work are presented.

The second chapter contains the theoretical background about proton interactions with matter, including the creation of secondary particles. In this chapter we also present and explain the physical quantities used to describe the radiation and its effects on the human body.

The third chapter we explain the concept of this therapeutic modality, the different phases of treatment preparation and the comparison of the effects of different physical particles in treatment. We introduce the concept of FLASH therapy and the bibliography and developments that sustains the research in this area.

The fourth chapter explains the production of the protons beams and the machinery that is necessary to produce and conduct the beam to the treatment room.

The fifth chapter presents the evolution of the techniques used nowadays in proton therapy facilities. In this chapter we also present the advantages and disadvantages of each and their role in modern proton radiation therapy.

The sixth chapter introduces the tool used to develop this work, MCNPX. This is a Monte Carlo simulator and the theory behind these methods is described and the workflow process in MCNPX.

The seventh chapter contains general information about the characteristic profile of dose deposition of the protons in the medium. In this chapter, the lateral scattering of the dose distribution and the interaction of this particle beam with homogeneous and inhomogeneous mediums are also studied.

In the eight chapter the parameters and components used to perform the simulations are presented.

The ninth chapter contains the results of all simulations performed with MCNPX. Here there are shown the simulation results and their comparison with reference situations and the discussion of the results, for each scenario presented.

The tenth chapter we address the neutron doses obtained. In this chapter, we present the theoretical bases behind this subject and their importance in proton radiation therapy. Several simulations to study the influence of neutron doses in the dose distribution are performed.

The eleventh chapter is where we present our conclusions and contains the compilation of all simulation results and a discussion about them, as well as a comparison to the most relevant bibliography available.

The twelfth chapter contains a list of all bibliography used in the present work.

2. Protons fundamental concepts

In this chapter there will be introduced the basic concepts behind protons interaction with matter, characteristically behaviour and energy loss. There are also presented the principal quantities used, such as absorbed dose and effective dose.

2.1. Proton interactions in matter

The protons interact with matter by Coulomb interactions with atomic electrons, Coulomb interactions with the atomic nucleus, and via nuclear reactions with atomic nuclei.

Figure 1 presents a schematic illustration of proton interaction mechanisms: (a) energy loss via inelastic Coulomb interactions (ionization and excitation of the electrons), (b) deflection of proton trajectory by repulsive Coulomb elastic scattering with nucleus (multiple Coulomb scattering), (c) removal of primary proton and creation of secondary particles via non-elastic nuclear interaction .(7)

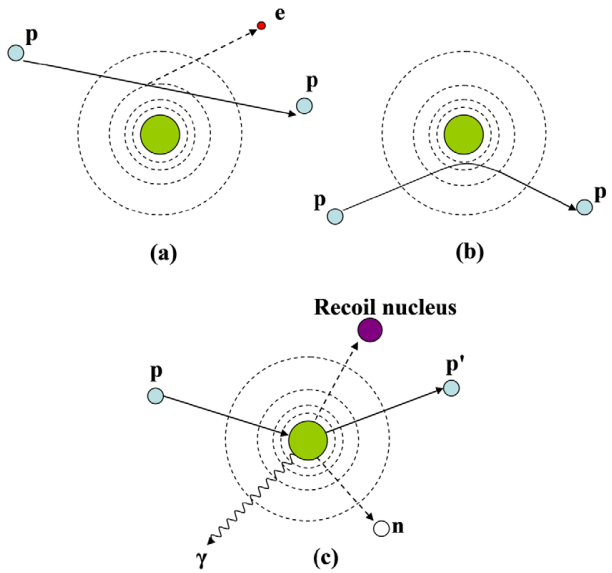

Figure 1 Schematic illustration of proton interaction mechanisms. p: proton, e: electron, n: neutron, γ: gamma rays(7)

The most frequent event is the continuous loss of proton kinetic energy by inelastic Coulomb interactions with atomic electrons. Most protons travel in a nearly straight line because their rest mass is about 1800 times bigger than the electron rest mass. (7) The secondary electrons (also known as “delta rays”) travel very short distances from the path of the proton while ionizing and depositing energy.

In a uniform medium, monoenergetic protons travel a well-defined distance, losing energy at an increasing rate as they slow down, before coming to a stop, leading to creation of the Bragg curve. (4)

2.1.1. Energy loss rate

The protons mainly lose their kinetic energy through electromagnetic Coulomb interactions with the orbiting electrons of the atoms in the medium. These interactions produce secondary electrons that deposit their energy locally (typically, ≤10 keV). The rate of energy loss by protons is approximately proportional to the inverse square of the proton velocity and increases with the penetration depth. (17)

The linear stopping power (S) is the rate of energy loss per unit path length (dE/dx) of the charged particles and the SI unit is MeV/cm. Usually, it is expressed in a way that is independent of the mass density, known as the mass stopping power:

$$\frac{S}{\rho} = -\frac{dE}{\rho dx}, \tag{2.1}$$

where ρ is the mass density of the absorbing material.

This phenomenon can be defined by several mathematical formulas, the Bethe-Bloch approach being the most accepted. It involves relativistic theory and quantum mechanics, which needs to be considered both for very low or very high proton energies. The equation is given by:

$$\frac{S}{\rho} = -\frac{dE}{\rho dx} = 4\pi N_A r_e^2 m_e c^2 \frac{Z}{A}\frac{z^2}{\beta^2}\left[ln\frac{2m_e c^2\gamma^2\beta^2}{I} - \beta^2 - \frac{\delta}{2} - \frac{C}{Z}\right], \tag{2.2}$$

where ρ is the mass density of the absorbing material, N_A is Avogadro's number, r_e is the classical electron radius, m_e is the mass of an electron, z is the charge of the projectile in units of the elementary electric charge, Z is the atomic number of the absorbing material, A is the atomic weight of the absorbing material, c is the speed of light, $\beta = \frac{v}{c}$, where v is the velocity of the projectile, $\gamma = (1-\beta^2)^{-1/2}$, I is the mean excitation potential of the absorbing material, δ is a density correction arising from the shielding of remote electrons by close electrons and will result in a reduction of energy loss at higher energies, and C is the shell correction term, which is important only for low energies where the particle velocity is near the velocity of the atomic electrons.

It can be seen that the energy loss is proportional to the inverse square of its velocity and the square of the ion charge ($z = 1$, for protons), and there is no dependence on projectile mass. This equation also reveals that the absorber material can highly influence the energy loss rate, since the linear stopping power is directly proportional to the density of electrons in the absorber ($N_A \rho Z/A$), because the energy loss occurs by Coulomb interactions between the proton and atomic electrons.

The density of the human body can vary by about three orders of magnitude, from air in the lung to cortical bone, and the velocity of protons can cause the value of S in water to vary by about a factor of 60 for proton energies between 1 and 250 MeV. In proton therapy, water is considered an excellent tissue substitute because of its similar density, effective Z/A, and other properties. Furthermore, proton energy loss and residual range in various materials are often expressed in terms of their water-equivalent values. (7)

2.1.2. Multiple coulomb scattering

A proton that passes close to one atomic nucleus experiences a repulsive elastic Coulomb interaction resulting from the positive charge of the nucleus. (7) Despite a small deflection, the accumulation of these events can lead to statistical significant lateral spreading of the protons. (4) The resultant scattering is named Multiple Coulomb Scattering (MCS).

In proton therapy, MCS in the treatment head (e.g., in the scattering foils) is helpful because it allows the beam to be spread laterally and create uniform dose distributions in the target. This effect is used often in passive scattering techniques, where the scattering foils in the nozzle are designed to make use of MCS and energy loss to produce clinically useful beams. However, MCS in the treatment head and in the patient blur the sharpness of lateral penumbra, and lead to a penumbral growth at the edge of collimated beams and/or the growth of the lateral spot size of a scanned beam. Understanding and preserving penumbral sharpness is key to realizing the full benefit of proton therapy for sparing healthy tissue. (7)

Some studies have highlighted that MCS has a high influence in proton dose distribution around implanted fiducial markers, used for image guided patient alignment. Beside their small dimensions (less than 1 mm), they can be responsible for creating areas of high dose and under dose in the tumor and compromise the target coverage. (7,18)

2.1.3. Nuclear interactions

Comparatively to others proton reactions presented before, nuclear interactions can occur, but they are much less frequent. This occurs because the cross sections for proton-nucleus

reactions are much smaller than that of Coulomb scattering. This can also be understood geometrically, since the nuclei are much smaller than the atoms and thus a beam of protons interacts mainly with the electrons. In these reactions, the primary proton transmits a large fraction of its energy to the nucleus and may scatter through a large angle. In a proton beam, all the primary particles are protons. After these primary particles suffer nuclear interactions, they can originate secondaries particles, as result from elastic or non-elastic nuclear reactions.

Elastic reactions occur when the incident projectile scatters of the target nucleus and the total kinetic energy is conserved, which means that the internal state of the target nucleus and the projectile remains unchanged by the reaction.(19) An example is the following reaction between a proton (p) and oxygen-16 ($^{16}_{8}O$) nucleus which results in the same particles that we have initially.

$$p + {}^{16}_{8}O \rightarrow p + {}^{16}_{8}O \tag{2.3}$$

In non-elastic scattering, there is no conservation of kinetic energy, meaning that the target nucleus absorbs some of the energy. This can originate different types of secondary events such as disintegration, excitation to a higher quantum state or particle transfer reactions. (4) In a nuclear reaction, the projectile proton enters the nucleus and this may cause the emission of a proton, deuteron, triton, or heavier ion, or one or more neutrons. (7) It is estimated that as many as 20% of protons of the highest energies in the therapeutic range undergo nuclear interactions along their path. An example of this reaction is the following, where a proton interacts with oxygen-16 and create a proton and nitrogen (^{15}N).

$$p + {}^{16}_{8}O \rightarrow p + {}^{15}_{7}N + p \tag{2.4}$$

Proton Bremsstrahlung is theoretically possible but, at therapeutic proton beam energies (of the order of MeV), the effect is negligible. (7) The protons emit a spectrum of photons when passing in the field of an atomic nucleus and get lateral acceleration from those interactions. The probability of Bremsstrahlung is proportional to the inverse of the square of the particle mass and, as the proton mass is very high, proton bremsstrahlung has no clinical significance. (3)

It is important to consider these interactions in the final dose calculation, since the particles created may have different ranges, biological effects on the tissues and they can highlight the origin of the particles. After a nuclear reaction, the generated particles can have a very short range, inferior to 1 mm (e.g., recoil nuclei and α-particles). They can also have a medium range that is equal to the range of the primary protons (e.g., secondary protons), or they can have a

long range (e.g., secondary neutrons). (19) These secondary neutrons may deliver dose outside the target volume and it is important to take that into account. (20)

Taking the example of water, H_2O, this material has hydrogen in its composition and when an incident proton scatters off hydrogen, a secondary proton can be created with a relative angle of approximately 90º, with the same initial kinetic energy. (19)

At therapeutic energies, the possible secondary particles from non-elastic reactions are secondary protons, neutrons, γ rays, heavy fragments (such as alphas) and recoiling residual nuclei. Secondary protons comprise about 10% of the absorbed dose in a high-energy proton treatment beam; they have a small but non-negligible impact on the spatial dose distribution in a patient. (19,21) Deuterons and heavier ions are present in smaller proportions; collectively they comprise about 1% or less of the therapeutic absorbed dose. (22) Their energy and range are very small and they deposit their kinetic energy locally. (7)

A study of Lee et al., (23) aimed at simulating the fluence and dose distributions from a pencil beam in a water phantom. The authors used the Monte Carlo N-Particles Transport Code (MCNP) to model the transport and interaction of the particles in the material. The authors simulated a pencil beam with 160 MeV to irradiate a water phantom with dimensions of 40 cm × 40 cm × 50 cm.

To better understand the previous simulation and compare the results, we performed a repetition of this in MCNPX program. This simulation was repeated with the reported authors conditions and our results are shown in Figure 2. The simulation was performed with 3×10^6 particles and took 66 minutes to compute. Due to the high number of particles used, the maximum percentage of error in the values of deposited energy or fluence was about 0.012%.

In agreement to the conclusion of the authors, it is possible to observe that the protons contributed almost all the flux before reaching its range. The flux of the neutrons and photons are one order smaller, electrons are three orders smaller, and deuterons are four orders smaller than protons.

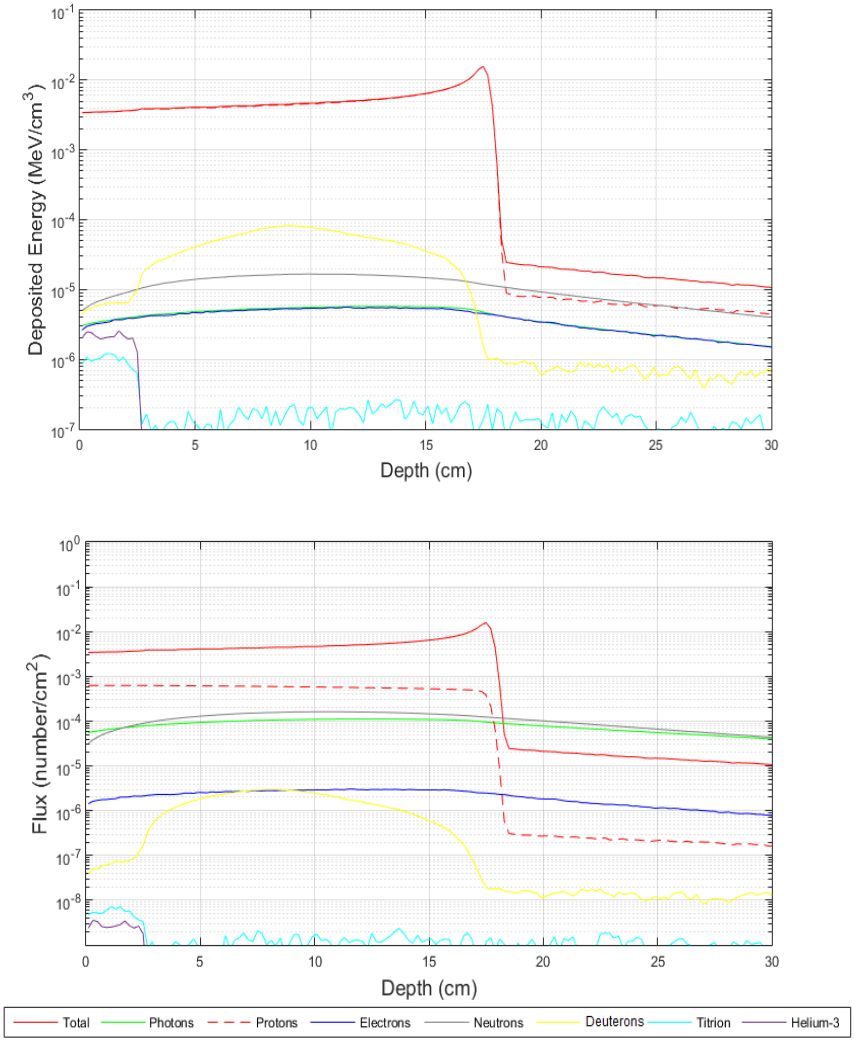

Figure 2 Energy deposition and flux curves of different particles generated by 160 MeV protons in a water phantom. The Y-axis is presented in a logarithmic scale.

It is also possible to observe that the neutron and photon contributed dose was 0.2% of the proton dose. In fact, taking the maximum deposited energy from protons and neutrons, we obtain the ratio:

$$\frac{maximum\ energy\ neutrons}{maximum\ energy\ protons} x100 = \frac{2x10^{-5}}{1x10^{-2}} x100 = 0.2\% \quad (2.5)$$

This contribution is small because of their low cross section with water, as explained by the authors.

It can also be observed that there is no relationship between the deposited energy and flux graphical representation. Before the Bragg peak, deuterons are the second highest contributors to the dose, after protons. After the Bragg peak, the neutrons and the secondary protons are the particles that contribute the most for the deposited energy in the water phantom. (23)

Because the proton beam energy used in this work in chapter 9 and 10 is 230 MeV, the simulation was repeated to observe if there are significative differences between the secondary particles created by these two energies. The results are shown in Figure 3 and it's possible to observe that there are no differences from the previous situation, in terms of the magnitudes of deposited energy and fluences for all types of particles. Similarly with the precedent one, the simulation was performed with 3×10^6 particles and took 96 minutes to compute. Due to the high number of particles used, the maximum relative error associated was 0.013%

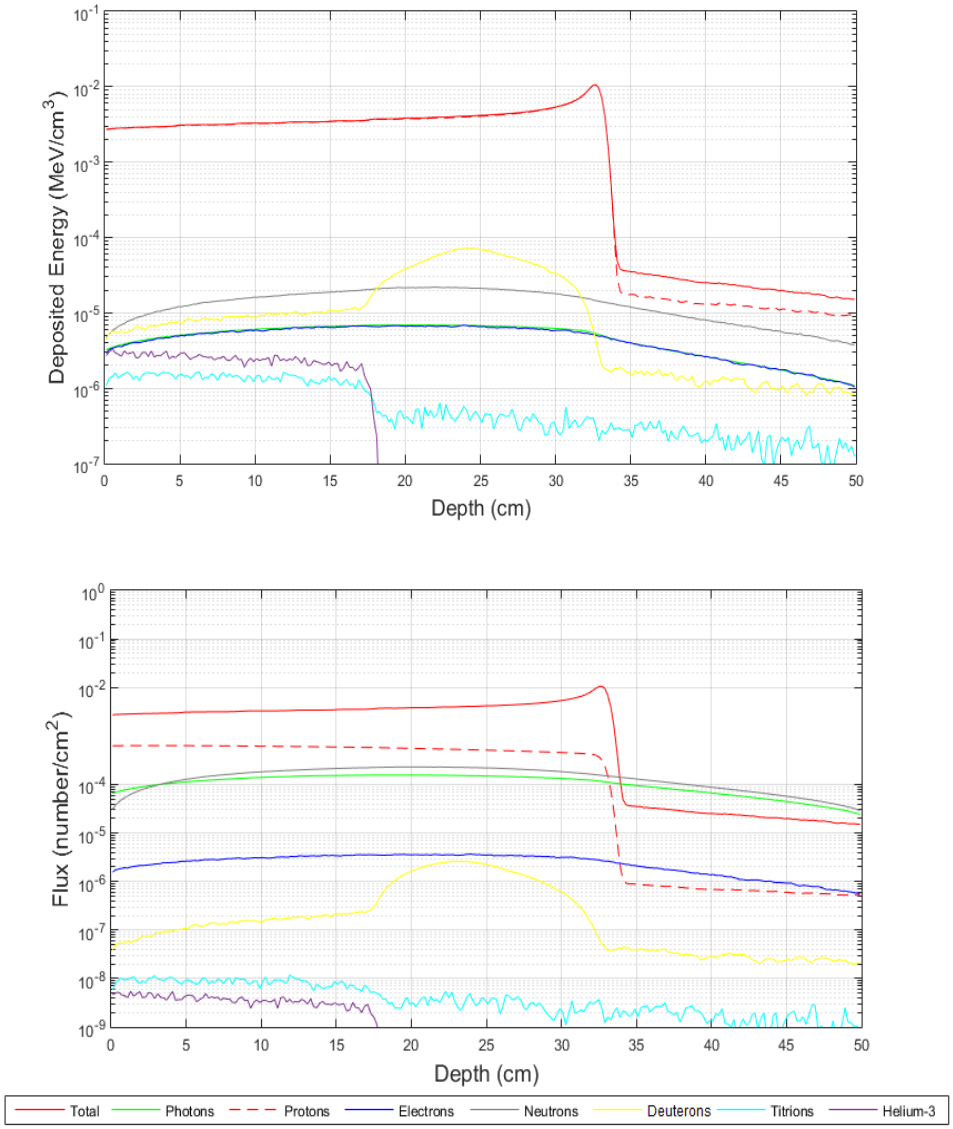

Figure 3 Energy deposition and flux curves of different particles generated by 230 MeV protons in a water phantom. The Y-axis is presented in a logarithmic scale.

A study of Paganetti (20) simulated the particle yield from different nuclear channels, as a function of proton penetration depth. The author performed this simulation with and without a 1.5 cm slice of bone material at the entrance of the water phantom. It is reported that, for a 160 MeV

beam, 19.6% of the primary protons undergo a nuclear interaction as they slowdown. The average number of secondary particles per primary proton nuclear interactions is 1.80 protons, 0.63 neutrons, 0.38 α-particles, 0.02 deuterons, 0.002 ^{3}He and 0.001 tritons. When comparing water and bone, it shows that the total amount of nuclear interactions is higher for bone. Nevertheless, this finding cannot be interpreted by the density difference, since the bone has more reaction channels and a higher probability for multi-particle evaporation and heavy particle evaporation, leading to a bigger yield of secondary particles. (20)

2.3. Range

The range (R) is the path length traversed by a charged particle before it is stopped. The R determinations can be done by using numerical or analytical approaches. The most common numerical approach is the continuous-slowing-down approximation (CSDA), which is obtained by integrating the reciprocal of the total stopping power with respect to energy. In this case, the range can be calculated as:

$$R = \int [S(E)]^{-1} dE \,, \tag{2.6}$$

where E represents the ion's initial kinetic energy. This method is a very close approximation to the average path length travelled by a charged particle as it slows down to rest, presenting a good estimative of range results in most clinical cases. However, it neglects lateral scattering because it relays on the assumption that the ions travel in a straight line; and also neglects the energy loss fluctuations in the matter along the beam path. (24)

There are uncertainties in proton's range that should be considered in the treatment planning process. These uncertainties depend on the precision and accuracy of the measurement system, the experimenter's skills, lack of knowledge on beams energy distribution and properties of all absorbing materials in the beam path. (7)

Range uncertainties can also occur from inaccurate conversions from computed tomography (CT) data to proton stopping power ratios, as well as setup uncertainties and variations in patient anatomical configuration during treatment delivery. At this point, positron emission tomography (PET) imaging is one of the few in-vivo range verification methods that can be performed on a patient during or immediately after the treatment. (25,26) This approach relies on the radioactivity generated in the patient after the treatment. The non-elastic nuclear interactions of the proton beam inside the human tissues creates isotopes of ^{15}O and ^{11}C, whose half live is 2 and 20 minutes, respectively. They emit a characteristic positron through β^{+} decay and the annihilation 511 keV gamma ray pair can be captured using a PET camera, allowing to verify and adjust the beam range. Despite giving important information, the time frame between

the treatment and the image acquisition needs to be very short to produce quality images and the method is also dependent of the location and volume of the tumor. (25,27)

There are some nomenclatures used to describe the range of protons within the Bragg peak curve. R_{80} is used to describe the range of protons where 80% of the energy is deposited after the Bragg peak. It is also very common to refer R_{90} that correspond to the range of protons where 90% of the energy is deposited, after the Bragg peak. R_{100} is the range at the maximum energy in the Bragg peak curve.

2.4. Quantities and units in ion therapy

2.4.1. Absorbed dose

The absorbed dose is a non-stochastic physical quantity for radiation therapy, protection, and radiobiology. It expresses the mean energy imparted by ionizing radiation to matter per unit mass, and it's defined as:

$$D = \frac{\bar{E}}{m}, \tag{2.7}$$

where $\bar{E}$ is the expected value of energy transmitted by ionizing radiation to a finite volume V. This value represents the sum of all energies that arrive at the volume of interest minus the energy that leaves the volume, in a specified time frame. m is the mass of the volume V under consideration. (28)

This physical quantity correlates the capacity of the radiation to produce effects. If the absorbed dose is zero, this means that the radiation doesn't produce effects.

The SI unit of dose is Gray (Gy), which corresponds to 1 joule per kilogram (J/Kg), meaning the absorption of 1 Joule per mass kilogram. This unit is used for all types of ionizing radiation and for any irradiation geometry.

2.4.1.1. Conversion from another units

In this work, the simulations results are expressed in MeV/cm^3/proton. The conversion to Gy, in water material, can be done as following:

$$1\ MeV = 1.6021\ x\ 10^{-13} J \tag{2.8}$$

$$1\ cm^3 H_2O = 1\ g\ H_2O = 0.001\ kg\ H_2O \tag{2.9}$$

$$1\ MeV/cm^3 = \frac{1.6021x10^{-13} J}{0.001\ kg} = 1.6021x10^{-10} Gy \tag{2.10}$$

In this case, the material used is water. If the material used is different from this, the calculations should be adjusted to account for the density of a different material.

2.4.2. Fluence

The particle fluence is a quantity that involves the number of particles (dN) incident on a sphere of cross-section area (dA).

$$\emptyset = \frac{dN}{dA} \tag{2.11}$$

The fluence is usually expressed in units of m^{-2} or cm^{-2}. This is a scalar quantity, which means that the direction of the incident radiation is not considered. (28,29)

2.4.3. Equivalent dose

The equivalent dose, H_T, is a radiation protection quantity used to quantify the biological effects of the radiation in the different tissues exposed to radiation. H_T in an organ or tissue T is given by:

$$H_T = \sum_R w_R D_{T,R} \, , \tag{2.12}$$

where $D_{T,R}$ is the mean absorbed dose from radiation of type R in the specific organ or tissue T, and w_R is the radiation weighting factor for each type of radiation R. The radiation R is given by the type and energy of radiation either incident on the body (external source) or emitted by radionuclides within the body (internal sources). (30)

Table 1 summarizes the values of w_R from different types of radiation. When there are several types of radiations involved, a sum of all the contributions is performed.

Table 1 Radiation weighting factors, w_R, for each irradiation particle type. (30)

Radiation type	Radiation weighting factor, w_R
Photons	1
Electrons and muons	1
Protons and charged pions	2
Alpha particles, fission fragments, heavy ions	20
Neutrons	A continuous curve as a function of neutron energy

The SI unit for H_T is joule per kilogram (J/kg) and is named sievert (Sv).

For neutrons, the biological effectiveness in the body depends on the neutron's energy. Due to this, the w_R is defined as a function of energy. The continuous function in neutron energy, E_n (in MeV), is defined for the calculation of w_R for neutrons, as follows:

$$w_R = \begin{cases} 2{,}5 + 18.2e^{-[\ln(E_n)^2/6]}, & E_n < 1\ MeV \\ 5.0 + 17.0e^{-[\ln(2E_n)^2/6]}, & 1MeV \leq E_n \leq 50\ MeV \\ 2.5 + 3.25e^{-[\ln(0.04E_n)^2/6]}, & E_n > 50\ MeV \end{cases} \quad (2.13)$$

2.4.4. Effective dose

The effective dose, E, is the tissue weighted sum of equivalent doses in all specified tissues of the body. This is a radiation protection quantity and is given by the expression:

$$E = \sum_T w_T \sum_R w_R D_{T,R} = \sum_T w_T H_T\ , \quad (2.14)$$

where w_T is the tissue weighting factor for a tissue T and $\sum w_T = 1$. This sum accounts for all organs and tissues considered to be sensitive to the induction of stochastic effects. $D_{T,R}$ is the mean absorbed dose in an organ or tissue T from radiation of type R. (30)

This quantity is based on the mean absorbed doses in organs or tissues of the human body and the w_T are mean values representing an average over many individuals of both sexes and ranging ages. Furthermore, it is calculated for a Reference Person, from whom the equivalent doses in organs and tissues are calculated by averaging the doses for Reference Male and Reference Female. It provides a value that consider the specific exposure conditions of an individual but not of its individual properties.

The process of determining the effective dose starts with the determination of absorbed and equivalent dose for the Reference Female and Reference Male, separately. The sex-specific doses are then averaged, resulting in equivalent doses for Reference Person. This dose is then weighted by the w_T and summed over all organs, shown in Table 2. It is possible also to adapt the procedure to pediatric reference individuals.

Table 2 Tissue weighting factors, w_T. (30)

Tissue	w_T	$\sum w_T$
Red bone marrow, colon, lung, stomach, breast, remainder tissues	0.12	0.72
Gonads	0.08	0.08
Bladder, oesophagus, liver, thyroid	0.04	0.16
Endosteum (bone surface), brain, salivary glands, skin	0.01	0.04
Total		1.00

The remainder tissues mentioned in Table 2 are adrenals, extra thoracic region, gall bladder, hearth, kidneys, lymphatic nodes, muscle, oral mucosa, pancreas, prostate, small intestine, spleen, thymus, and uterus/cervix.

The ponderation factors are dimensionless, and as such the units for effective dose are also sievert (Sv). (30)

The quantities of equivalent dose and effective dose are not measurable. They are determined by radiation monitoring using operational quantities (e.g., ambient dose equivalent) or by applying conversion coefficients that relate radiation field quantities to organ equivalent or effective dose.

2.4.5. Ambient dose equivalent

The ambient dose equivalent (H*(d)) is the radiation operational quantity used to calculate effective dose, in area monitoring. This is the dose equivalent, at a point in a radiation field, that would be produced by the corresponding expanded and aligned field in the ICRU sphere at depth, d, the radius opposing the direction of the aligned field.(19,30)

The ICRU sphere has a diameter of 30 cm, and the composition is 76.2% of Oxygen, 10.1% of Hydrogen, 11.1% of Carbon and 2.6% of Nitrogen.

For strongly penetrating radiation, it is recommended that d is 10 mm and for weakly penetration radiation the value recommended is 0.07 mm.

The unit used is also Sievert (Sv).

3. Radiation therapy

Radiation therapy (RT) is based on the fact that radiation can interact with a biological tissue, causing direct or indirect damage to the genetic material (deoxyribonucleic acid, DNA). The damages on the cell DNA undergo restoration mechanisms but the accumulation and/or severity of those can lead to mutations or cellular death. In theory, the increase on the radiation dose leads to an increase on the damages of the DNA and, therefore, augmentation of cell death probability. In reality, it is necessary to take into account that RT affects both tumoral and healthy tissues and, since the mechanisms to restore healthy cells are more efficient than those of tumoral cells, an equilibrium must be achieved to obtain the best clinical outcome possible. (3) These differential mechanisms of cell restoration are what lays behind the treatment fractionation, practiced nowadays.

RT can be performed by using internal sources placed inside the patient (brachytherapy) or by external radiation administration (external RT). The most used technique for external RT is the administration of photons or electrons by a linear accelerator (LINAC). The LINAC has a mechanical structure, a gantry, that allows a volumetric administration of megavoltage photons in the patient, conformed to the region of interest. The type of radiation used has an important role in the dose conformality, since their physical interactions with matter are different.

Electrons and heavy ions (protons and carbon ions) are charged particles that undergo frequent interactions in the material and have a finite range. Electrons have a significant scattering that produces very diffuse dose distributions. The protons mostly undergo small angle scattering events and deposit the maximum energy per path length close to the end of their range.(2)

The photons are uncharged particles and don't lose their energy continuously. They deposit the dose mainly via secondary electrons that are produced in ionization effects inside the tissues. The dose distributions of these particles, as a function of depth, show a maximum dose close to the entrance after a short build-up and then an exponentially decreasing energy deposition with increasing depth in tissues. (2,29) This is one of the biggest disadvantages when compared to proton therapy because the finite range of protons allows us to spare more healthy tissues before and after the Bragg peak region, since the dose plateau preceding the peak is also low when compared to the dose given by other particles. (29)

Figure 4 shows a comparison between depth-dose curves of various particles used in RT (electrons, photons, protons, and carbon ions) as function of depth in water.

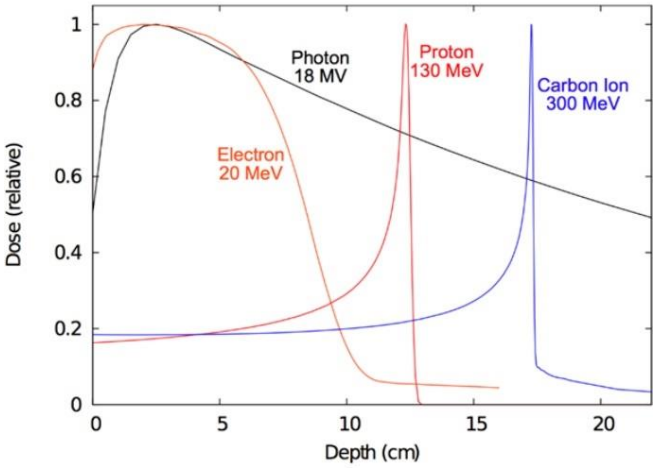

Figure 4 Comparison of the depth-dose profiles for electrons, photons, protons, and carbon beams. (41)

In the actual clinical practice, most of the treatments use beams of photons or electrons due to advanced developments in therapy technology. Besides that, the paradigm is changing and evolving to more usage of heavy charged particles in clinical practice, due to the investments in technical progress and decrease of equipment costs.

There are several publications that show dosimetrical comparisons between treatment plans with different particles and techniques. The results are transversal in the literature and highlight notorious differences in terms of dose fall-off and exit doses. Figure 5 shows a dosimetrical plan of craniopharyngioma obtained with photons (on the left), and with protons (on the right). Those results were obtained with images from the same patient but planned with different techniques. The color lines presented are isodose lines, that connect the points with the same deposited dose inside the patient. It is possible to observe that the images on the left, planned with photon beams, have bigger exit doses than the images on the right, planned with proton beams.

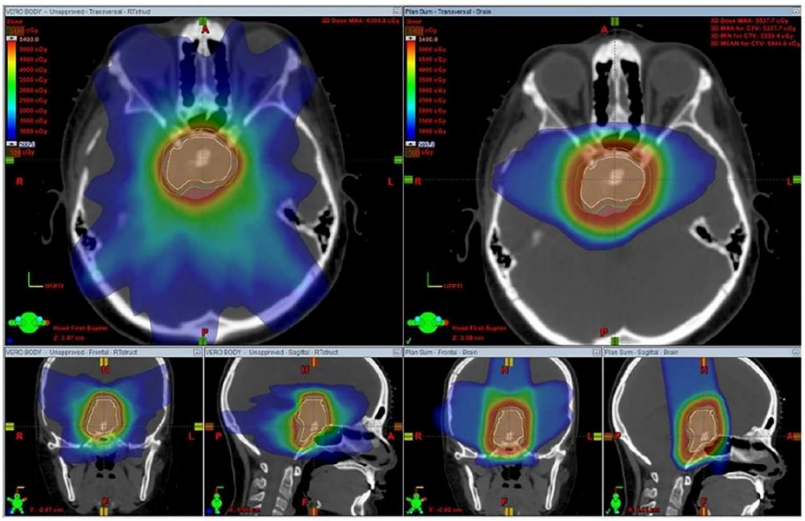

Figure 5 Dosimetrical comparison of craniopharyngioma plans obtained with photons (on the left) and with protons (on the right). (42)

Proton therapy shows advantages over conventional RT with photons and electrons, such as an improvement on normal tissue sparing distal to the tumor, differential modulation of the immune system, increased LET and RBE in the tumor and lower integral dose in normal tissue compared to modern photon therapy. (43)

The tumor control probability (TCP) is the probability that a given dose at the tumor volume will kill the tumor cells. The normal tissue complication probability (NTCP) is the probability that a given dose will lead to complications due to the toxicity of radiations. As illustrated in Figure 6, the probabilities mentioned are typically characterized by a sigmoid function. One of the indications to RT is that the TCP curve appears on the left side of the NTCP curve. In terms of effectiveness of the treatment, this is bigger when the separation of these two curves increases. In clinical practice, this is not a real scenario and due to the proximity of the curves, it's necessary to reduce the errors associated with RT administration.

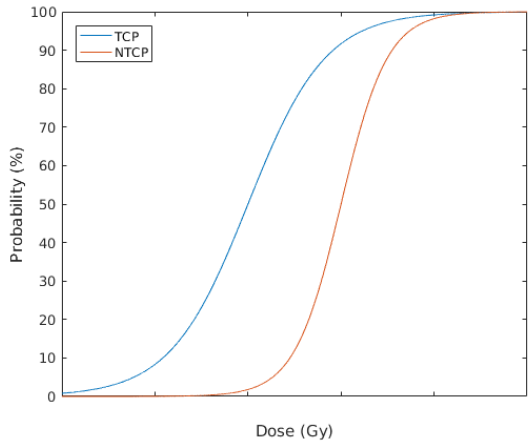

Figure 6 Tumor control probability, TCP, (represented at blue) and normal tissue complication probability, NTCP, (represented in red). (11)

The linear energy transfer (LET) describes the energy transferred from the beam to the irradiated material, per unit of particle path length (in units of keV/μm, for example). (19,21) In the case of protons, the LET has a slight increase along the particle penetration and experiences a big augmentation downstream the area of the Bragg peak, which is normally located inside the target. (7,44) The rate of absorption of energy from an energy-modulated proton beam, producing a SOBP, varies only to a modest degree with depth from the entrance to near the beginning of the SOBP. There, the absorption of energy becomes increasingly rapid.

The biological effect of a physical dose (e.g. absorbed dose) depends on the type of radiation, its LET, the target tissue type, the fraction of an organ exposed and the fractionation scheme. (19)

The relative biological effectiveness (RBE) is the ratio of biological effects to that the same physical dose of a standard radiation, usually from ^{60}Co. The RBE is defined as:

$$RBE = \frac{D_x}{D}, \tag{4.1}$$

where D is the value of a certain radiation dose that leads to a specific biological effect and D_x is the standard radiation dose necessary to produce the same effect. (19)

There have been numerous *in vivo* and *in vitro* experiments to attempt to determine the proton RBE and the accepted mean value is 1.1. This means that a lower dose of protons is necessary to reach the same biological effect as photons because they have approximately 10% higher biological effectiveness. (4) Despite the controversy when using this standard value, there are no studies that show adverse responses to this use. Multiple studies and efforts are being made to improve the understanding of RBE and develop new models to predict the RBE as a function of tissue type, dose and LET. (4) At this point, it's known that RBE increase with LET and low energy protons can have high RBE values.(19)

In the practice, the physical dose (in Gy) is multiplied by 1.1 to obtain the RBE-weighted absorbed dose, D_{RBE}.

When a certain dose is prescribed to a patient, it's assumed that this dose reflects a specific NTCP on an organ level. The clinically prescribed dose refers to an energy deposited in a volume the size of a CT voxel, while biological effects are determined by energy depositions on a cellular level. The dose-response relationships are patient and tissue specific, and, at this point, there are very few literature results that allow to establish individual prescriptions. Consequently, RT is prescribed based on physics and physical quantities (as absorbed dose), and this should have a primary role in dosimetry and clinical protocol.(2)

When the goal is to make comparisons about the effects of photons versus protons or to predict therapeutic outcomes based on the experience with other particles, the RBE-weighted dose can be used. However, those quantities serve different purposes and should be used in different steps of the treatment planification. To avoid confusions, it's important that the quantities involved to be clearly specified. (21)

3.1. FLASH therapy

As discussed before, the toxicity induced in the healthy tissues adjacent to the target volume limits the amount of dose that can be administrated. With the growing number of long-term cancer survivors, radiation administration techniques need to be continually updated to increase or maintain the anti-tumoral effect and diminish the toxicities in the healthy tissues.

In the last years, there have been several studies that suggest that irradiation at ultra-high dose rates (FLASH) may decrease toxicities in the normal tissues, compared to conventional irradiation techniques, maintaining the same level of anti-tumoral response. This technique diminishes the overall time for the dose delivery and it's been tested in pre-clinical experiments on animals as being capable of increasing normal tissue tolerance for some tissues, making it potentially possible to escalate the curative doses to target volumes. (45) However, the sparing effect of FLASH has no known solid biological and physical explanation and more investigation in the field is needed to detail all the mechanisms involved. (46,47)

Favandon et al., (13) performed thoracic irradiations in mice with a single faction of 17 Gy at conventional dose rates (0.3 Gy/s) that induced moderate and severe pulmonary fibrosis after 36 weeks. The authors also performed a single irradiation, with the same dose, but with ultra-high dose rates (40-60 Gy/s) and observed that the pulmonary fibroses were reduced comparative to the previous situation. The same levels of pulmonary fibroses reported in the conventional irradiation were observed when 30 Gy were administrated with FLASH, and the anti-tumor efficiency was not different between the two techniques. In a study of Montay-Gruel et al., (12) the

authors performed a single irradiation of 10 Gy in mouses' brains, with the two RT modalities. The main observation was a relative protection of normal tissues with FLASH irradiation with dose rates ≥ 100 Gy/s, compared to conventional RT. Here, the total dose was administrated in one single fraction and the FLASH-RT effect was found to be reproducible with 1-10 pulses of 1.8-2 μs and overall time less than 200 ms and a dose-rate within the pulse above $1.8x10^5$ Gy/s. These two studies illustrate some results in the literature and were performed with electrons, as most of the available evidence, due to the facility to create electron beams with high dose rates. (12,14,48)

It is more difficult to produce high rate doses with proton beams due to heat limitations but there are some advances and reported results. (43)

In a study of Diffenderfer et al., (49) the authors irradiated mouse intestinal tissue and flank tumor of pancreas cells. The irradiation was performed with double scattering technique, using FLASH (dose rates of 78 ± 9 Gy/s) and standard dose rate proton RT (0.9 ± 0.08 Gy/s). The results show that FLASH PTR produce less intestinal fibrosis compared to conventional PTR but there weren't observed differences regarding the tumor response between the two modalities. In this study some limitations of FLASH proton therapy were highlighted, namely regarding the use of cyclotron-based double-scatterer proton systems due to the limitations in maximum field size that can be achieved at high dose rate. Pencil beam scanning (PBS) is proposed as a solution because the spot scanning can be of the order of 2 to 5 ms for a 5-mm spot-to-spot distance, which can be consistent with FLASH conditions. In the meantime, the effects of PBS are being studied in animals. Another challenge with PBS is that the time required to move the beam between spots could have implications on the FLASH effect (16). Another question raised is if the high LET in the Bragg peak would enhance the FLASH effect. However, as the high LET is quite narrow in the depth direction, it is expected to have a significative larger effect on smaller targets than larger targets.

The FLASH technique combines complex and several inter-dependent physical parameters, such as the dose, pulses (number and width), irradiation time (<200 ms), mean dose rate and dose rate within the pulse. While in conventional RT the mean dose rates are ≥0.01Gy/s, in FLASH-RT the mean dose-rates are ≥40Gy/s.

One of the main differences between FLASH-RT and conventional RT is the irradiation time. These very short irradiation times suggested that an early oxygen modulation of the radiochemical events that depend upon oxygen concentration in the irradiated volume. Flash-RT could cause a rapid consumption of local oxygen and elicit a transient radiation-induced hypoxia. This oxygen dependency was confirmed by some studies that show that hyper-oxygenation can abolish the FLASH effect. (48)

3.2. Volume specifications

In RT, the treatment is prescribed to a target volume (TV) within the patient, usually the tumor location. There are different volumes with different definitions and requirements for the treatment prescription, shown in Figure 7. (19)

The gross tumor volume (GTV) and the clinical target volume (CTV) are oncological volumes. The GTV consists in the clinical disease and its location is determined by clinical examination and imaging exam registration (for example MRI, CT, and endoscopy). The CTV is the volume resulting from adding a margin to the previous one, to include sub-clinical disease extension. It is also frequent to contour an internal target volume (ITV) that encounter the various positions of the CTV along a specific timeline. Usually, this structure is obtained with a 4D-CT, where the interest volume is followed in the cycle of respiration, for example, to make sure the CTV is covered all along its motion.

The planning target volume (PTV) is a geometrical structure, designed to take into account several errors and variances. These include the GTV and CTV structures plus a margin to encounter for set-up and organ motion margin. When the ITV structure is used, this margin is added to the ITV, instead of the CTV. There are some proton-specific issues regarding the PTV specification, due to range uncertainties. In the case of PTR, it is recommended that the PTV be designed relative to the CTV based on lateral uncertainties. It is also required to perform an adjustment within the beam-design algorithm to account for differences in margins due to uncertainties along the beam direction (i.e., range uncertainties) and set-up and motion margins. (21)

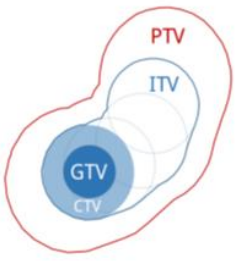

Figure 7 Illustration of the target volumes. (11)

In the case of FLASH-RT, we will have an hypofractionated treatment scheme, meaning that less treatment fractions with bigger dose per fraction will be applied. In these schemes, the weight of systematic errors increases comparatively to random error, because we have less treatment fractions. This can raise the discussion of adding more margin to the PTV, since the weight of systematic errors will be bigger. Likewise, we can also raise the discussion about the ITV definition, since the treatment is delivered in less than 1 second, for FLASH-RT. Besides, the

intra-fraction motion can lose some focus in FLASH-RT. The tumor location is of extreme importance because it is crucial that the full dose could be delivered at the right time, when the tumor is in the beam path, and therefore an eventual motion of the tumor is less important since the irradiation time is very small.

The organs at risk (OAR) are also contoured and represent normal tissues and organs where the radiation can produce adverse events. The panning organs at risk (PRV) is also a geometrical concept, which is obtained by adding a margin to the OAR, to account for organ motion and set-up errors.

The contouring process is of extreme importance since it allows to account for the radiation dose received by the TV and the OAR.

3.3. Treatment planning and quality control

The treatment plan phase consists in estimating a 3D dose distribution inside the patient, through a dose calculation algorithm. The Hounsfield units from the CT image are converted to stopping powers and the calculation is made taking that into account.

The treatment plan comprises the machine parameters on how the treatment must be delivered (e.g., gantry angles, number of fields and couch angles). The treatment planning system (TPS) is the software that generates the plan and allows to make changes in the parameters to optimize the dose distributions.

Usually, the therapeutic dose is prescribed to the PTV. This structure is also used to report doses and one of the usual constraints is that 95% of the prescribed dose should cover this structure.

After a treatment plan is computed, the constraints for target volumes and OAR are accessed in the dose-volume histogram (DVH) that shows the dose received by each contoured volume. The constraints are published and can vary with the technique or medical request. The discussion of these constraints is out of the scope of this work, for more information, please refer to QUANTEC Guidelines. The treatment optimization is a dynamic process and takes part to fulfil the treatment objective of homogeneously cover the target volumes with the prescribed dose and deliver the minimum dose possible at the OAR.

Another condition that must be met is the ability of the machine to deliver the dosimetrical plan. This consists in delivering the dosimetrical plan in a water or plastic phantom. The dose is measured at a certain depth using diodes and those measurements are compared to the TPS, in the same conditions (phantom geometries and measurement depth). (11)

4. Proton beam production

A PTR center is composed by an accelerator with an energy-selection system to produce protons of the desired energy, a beam transport system to conduct the beam to the treatment delivery system and a treatment-delivery system. Figure 8 shows the layout representation of the PTR facility in the Massachusetts General Hospital, where it is possible to observe the components that compose the center and that a single accelerator can deliver the beam to multiple rooms.

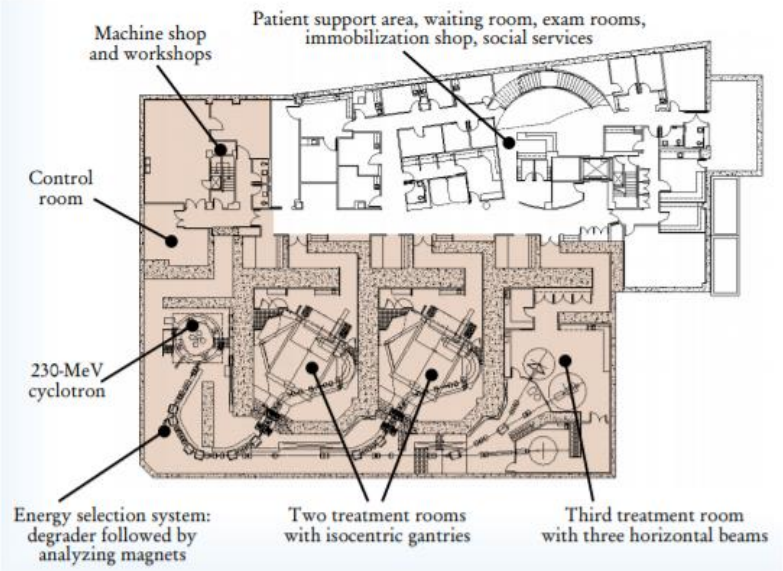

Figure 8 Proton-therapy facility layout at Massachusetts General Hospital. Adapted from (3).

The therapeutic PTR beams have energies typically from 70 to 250 MeV and are created by the ionization of hydrogen atoms to extract protons. To achieve these energies, the kinetic energy of the protons is increased using a particle accelerator. It can be a cyclotron, a synchrotron, or a linear accelerator. Despite being very used in the therapy with photons and electrons, the use of linear accelerators in PTR facilities is much less common since they limit the maximum energy available for the treatment.

Cyclotrons are more compact, have higher beam intensity and are the most used in PRT facilities. Protons are accelerated to the maximum of the energy of the cyclotron (e.g. 230 MeV), and when a lower energy is required, they are slowed down by electromechanical insertion of energy degraders in the path, in the energy selection system. (4,19) The mechanism of a cyclotron is described in Figure 9. The particles are accelerated by an electric field between two D-shaped hollow electrodes (called “dees”), in a vacuum tank. A fixed magnetic field is applied to bend the

path of the protons and, as their energy increases, their radius also increases until it reaches a maximum and the protons are extracted at their maximum energy.(19,21)

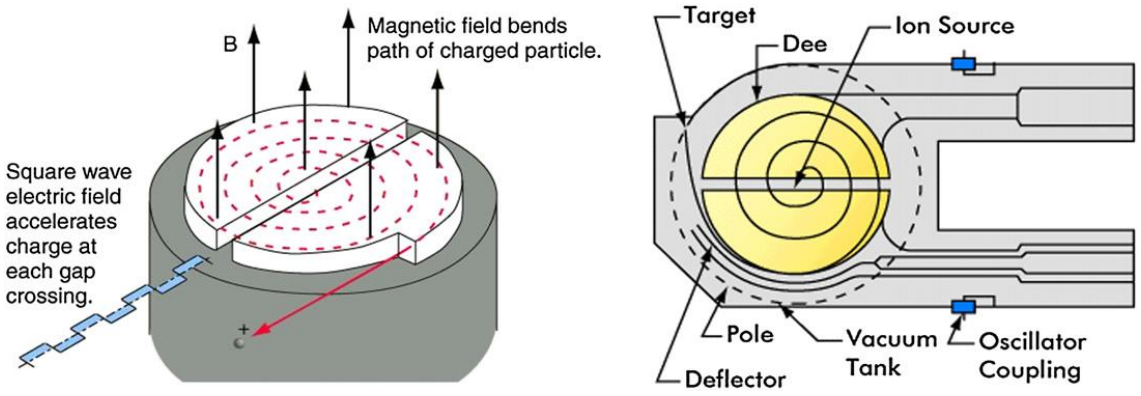

Figure 9 *Acceleration of protons in a cyclotron. Adapted from* (4)

In the case of synchrotrons, the beam is delivered at specific energies, requested for the treatment. The low energy particles are injected into the accelerator ring and a radiofrequency electric field increases their velocity while they are being confined to a circular orbit by the magnetic field. The synchrotrons deliver the proton beam in pulses, usually with a few seconds duration and a few seconds dead-time between the pulses. This characteristic may be an issue to techniques of energy repainting, beam gating and to FLASH administration. (3,21)

After the energy selection system, the proton beam is transported to the treatment rooms. The beam transport system is composed of several magnets to keep the beam focused inside the beamline and, when it arrives in the treatment room, it is directed to the patient through a fixed beamline (usually used to ocular irradiation) or a rotational gantry. At the exit of the beamline, the final beam preparation is performed in the nozzle, following the treatment plan specifications.

The treatment-delivery system is composed by several subsystems. Some of them are shown in Figure 10 and are the beam nozzle (A), volume-tracking and beam-gating device (B), gantry (C), patient positioning and immobilization system (D) and a robotic couch (E). The final component of proton-therapy facility is a shielded area to separate the accelerator and beam-transport system from the treatment rooms. (21) Also present in the treatment room is an imaging system to acquire internal images of the patient, prior to the irradiation. This can be a CT- on rails or a cone-beam CT system, represented as F in Figure 10.

Figure 10 Components of the treatment-delivery system. (A) beam nozzle, (D) volume-tracking and beam-gating device, (C) gantry, (D) patient positioning and immobilization system, (E) robotic couch, (F) cone-beam CT system. Adapted from (50).

The accelerated proton beam that comes out of the nozzle is very thin and can't be directly applied to treating 3D tumor volumes. The beam must be expanded longitudinally and laterally and modulated to conform the target shape, forming a SOBP. The two approaches are explained in chapter 5.

5. Proton beam delivery techniques

The characteristics of a proton beam are determined by the intrinsic physical properties of the protons, the beam generator accelerators, and the devices used to control it.(21) The beam has a Gaussian shape and width of the order of millimeters when it is extracted and a narrow energy spectrum that results in a narrow spread of ranges in a target. Therefore, that beam must be spread out in three dimensions to match the target volume because the dimensions of a clinical target are typically different from the dimensions of an unmodified particle beam. There are two major techniques to do so: passive scattering and active scanning.(19)

5.1. Passive scattering

In this technique different devices composed of different materials are used, usually with high atomic number, to obtain a 3D uniform dose distribution to the TV. The devices are coupled to the gantry nozzle and perform beam scattering and modulation of the primary beam, through all the irradiation fields used on a treatment. (21)

The range modulation is achieved by insertion of one absorber material, with different thickness, in the beam path. This modulation in depth can be achieved spatially by using an absorber plate with ridge-shaped elevations. These range modulators are commonly called ridge filters and are shown in Figure 11. (21)

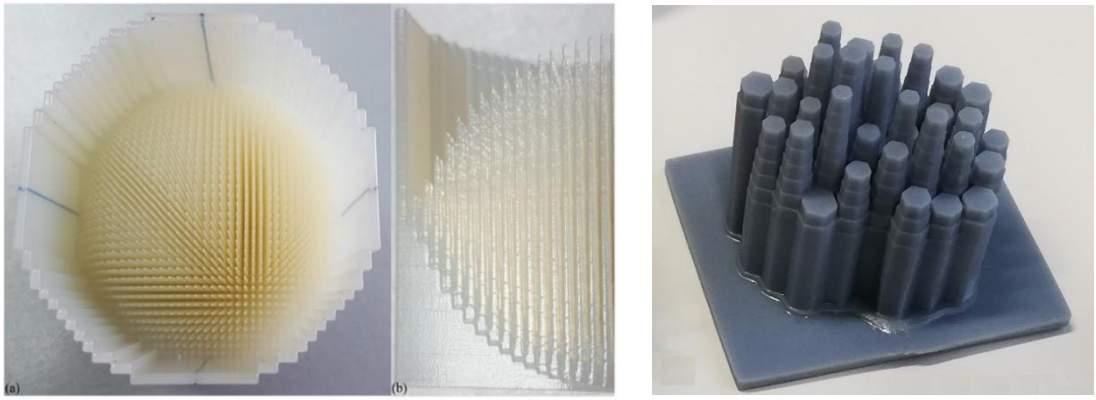

Figure 11 Ridge filter image on the left (15). Figure on the right is prototype from IBA

Range modulation can also be achieved during a given time interval, by using a rotating absorber propeller with different blade thicknesses, known as range modulator wheel (RMW), shown in Figure 12. (21) This device has different thicknesses of material that, combined with the device rotation, modulate the range of the beam. To create a SOBP that covers the TV, the beams

are weighted at each step, as shown in chapter 7.1.1. There are authors that report using two different materials to create each blade. The most common combination is Lexan and Lead.

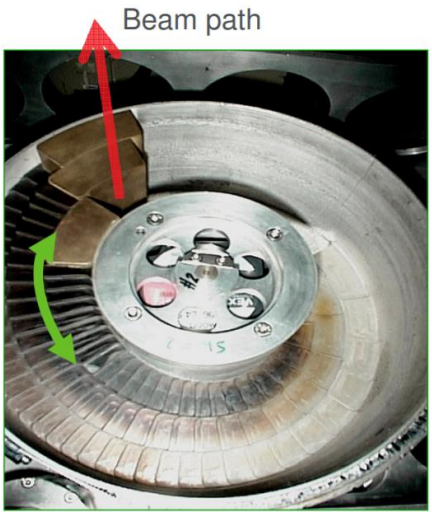

Figure 12 Photography of an RMW. The wheel turns in the sense of the green arrow and the beam crosses the device in the direction of the red arrow. Adapted from (51)

It is also necessary to insert a scattering material in the beam path to enlarge the lateral dimensions and cover the TV. This can be done with a single scatterer or a double scatterer system, the second one being the most used. This technique combines two scatterers and uses combinations of materials with high and low atomic number, bearing in mind that the first ones have a higher scattering power. (2,52)

Collimators (blocks or apertures) are also used to conform the dose distribution laterally to the shape of the interest volumes, usually made of brass with sufficient thickness (around 2 to 8 cm) to absorb the protons with higher energies. (4)

The last device used is a compensator designed to shape the dose distribution to the distal surface of the PTV. Due to this, there is a region of normal tissue in the proximal region that will receive an unnecessary dose.(21)

The field-shaping device and compensator should be as close to the patient's skin as possible to minimize scattering, which degrades the lateral penumbra. Due to the proton interactions in the collimator and compensator, neutron radiation is generated close to the patient. (21) A schematic view of the beam modifying devices is shown in Figure 13.

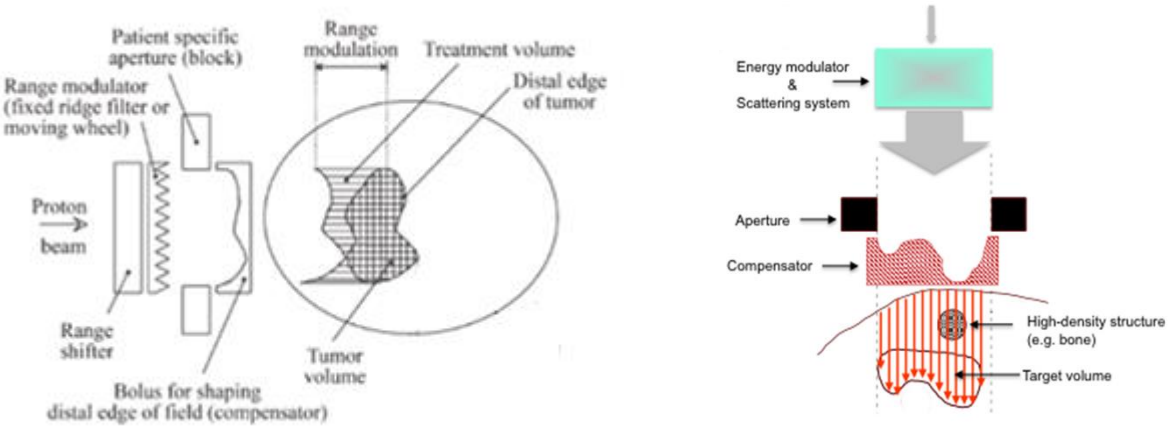

Figure 13 *Schematic diagram of patient-specific beam-modifying devices. Adapted from* (2,21)

This technique has advantages such as safety and simplicity. However, this technique involves the usage of a specific range shifter modulator for each energy and SOBP, which can have influence on the dose uniformity. Along with this, most of the beam modifying devices are patient- and/or field-specific which increases the cost, verification, fabrication, and manipulation time. Moreover, these materials can became activated with repeated irradiation and must be stored properly before being recycled. (11,21) Another disadvantage is that this technique tends to be sensitive to variations in beam position relative to the scatterer and produce a larger penumbra. (21)

5.2. Active scanning

This technique consists in scanning a small beam with Gaussian-shape, until all the 3D structure of the TV has been irradiated. This scanning is possible because the protons are charged particles and their path can be deflected when submitted to a magnetic field. The scanning magnets, mounted inside the nozzle, deflect the narrow proton beam and guide it to reach the full lateral extent of the target volume. (19)

Each scanned beam will administer the dose at iso-layers inside the TV, at a specific energy. After that, the energy of the beam is changed, and it will be scanned through another layer of the TV, as shown in Figure 14. It is important to note that iso-layers are not necessarily iso-depths, since there are tissue heterogeneities inside the patient. (2) This process is repeated until the full 3D dose administration is completed. This irradiation is done within a matrix of spots inside the TV, determined by the TPS, and the weight of each pencil beam to be defined as well as its fluence or number of protons delivered.

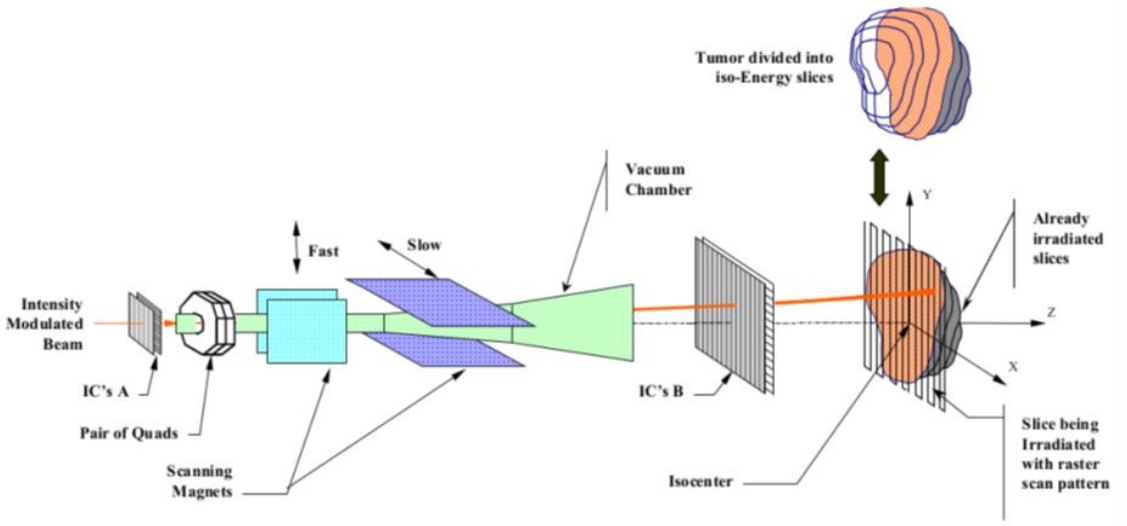

Figure 14 Representation of a proton therapy beamline with pencil beam scanning delivery. (11)

The most used technique is Proton Beam Scanning (PBS), where the pencil beam transported to the beam nozzle is directly sent into the patient without interacting with any scattering or energy-modulation devices. (19) The absence of scattering materials allows that a sharper Bragg peak be employed when compared to passive scattering techniques.

The time required to change energies is an important factor since it determines the duration of the treatment and the dose homogeneity, due to potential patient motions. (2) The absence of collimators and range compensators highly reduces neutron production and manual operations. However, the delivery itself is generally slower due to the time required to switch the proton energy between each layer (typically ranging from 0.5 to 2 seconds). (53)

This technique provides a better flexibility, enabling the delivery of complex heterogeneous dose distributions, also called intensity modulated proton therapy (IMPT).

6. Monte Carlo simulations

Monte Carlo (MC) simulation is a stochastic method with inherent randomness, meaning that the same set of parameter values and initial conditions will lead to a combination of different outputs. Inversely, in deterministic models, the output is fully determined by the parameter values and the initial conditions.

A MC simulation is a numerical method to solve equations or to calculate integrals based on random number sampling, that can be applied to simulate physical interactions and is accepted as the most precise way to compute dose distributions in materials of complex density such as the human body. (17)

In this analysis a model is created, as similar as possible to the physical reality, within which interactions take place based on known probabilities of occurrence, with a random sampling of probability density functions (PDFs). The program tracks the particles, one at a time, from their origin and follows their interactions through the geometry, randomly sampling from one or more probability distributions at each step, to choose how the particle might interact, its change of direction, loss of energy and potentially creates secondary particles. (19,54)

The MC algorithms use a computer program known as random number generator (RNG). This creates a large number of random numbers to solve complex problems. Because they are created by a computer, the numbers cannot be called absolutely random due to their predictable nature. Nevertheless, there are some criteria for this pseudo-randomness, such as they shall be uncorrelated and appear independent.

The probabilities of occurrence are related to the cross sections of the materials used. The behavior of the real particles within the physical system is predicted from the accumulated data on many simulated particles. This technique is well suited to solve complex 3D and time dependent problems because no averaging approximations are required in space, energy, or time. (54)

It is not feasible to simulate all the physical interactions for charged particles due to the computational time. Because of the big number of small angle scattering events of each Coulomb interaction, there was the need to develop class II condensed history algorithms that condenses or sums the energy losses and directional changes. The MC methods use a combination of continuous processes based on condensed history and discrete processes based on an explicit model of each interaction. In PTR, discrete processes are typically nuclear interactions, secondary particle production (including δ-electrons), and large angle Coulomb scattering. (19)

Because MC computations follow the simulated particle until it escapes the geometry of interest or until it loses a big fraction of its original energy, the computation times are commonly

very long and many particles need to be simulated to achieve an acceptable accuracy. (17) This minimum energy until where the particle should be followed (cut-off energy, E_{cut}) can be established by the user. The uncertainty of MC results depends on the number of histories, N, with the error in the simulated quantity being proportional to $1/\sqrt{N}$. (19,54)

The results of MC simulations are typically histograms, also denominated as tallies. These files are completed with information through the simulation time.

6.1. MCNPX

The Monte Carlo N-particles Extended (MCNPX) code was developed by Los Alamos National Laboratories, and it is designed to analyze the transport of particles by MC methods, over a vast range of energies. The code can simulate neutrons, gamma rays and secondary particles such as secondary gamma rays, secondary electrons, and secondary neutrons.(55)

The MCNPX code is used in areas such as radiation protection and shielding, dosimetry, medical physics, fission and fusion reactor design.

This program is used in multiple studies and the results of proton absorbed doses calculated with it have been validated by measurements in different studies. (56,57)

The software used in this study is MCNPX version 2.7.0.

6.1.1. Input file

To start a simulation, it is necessary to create an input (INP) text file with the relevant information for the program function. Those are the geometry specification, the description of the materials in the problem and cross-sections used, the location and characteristics of the particle source, the type of answers or tallies desired and the variance reduction techniques to improve the efficiency. The MCNP input file has 3 main sections: cell card, surface card and data card, separated by a blank line delimiter at the end of each, as shown in Figure 15.

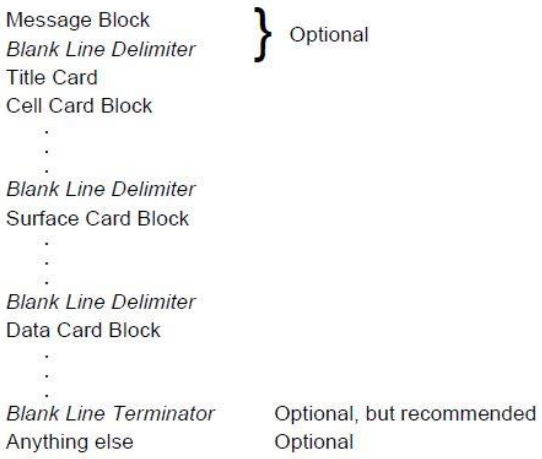

Figure 15 *Input file text form in MCNPX.*

Cell card

In the cell card, the first entry should specify the number attributed to each cell in the problem, followed by the material number (arbitrarily assigned by the user and specified in the data card), cell material density and the complete specification of the geometry of the cell. Figure 16 shows the cell card of one example problem to illustrate the explanation. This is constituted by a rectangle of water (defined as cell 1) surrounded by air (defined as cell 2). It is necessary to define a geometry that contains the problem, in this case, the cell 3. As a requisite, it is also necessary to surround all the geometry by a void space, defined as cell 4.

The character "c" is a comment card and can be inserted anywhere in the INP file. The "$" character terminates the data entry and anything that follows this symbol is interpreted as a comment.

The cell material density, d, can be interpreted as atomic density in units of 10^{24} atoms/cm^3 (e.g., atoms/b-cm) if $d > 0$, or can be interpreted as the mass density in units of g/cm^3 if $d < 0$.

The cell 1 is constituted by the material 1, with a density of 0.997 g/cm^3, and is defined as a region in space with negative sense with respect to surface 5. The negative sense means that it refers to the area inside the surface specification. The cell 3 is constituted by material 2, with a density of 0.00125 g/cm^3, and it defines a region in space with negative sense with respect to surface 7, excluding the volume of surface 5 and 6. The cell 4 is a void, with no density associated, and is defined as a region in space with positive sense with respect to surface 7. The positive sense indicates that it refers to the area outside the surface specification.

The importance of the cells can be defined to one or various particles used in the problem. The importance is used to terminate the particle's history if the importance is zero, to move the particles to cells with more importance within the geometries and to weight the cut-off. In the

example shown, the importance of protons in cell 1,2 and 3 was the same, meaning that all the geometries had the same importance for the final output. The cell 4 is a void and the importance of protons in the cell was set to zero.

```
c Example problem
c ============= CELL CARD ============================================================
1     1 -0.997     -5               imp:h=1   $ water
2     2 -0.001225  -6               imp:h=1   $ air
3     2 -0.001225  -7 #5 #6         imp:h=1   $ space to run the problem
4     0            +7               imp:h=0   $ void specification
```

Figure 16 *Example of a cell card specification.*

Surface card

The surface card must contain the surfaces used to describe the cells. The first entry should be the surface number, followed by an alphabetic mnemonic entry that indicates the surface type, within the ones available in the program. The final entry is a numerical coefficient of the equation of the surface, in their proper order.

The surfaces can be defined as equations, points or macrobodies, and the format chosen for the example in Figure 17 was the latter. The macrobody surface is decomposed internally by MCNPX into surface equations and the facets are assigned individual numbers according to a predetermined sequence. The space inside a macrobody has a negative sense with respect to the macrobody surface and all its facets; and the space outside the macrobody has a positive sense.(55) In the example of Figure 17, the surfaces are all rectangular paralleliped (RPP). The first and second entries correspond to the X_{min} and X_{max} values, respectively. The third and fourth entries correspond to the Y_{min} and Y_{max}, respectively. The fifth and sixth entries correspond to the Z_{min} and Z_{max}, respectively. The surface 5 is therefore a rectangular paralleliped defined within the values of $-2 < X < 2$ cm, $-2 < Y < 2$ cm, and $0 < Z < 5$ cm. The surface 6 is also a rectangular paralleliped defined within the values of $-5 < X < 5$ cm, $-5 < Y < 5$ cm, and $-5 < Z < 10$ cm. Likewise, the surface 7 is also a rectangular paralleliped defined within the values of $-10 < X < 10$ cm, $-10 < Y < 10$ cm, and $-10 < Z < 30$ cm

It is also possible to specify spheres, hexagonal prisms, elliptical cylinder, and other geometries available in the program.

```
c ============= SURFACE CARD=========================================================
5     RPP -2 2 -2 2 0 5          $ water
6     RPP -5 5 -5 5 -5 10        $ air
7     RPP -10 10 -10 10 -10 30 $ space to run the problem
```

Figure 17 *Example of a surface card specification.*

Data card

The data card must contain information about the physics (mode used), cell and surface parameters (importance of the particles), source definition, tally specification, material specification and problem termination. It is also possible to define the importance of the particles in the cell card, which we have done in the example.

All the particles that will be transported in the problem should be specified in the mode card. If a particle is designated, the anti-particle will also be transported.

The material specification, m, is done with the *zaid* and the fraction of the elements. The *zaid* is composed by ZZZAAA, where ZZZ is the atomic number and AAA is the atomic mass number. As shown in Figure 18, the oxygen *zaid* is 8016 (atom number 8 and mass number 16) and the hydrogen *zaid* is 1001 (atom number 1 and mass number 1). The fraction of the elements can be specified in terms of atomic fraction or the weight fraction. In the example of Figure 18, the material 1 is water (H_2O) and the fraction was specified in terms of atomic fraction, meaning that there are 2 atoms of hydrogen and 1 atom of oxygen. The material 2 is air and was specified in terms of weight fraction, meaning that the material is composed by 70.08% of nitrogen, 20.92% of oxygen and 9% of argon. Although it is possible to specify the materials in these two ways, they should not be mixed within the same material card.

The source is specified in the SDEF card and, in the example problem of Figure 18, the particle specification is done by the entry “par=h”, where H is protons. The energy is set by the ERG entry and was set to 100 MeV. The position of the source is defined by the coordinates in X, Y and Z, and it was set to (0,0, -1) cm. The entry VEC specifies the reference vector for the direction of the beam. The entries of VEC are the cosine of the angles between the beam direction and the X, Y and Z-axis. In the example of Figure 18, these three entries are (0,0,1), which defines a beam along the Z direction. The entry DIR=1, specifies that the beam will propagate along the positive direction defined by VEC.

The problem cut-off card was defined by the number of particles sent, by the NPS entry. This number specifies the number of histories to be run in the problem. In the case of Figure 18, the cut-off was defined as “nps 50000”, meaning that the problem will stop when the program follows 50000 initial particles sent. This can also be done regarding other parameters such as the simulation time and the minimum cut-off energy. (55)

The PRDMP card specifies the print and dump cycle card. In this card it is possible to specify the writing of the MCTAL file, where the tally results are presented. The Print card allows to print the tables that should be included in the output file. By not specifying one number, the program will write all the table information available.

```
c =============== DATA CARD ============================================================
mode   H
m1     1001 2 8016 1                          $ H2O
m2     7014 -0.7008 8016 -0.2092 18040 -0.09  $ air
sdef par=h erg=100 x=0 y=0 z=-1 vec=0 0 1 dir=1
F6:H   1                                      $ averaged energy deposition across cell 1
TMESH
RMESH3 TOTAL
CORA3 -2 19i 2
CORB3 -2 19i 2
CORC3  0 24i 5
ENDMD
nps 50000
PRDMP 2J 1 1 1
Print
```

Figure 18 *Example of a data card.*

6.1.2. Scoring with MCNPX

The tallies in MCNPX can be used in different ways, depending on the desired results. This work is focused on tallies to calculate the primary and secondary dose.

Surface and cell tallies

This functionality allows us to obtain results from the INP file, in terms of energy deposition, flux or current. These tallies present their results as an average over a cell or surface and their usage should be considered regarding the significance of the results. Although there are various tallies available, the most used are the F4 and F6.

The F4 tally is a flux tally over a cell and gives results in particles/cm^2, for specific or multiple particles.

The F6 tally gives energy deposition averaged over a cell, in units of MeV/g, for specific or multiple particles. This is the tally used in Figure 18, where we want to determine the energy deposition in cell 1. MCNPX can also calculate the collision heating (+F6) tally, which contains energy deposition from all particles in the problem.

Mesh tally

The mesh tallies can be used to compare different particle contributions to overall results. This is a method to graphically display tally results such as particle tracks, energy deposition, flux, dose, or other quantities. This mesh tally can have rectangular, cylindrical, or spherical shapes and it is super-imposed on top of the standard problem geometry, allowing us to track the particles of the problem through an independent mesh. There are three types of tallies: type 1, type 2 and type 3, the first and third one being the most used.

The tally 1 can score flux, fluence or current from one or multiple particles. In this tally, when using the word FLUX, the results are a flux-based tally, which gives results in purely flux, or

number of particles/cm^2/second per source particle. When using the word PEDEP, the tally scores the average energy deposition per unit volume, MeV/cm^3/source particle.

The type 3 is an energy deposition TMESH mesh tally. This one scores energy deposition, taking into consideration the energy deposited per unit volume from all particles in the problem. This can be due to the slowing of a charged particle, the recoil of a nucleus, energy deposited locally for particles born but not tracked, etc. The normalization of the output is per unit volume, MeV/cm^3/source particle. In the mesh tally type 3, the energy deposition is obtained from all the particles in the problem where, in the mesh tally type 1, the energy deposition is obtained for a particle type required.

In terms of the resultant energy unit's presentation, the tally F6 is analogous to the use of a PEDEP keyword in the Type 1 mesh tally (this keyword permits the choice of considering different particles) and the +F6 tally is analogous to the Type 3 mesh, although the normalization is different. Since the mesh tallies score energy deposition within a mesh cell, which may contain more than one material, normalization is per unit volume. The units of this tally are MeV/source-particle. In the F6 and +F6 tallies, material density is available for the chosen cells, and normalization is MeV/g/source-particle.

Neutron doses calculation

The calculation of neutron doses can be done with an F4 tally or a TMESH tally type 1. In both options, the particle type needs to be specified and flux-to-dose conversion factors applied. The conversion factors are used to make a relationship between protection and operational quantities to physical quantities that characterize the radiation field, for both internal and external radiation exposure. (2,30)

To achieve this, dose function (DF) and dose energy (DE) cards are used. The entries on the DE and DF card make a correlation between the energy value (in MeV) and the value of dose function corresponding to it. So, the first entry on DE card, corresponds to the first entry on DF card, the second entry on DE card, corresponds to the second entry on DF card, and so on. The code multiplies the entries of DE by the entries of DF, does generating a conversion between energy and dose values.

The neutron dose was calculated in terms of ambient dose equivalent (H*(10)) by inserting the flux-to-dose conversion factors of ICRP-74 (58) and in terms of Effective dose (E) by inserting the flux-to-dose conversion factors in antero-posterior direction of ICRP 116. The E antero-posterior (AP) was used because this may be considered more conservative for high energy neutrons. (19)

7. The Bragg Peak

In this chapter it will be described the Bragg Peak curve and presented multiple simulations obtained with MCNPX, aiming to illustrate the theoretical physical proton beam interactions descripted. By using MCNPX tools, we will demonstrate the Bragg peak and the Spread-out Bragg peak, as well as the lateral scattering of a proton beam. Further, it will be analysed the impact of protons interactions with different materials in the beam path.

The results of those simulations are obtained inside a calculation grid superimposed in the assembly. This calculation grid can have cubical, spherical, or rectangular shapes, depending on the user assignment and specification. It represents a volume, inside which, the software will perform the calculations. The accuracy of those calculations is as bigger, as smaller the volume of the pixel geometry. The calculation grid is created by a number of intervals in the X, Y and Z-direction. The number of intervals on the X-direction is the number of segments created by the software in the lateral direction of the grid. The number of intervals on Y-direction correspond to the number of segments created in the longitudinal direction, and the number of intervals in the Z-direction correspond to the number of segments created in the vertical direction of the grid. As an example of Figure 19, we show a cubic calculation grid where the values of X, Y and Z are ranging between -2 and 2 cm, equally spaced by 0,4 cm in all directions. This means that the calculation grid has a volume of $0.4 \times 0.4 \times 0.4\ cm^3 = 0.064\ cm^3$ per voxel.

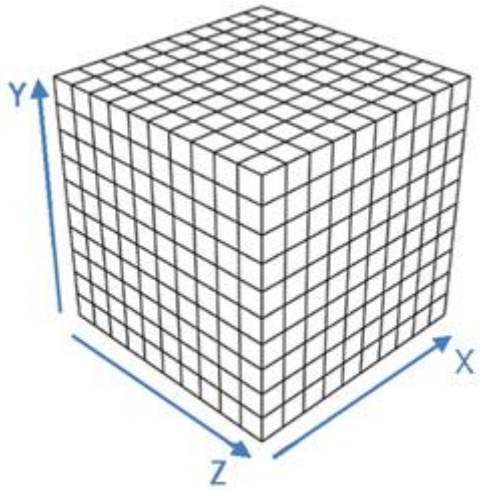

Figure 19 *Display of 3D grid of voxels* (31)

7.1. Longitudinal profile

The proton beam interacts with matter by the mechanisms described on chapter 2 and produces a dose distribution along its path. The increase of energy deposition of charged particles with penetration, forms a maximum nearly before this energy deposition decreases substantially. This region is called the Bragg peak, illustrated in Figure 20.

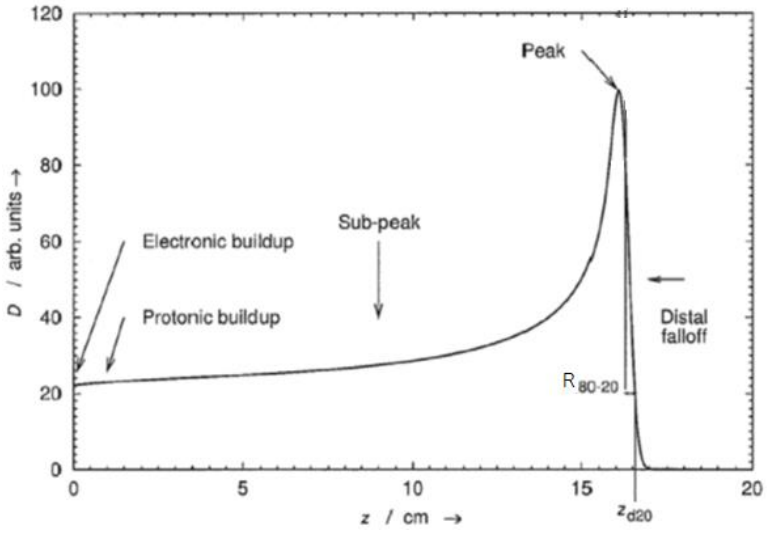

Figure 20 Absorbed dose, D, as function of depth, Z, of a 154 MeV pristine proton Bragg peak, in water. Adapted from (7)

The shape and distribution of the Bragg peak results from the combination of different aspects. The electronic build-up region is due to the proton's Coulomb interactions with atomic electrons that result in a loss of protons' energy. That region is followed by the protonic build-up, where the absorbed dose increases with depth due to build-up of secondary protons.

This energy distribution is not done equally at all depths. The average energy transferred from a charged particle per unit distance into the medium is called linear energy transfer (LET, or "stopping power"). The LET for protons is given by the Bethe-Bloch formula, as presented before. (3) When crossing a material, each beam particle with the same initial energy suffers a different set of interactions and has a specific distribution of energies after crossing a thickness of absorber; this process is known as energy straggling. Along with this, it can also be seen that the particles have a resulting distribution of depths at which they stop, called range straggling. The rate of energy loss of a charged particle is proportional to the square of its charge and approximately inversely proportional to the square of its velocity. This phenomenon contributes to the sub-peak region, along with nuclear reactions. This sub-peak region is also known as plateau. When a particle traverses' matter, its rate of energy loss increases until, at very low velocities, it captures

an electron, decreasing its effective charge. The average rate of energy loss consequently decreases at very low velocities, creating the Bragg peak.(21)

The distal fall-off region is the distance between the distal 80% and distal 20% depths, represented in the image as R_{80-20}.

At the distance of R_{80}, the edge of the Bragg peak is very similar to the same depth as the 50% fluence, on the fluence distribution. This means that at the distance R_{80}, 50% of the initial protons already deposited their energy before this point and 50% of the sent protons will deposit their energy after that. (3)

Ideally, the peak of the Bragg curve should be very sharp and the decrease in energy should be very abrupt after reaching the maximum energy. In fact, there are some effects that make this impossible. There are statistical fluctuations in the ionization processes that cause range straggling, typically by about 1% of their range. Besides that, it is almost impossible to have a monoenergetic proton beam. There is always some energy spread due to details of the protons' production, typically of the order of 1%. These two effects combine in a near-Gaussian spread function and spread out the near-infinitely sharp ionization peak, resulting in the broader, more rounded, and more symmetric peak. (3)

To investigate the lateral energy spread along the proton beam path and in the Bragg Peak region it was performed a simulation on MCNPX. The graphical display of its behavior is shown in Figure 21 and Figure 22.

In Figure 21 we represent a bi-dimensional (2D) and tri-dimensional (3D) representation of a Bragg peak in a water phantom. This beam has a gaussian distribution with $\sigma_x = \sigma_y = 0.24\ cm$ and lateral dimensions of 1×1 cm. The calculation grid has a volume of $6 \times 0.075 \times 0.5\ cm = 0.225\ cm^3$. See chapter 8 for more explanations about the beam sigma (σ) dimensions.

Each particle loses more energy at the position of the Bragg peak than at the entrance. However, at the entrance, there are many more particles at the center (higher fluence) because of the gaussian particle distribution. This means that there are a lot of particles in a smaller surface but losing less energy. At the position of the Bragg peak, the particles are losing more energy but spread over a larger surface (lower fluence). The combination of the 2 effects results in the graphical representation presented.

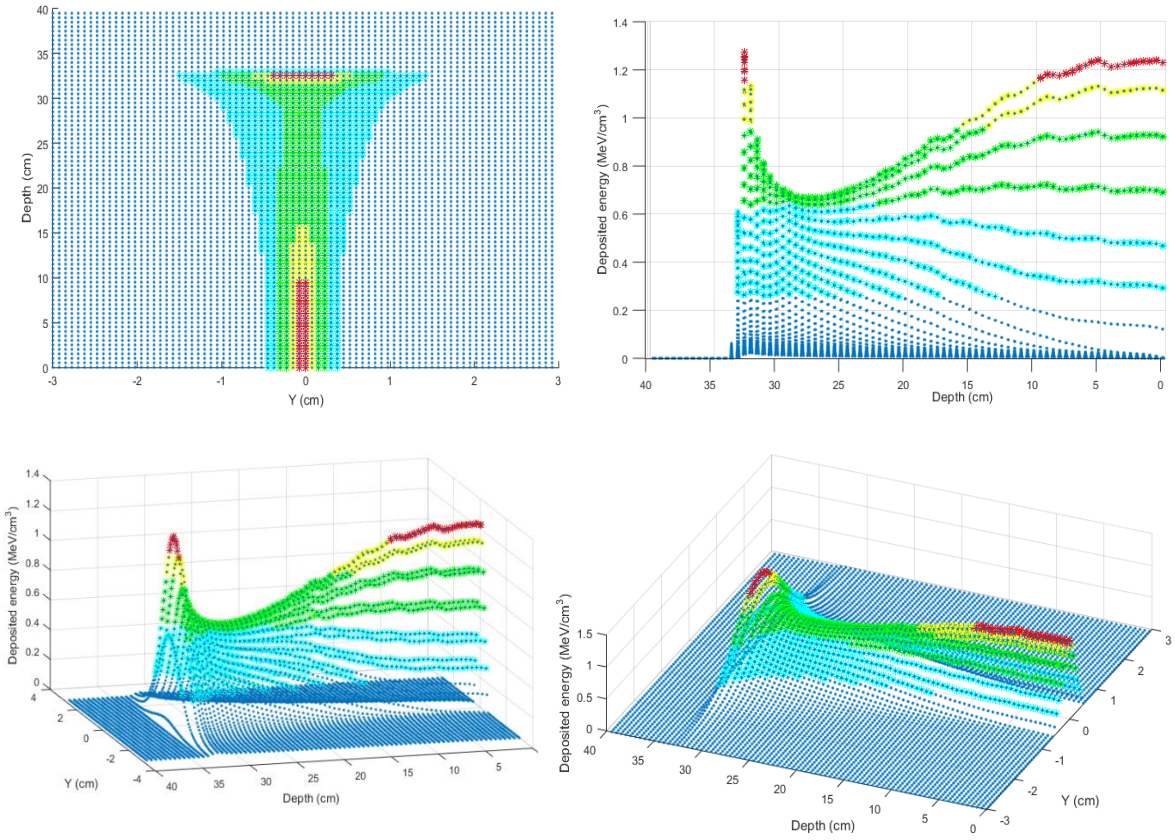

Figure 21 2D and 3D representation of the Bragg peak from a beam with gaussian fluence distribution. The red represents the area where the deposited energy is superior to 90% of the maximum deposited energy. The yellow / green / cyan / dark blue represents the area where the deposited energy is between 90% and 75% / 75% and 50% / 50 and 20%/ inferior to 20% of the maximum deposited energy.

This effect shown in Figure 21 is the behavior of a single pencil beam in water. To decrease the entrance dose in the central area, it is necessary to have multiple beams, side to side, to create a distribution as in Figure 20.

In the Figure 22 a 2D and 3D representation of a Bragg peak is presented, in a water phantom. This beam has a uniform fluence distribution and dimensions of $1 \times 1\ cm$. The calculation grid has a volume of $6 \times 0.075 \times 0.5 = 0.225\ cm^3$.

In this example, the particles lose their energy over a large surface at entrance. This explains why the entrance dose is lower than in the previous figure.

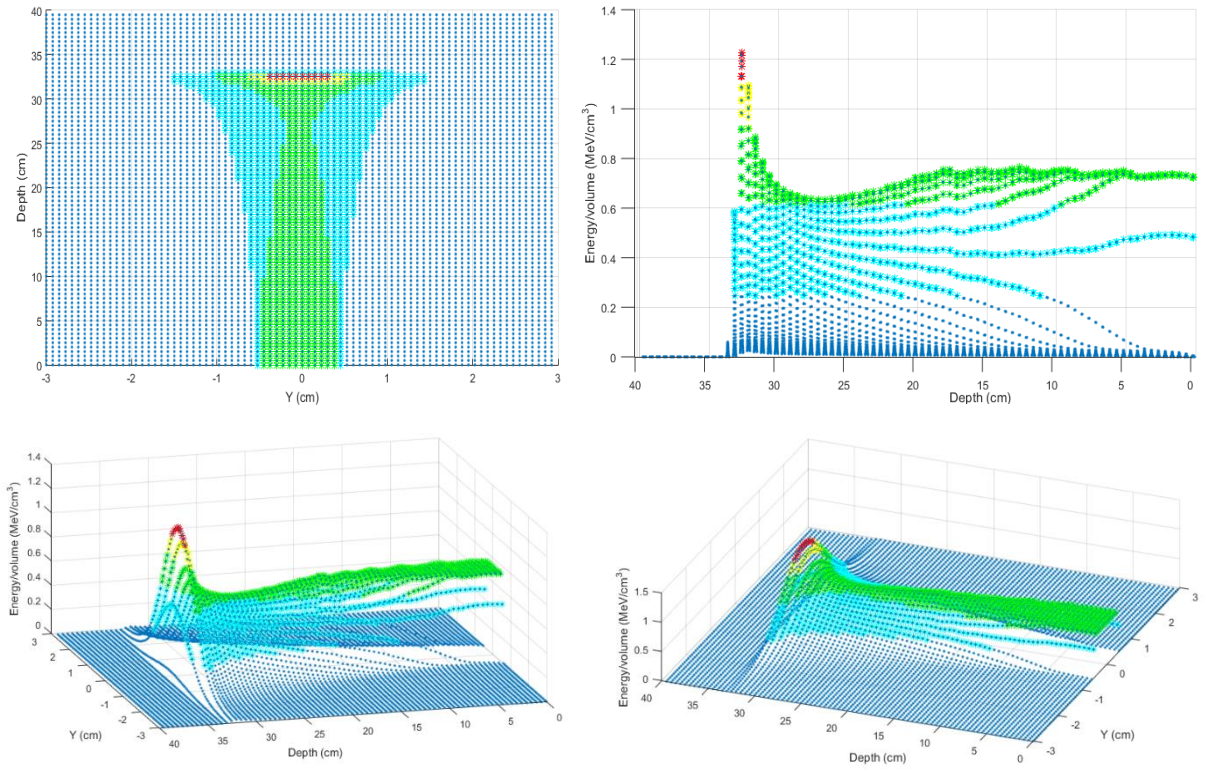

Figure 22 2D and 3D representation of the Bragg peak from a beam with uniform. The red represents the area where the deposited energy is superior to 90% of the maximum deposited energy. The yellow / green / cyan / dark blue represents the area where the deposited energy is between 90% and 75% / 75% and 50% / 50 and 20%/ inferior to 20% of the maximum deposited energy.

7.1.1. The Spread-out Bragg peak

In 1946, Robert Wilson suggested that the dose distributions of mono-energetic proton beams could be combined to deliver dose to larger tumors volumes, using a combination of pristine Bragg peaks with different ranges and ponderations. The tumor volumes have irregular shapes and can extend many centimeters in length and width, and this technique emerged to produce homogeneous dose distributions at the target volume with low doses in the surrounding healthy tissues. (3)

Figure 23 shows a spread-out Bragg peak (SOBP) that provides a uniform dose distribution in depth across the target volume, represented by darker grey area. This effect comes along with a sharp fall-off which thus spares normal tissue behind the target volume, represented by the light grey area. (3,19)

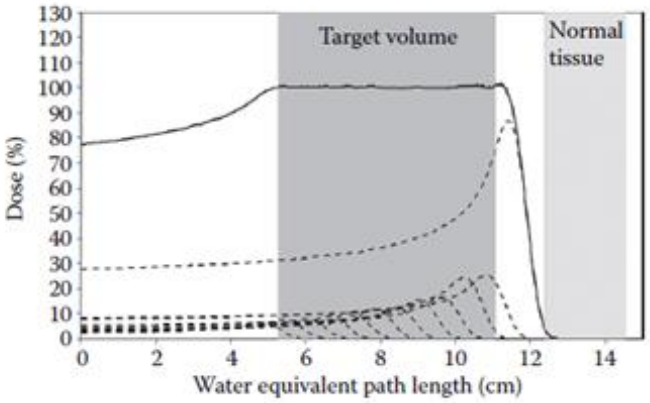

Figure 23 Schematic view of SOBP, showing the SOBP depth-dose distribution (solid line) and the component Bragg peaks (dashed lines). (7)

The entrance dose, on the proximal side of the SOBP, depends on the extent in depth of the SOBP. This total entrance dose can increase from 30% to nearly 80% due to the deepest Bragg peak. As described before, the flux of protons at a point at distance r from the source decreases by the law of the inverse-square, by a factor of $1/r^2$. The decrease of dose at larger depths makes it necessary to adjust the weights of the upstream Bragg peaks, leading to an increase of the entrance dose. In practical terms, this causes the dose sparing of the proximal tissues to decrease with shorter distances from the source to the patient and, for that reason, it's recommended that, in proton therapy facilities, the source stays at 2-3 meters away from the isocenter. (3) Besides this, the irradiation of tissues with SOBP produces superior dose distributions compared to a photon beam from a typical linear accelerator. (3,19)

In an article of Sayah R. et al., (32), the authors described the creation of an SOBP, by using a range modulator wheel (RMW) (for more information about this technique, report to chapter 6.1). This technique uses different modulator steps, made of various thicknesses of Lexan and Lead to achieve a modulation in depth. A weighting factor is associated to each modulation step to produce a homogeneous dose distribution. This information is summarized in Table 3.

We used the MCNPX program to confirm the authors' results report and validate the simulation method. In this simulation, we used a proton beam with 178.16 MeV, at the exit of the nozzle. 3×10^6 source protons were tracked in each simulation to achieve a statistical uncertainty on the deposited energies of less than 2%.

Table 3 *Lexan and Lead thickness of each modulator step and associated weighting factors*

Modulator step	Modulator thickness (cm)		Weighting factor
	Lexan thickness	Lead Thickness	
1	0.106	0.317	0.382
2	0.791	0.297	0.145
3	0.152	0.269	0.099
4	2.164	0.256	0.079
5	2.887	0.229	0.076
6	3.531	0.216	0.065
7	4.209	0.197	0.056
8	4.918	0.172	0.048
9	5.562	0.160	0.045
10	6.262	0.136	0.005

In Figure 24 we represent the resultant SOBP and each individual Bragg peak that contributed to the spatial dose distribution. The SOBP was normalized to 100% of the dose. The contribution of each individual Bragg peak, or its weighting factor, is not equal between the beams and its values were the same as reported per the authors. To achieve a flatter SOBP in the plateau region, the individual weight should be optimized.

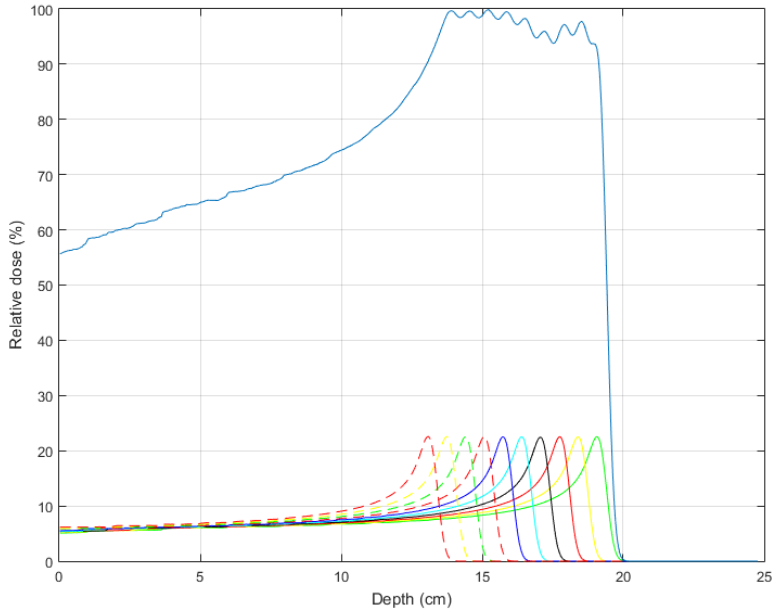

Figure 24 *SOBP resultant from the combination of contributions of each individual Bragg peak.*

7.2. Lateral scattering

The accurate evaluation of the lateral dose profile is an important issue in proton therapy as the lateral scattering can increase range uncertainties of proton.

MCS is the principal cause of the spreading out of a pencil beam. This effect causes a nearly Gaussian distribution in the angle of deviation and in the lateral spread of the pencil beam. Near the end of the path of protons, the standard deviation of the lateral distribution is about 2% of the range. (3)

The MCS of the beam particles, accounts only for electromagnetic interactions between the beam particles and the irradiated materials while the global transverse dose profile, which also accounts for the contribution of nuclear interactions, is generally approximated by a sum of Gaussian functions by most Treatment Planning Systems (TPSs). (33) This approach achieves a good compromise between accuracy and computing efficiency while efforts are being made to decrease the computation time.

The pencil beam is also broadened due to interactions within the target and with the upstream material. For large proton penetrations, the lateral penumbra near the end of the range is dominated by scattering in the target material. In contrast, for small proton penetrations, the lateral penumbra is usually dominated by blurring effects that occur upstream of the patient. (3) In Figure 25 the principal contributions to the dose at different points are summarized.

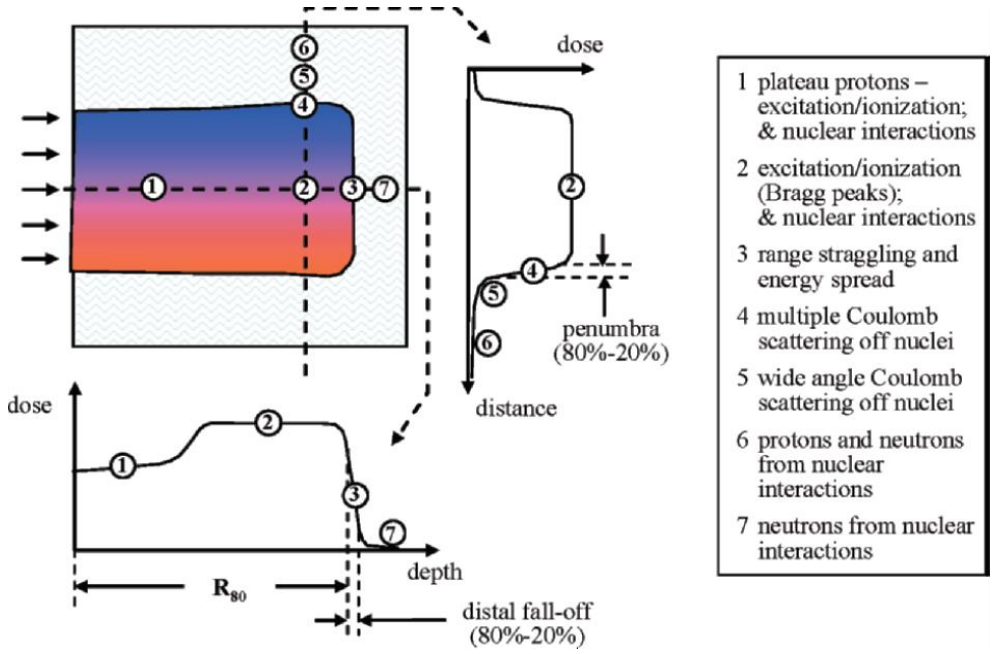

Figure 25 Synopsis of the principal contributions to the dose at various points within and outside a broad pencil beam (3)

To study lateral scattering, a proton beam with 100 MeV and 230 MeV was simulated, incident in a water phantom. Three different beam scenarios were considered, and the grid calculation is equal in both energy simulations, with a value of $10 \times 0.1 \times 0.1 = 0.1\ cm^3$. Every simulation was made with 3×10^6 particles, taking about 47 minutes to compute each one. Due to the high number of particles followed, the maximum relative error of the deposited energy associated to the simulations was 0.013 %. The total energy deposition is given by the integral of all the curves presented.

The first scenario is a beamlet composed by particles considered monoenergetic, parallel, and uniformly distributed through an infinitesimally small cross-sectional area dx/dy, traveling along Z-axis direction, in the positive sense. The result of the lateral scattering is presented in Figure 26 for both simulated energies.

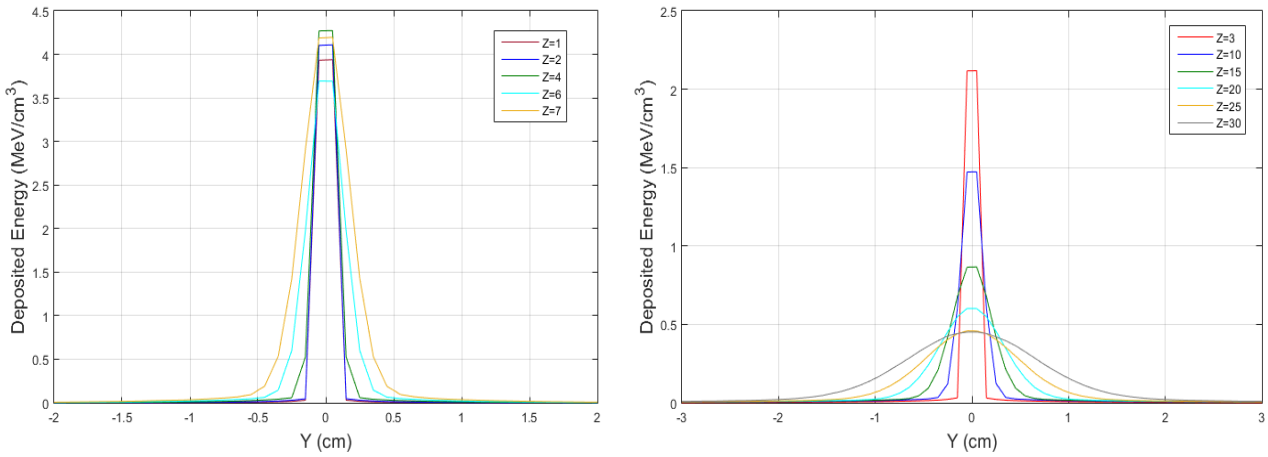

Figure 26 Simulation of lateral scattering of 100 MeV (on the left) and 230 MeV (on the right) beamlet. The beamlet has no lateral distribution.

In Figure 27 is shown the energy distribution at each depth (Z-axis value) in the material. As we move along in the Z-axis, the lateral scattering increases for both energies. If we compare the results from both energies, we can observe that the lateral scattering is increased for bigger energies. For a proton beam with 100 MeV, the Bragg Peak happens at Z=7.62 cm and with 230 MeV it happens at Z=32.65 cm. The results shown in the graph are only until the Bragg peak region, because after that depth value the results of deposited energy are approximately zero.

The second scenario consists in a beam with uniform particle distribution, with dimensions of 1 cm, in both X and Y-axis. The center of the beam coincides with the water phantom axis and

the particles travel along the Z-axis, in the positive sense. Figure 27 present the results of this simulation, for both simulated energies.

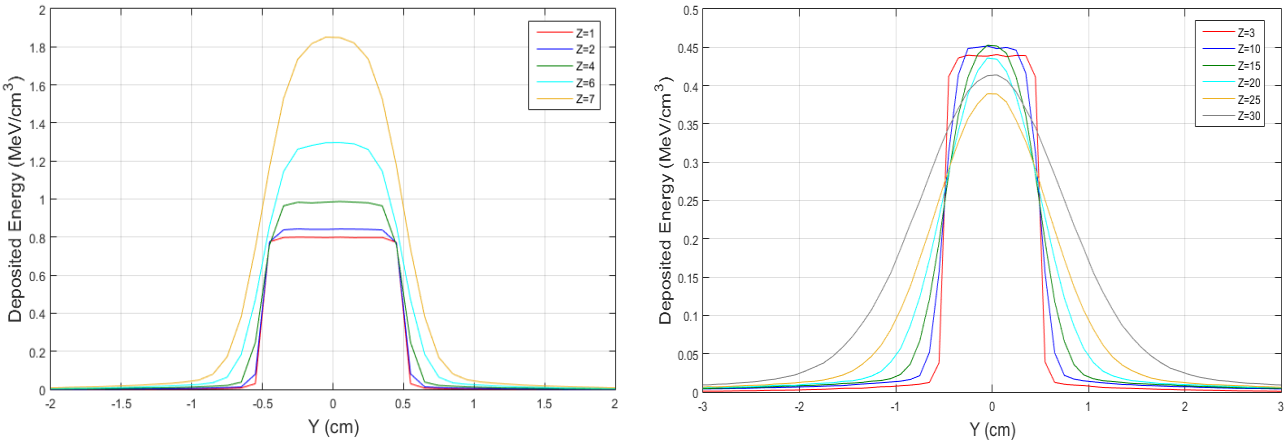

Figure 27 Simulation of lateral scattering of 100 MeV (on the left) and 230 MeV (on the right) beam with uniform particle distribution.

The third scenario is a beam with the same dimensions of the second scenario, but with gaussian fluence distribution. The beam sigma (σ) values used were the same in both directions, $\sigma_x = \sigma_y = 0.24\ cm$. To more detail in the sigma determination, please report to section 8.1. The results of this simulation are presented in Figure 28 for both energies.

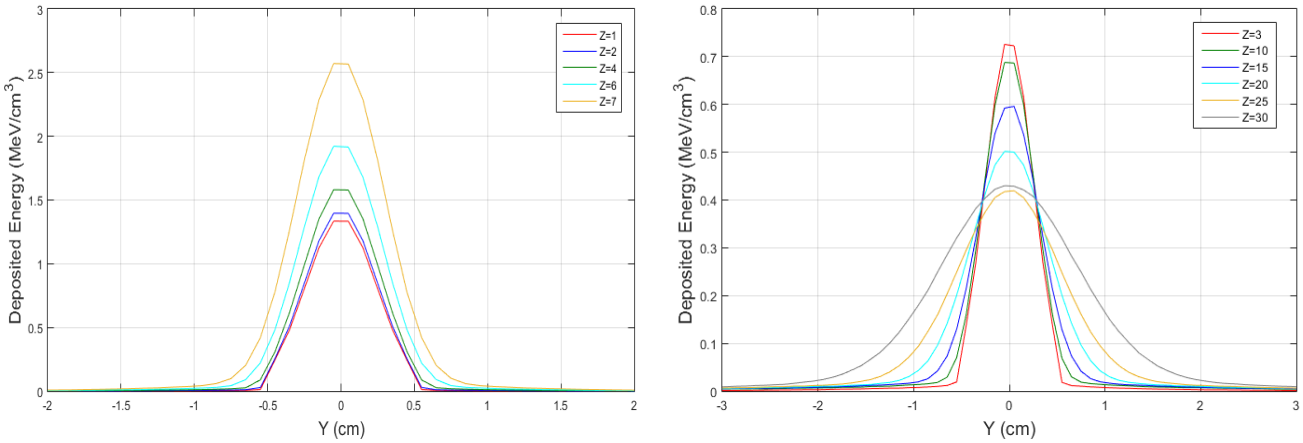

Figure 28 Simulation of lateral scattering of 100 MeV (on the left) and 230 MeV (on the right) beam with gaussian fluence distribution (δ_x=δ_y=0.24 cm).

In the figures above it is possible to observe that the lateral energy profile increases with the distance to the origin, until the Bragg peak area.

The penumbra width was calculated for both energy beams with gaussian distribution. The penumbra width is the distance between d_{80} and d_{20}. The d_{80} represents a point in the graph, where the deposited energy is 80% of the maximum deposited graph. Similarly, d_{20} represents a point in the graph, where the deposited energy is 20% of the maximum deposited graph. Because we are dealing with a gaussian distribution, there will be two values, one on the right and one on

the left of the central maximum, for d_{80} and d_{20}. Because the curve behaviour is similar in both positive and negative sides of the graph, we will only consider the values of the positive side.

The values for the 100 MeV energy beam are presented in

Table 4 and the values for 230 MeV energy beam are presented in Table 5. These results highlight that the bigger the proton beam energy, the bigger the range of these particles in the material. As the protons go through the material, there is more lateral scattering resulting in a larger spot.

The lateral spreading of a proton beam at the Bragg peak is about 1.5% of its range, independent of the proton energy. (3)

Table 4 Values of d_{80}, d_{20} and penumbra width determination at different depths in water, for a beam with gaussian distribution and energy of 100 MeV.

Z (cm)	d_{80} (cm)	d_{20} (cm)	$Penumbra\ width\ (d_{80} - d_{20})$ (cm)
2	0.15	0.35	0.2
4	0.15	0.35	0.2
7	0.15	0.45	0.3

Table 5 Values of d_{80}, d_{20} and penumbra width determination at different depths in water, for a beam with gaussian distribution and energy of 100 MeV.

Z (cm)	d_{80} (cm)	d_{20} (cm)	$Penumbra\ width(d_{80} - d_{20})$ (cm)
10	0.15	0.45	0.3
20	0.25	0.65	0.4
30	0.45	1.25	0.8

In a study of Loushab E. et al (2015) (1), the authors aimed at calculating the effects of the energy, shape, and type of ion beams (proton and carbon-ion) incident upon water, by using a Monte Carlo simulator. The authors simulated a mono-energetic pencil beam with protons (energies ranging from 50 to 230 MeV), and with carbon ions (energies ranging from 1101 to 4632 MeV). The energies used establish a one-to-one correspondence in range between the two particles. The results show that the transversal scattering of dose distribution is increased with energy at the end of a heavy ion beam range. It can also be seen that the amount of dose scattering for a carbon-ion beam is less than that of a proton beam, due to the bigger mass of carbon ions. It was also highlighted that although carbon-ions are primarily scattered less than protons, the corresponding dose distributions, especially the lateral dose, are not much less. This phenomenon occurs because carbon-ions generate more secondary particles than protons. The

results presented are valid up to 16 cm depth in water. For deeper penetrations or seated tumors, protons seem to be more effective. (1)

7.3. Interaction with matter

7.3.1. Simulation in homogeneous conditions

To access the range and the maximum deposited energy in homogeneous conditions, a scenario using one water phantom with dimensions of $10\ cm \times 10\ cm \times 40\ cm$ was simulated, whose center coincided with the Z-axis. The irradiation source was a mono-energetic beam, with no lateral distribution, starting at coordinate (0,0,0) and moving along in the Z-axis, in the positive direction. The simulations were performed for each energy, using 3×10^6 particles and took 45 minutes each, in average. The calculation grid had a value of $10\ cm \times 10\ cm \times 0.02\ cm = 2\ cm^3$. Due to the high number of particles used, the maximum relative error of deposited energies associated was 0.014%.

The numerical results are presented in Table 6 and the longitudinal profile of deposited energy distribution, as function of depth, is presented in Figure 29. It is possible to observe that, with an increase of energy, the protons range is also increased. On the other hand, with the increase of proton beam energy, the maximum deposited energy at the Bragg peak curve is decreased.

Table 6 Simulation results of the maximum deposited energy (MeV/cm^3), R_{100} (cm) and R_{80} (cm) from proton beams with energies ranging from 50 MeV to 230 MeV.

Incident beam energy (MeV)	50	80	110	140	170	200	230
Maximum deposited energy (MeV/cm^3)	0.6843	0.4819	0.3655	0.2925	0.2402	0.2016	0.1711
R_{100} (cm)	2.21	5.13	9.05	13.87	19.45	25.73	32.65
R_{80} (cm)	2.21	5.17	9.15	13.99	19.65	25.99	32.97

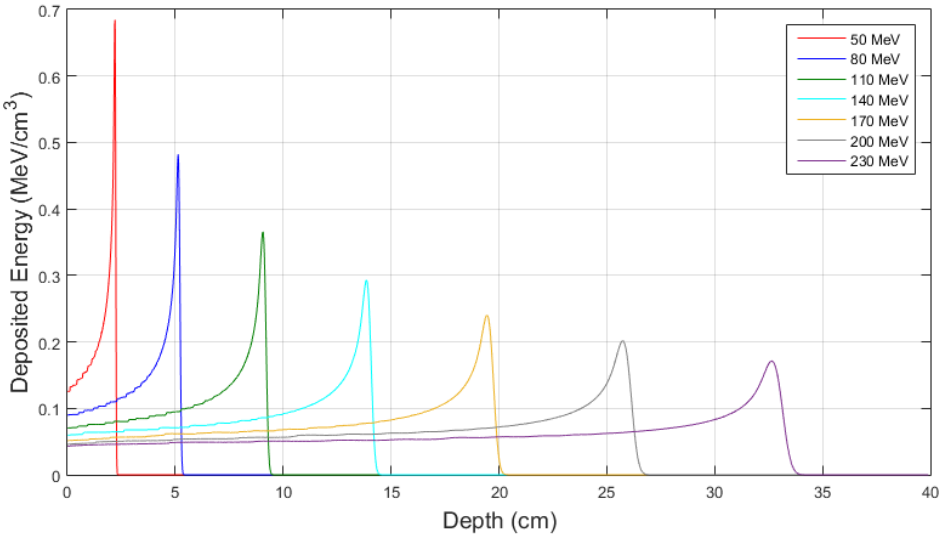

Figure 29 *Longitudinal representation of simulated Bragg peak, with beam energies between 50 MeV and 230 MeV.*

In Table 7 a comparison is made between the range results from different proton beam energies simulated in MCNPX, with the values reported in the literature. A percentual difference between the results Is presented, calculated as following:

$$\text{Difference (\%)} = \frac{|\text{this work results} - \text{literature results}|}{literature\ results} \times 100 \tag{3.1}$$

The range results of the measurements obtained by Han et al. (34), were acquired at the 10% maximum point on the energy deposition curve, according to IAEA technical report recommendations. (34,35) For this reason, the comparison of the results was done to R_{10} distal values for the proton beams simulated in the present work. The comparison can be seen in Table 7 and the maximum percentual difference observed was 2.1%. In their work, the authors compared the range measurements with NIST results and the percentual differences were less than 0.8%.

The range calculations presented by Janni, ICRU 49 and National Institute of Standards and Technology (NIST) were presented as CSDA calculation result and were compared with R_{80} values from the present work. (36,37) The difference between the MCNPX simulations and the literature results was less than 0.9%.

Table 7 Comparison of range results obtained from MCNP simulation with results reported in the literature. The maximum relative error associated was 1.34948×10^{-4}.

Energy (MeV)	This work			Janni(37)		Icru 49(37)		NIST(36)		Han et al., (2016) (34)	
	R100	R80	R10	Range (cm)	Difference (%)	Range (cm)	Difference (%)	Range (cm)	Difference (%)	Range (cm)	Difference (%)
80	5.130	5.210	5.270	5.236	-0.497	5.178	0.618	5.176	0.657		
110	9.050	9.150	9.330	9.226	-0.824	9.127	0.252	9.128	0.241		
150	15.630	15.790	16.070	15.919	-0.810	15.750	0.254	15.760	0.190	15.740	2.097
170	19.450	19.650	19.990	19.792	-0.717	19.594	0.286	19.590	0.306	19.650	1.730
190	23.550	23.790	24.230	23.974	-0.768	23.724	0.278	23.740	0.211	23.870	1.508
200	25.730	25.990	26.470	26.185	-0.745	25.929	0.235	25.930	0.231		
210	27.950	28.230	28.730	28.465	-0.826	28.192	0.135	28.190	0.142	28.370	1.269
230	32.650	32.970	33.550	33.221	-0.756	32.911	0.179	32.910	0.182	33.160	1.176

7.3.2. Simulation in inhomogeneous conditions

The need to account for heterogeneity on the dose distributions is more critical on PTR than in photon therapy since they result in range uncertainty and changes in lateral scattering of the primary particles in the patient and, consequently, that affects the dose fall-off. Heterogeneities can be present in the whole extension of the proton beam, may intercept part of that beam in the lateral direction or may be in a small region present in some part of the beam path. (19)

So-Hyun Park et al, (38) investigated the effects of heterogeneity structures (bone and adipose tissue) using Monte Carlo simulations. The authors placed the inhomogeneous material in the plateau region and proximal region of the Bragg peak, within a water phantom. Their results indicated that the location of inhomogeneous tissues does not affect the whole shape of the Bragg curve but affects the dose in the Bragg curve. When inserting bone with 1 cm thickness, the range decreases approximately 0.7 mm. The alterations of dose in the Bragg peak curve were more pronounced when inserting the bone material, which can be explained by the higher density of bone compared to adipose tissue (ρ=1.85 g/cm^3 and ρ=0.92 g/cm^3, respectively).

Shirmardi et al., (39) performed similar simulations as the previous authors, with the MCNPX code. They analyzed the range (R_{80}), FWHM and penumbra position (R_{20}) after inserting bone and adipose tissue inhomogeneities in the beam path. The results showed dose changes associated with the thickness or the density of inhomogeneous material in the Bragg curve. When inserting 1 cm of bone in the region of plateau and Bragg peak, the range was decreased by approximately 0.35 cm, but no such change would occur if we had inserted adipose tissue. By inserting the bone layers in the region of Plateau and Bragg peak, the R_{80} and R_{20} reduce. When adipose tissue with a 0.1 cm thickness is inserted in the region of Plateau and Bragg peak, the R_{80} and R_{20} reduce. The R_{80} is reduced from 8.87 to 8.78 cm and the R_{20} is reduced from 9.04 to 9.02 cm. By increasing the adipose thickness, the R_{80} and R_{20} increase. FWHM is always increased by increasing the inhomogeneity thickness of both materials. (39)

Bentefour E.H, et al., (27) performed *in vivo* proton beam measurements to validate a method for clinical situations. The main goal was to simulate a prostate irradiation, where the beam encounters different heterogeneities in its path (e.g., pubic bone, potential air cavities, bladder, bowels). In the paper, among other objectives, the authors investigated the effect of tissue heterogeneities by studying the range shifting and range mixing induced by inserts of inhomogeneous materials in a water phantom. (27) One of the measurements obtained was the determination of the range (defined at R_{80}) of a proton beam in water, and the determination of the R_{80} after inserting a block of bone equivalent material. The authors reported that after inserting two bone blocks with different thicknesses (4 and 0.5 cm) it's expected to have a pull back in the beam by 2.48 cm and 0.31 cm, respectively. Those values were verified by the authors in their measurements.

To be able to verify the authors results and compare the outputs, we recreated the simulation in MCNPX program. These studies were simulated in this work and all the relevant information given in the article was considered, to establish a meaningful comparison with literature results. The authors used a beam with a R_{80} of 18 cm. Because, in MCNPX, it is not possible to specify a beam by its range, it was necessary to determine which energy provides this

value of R_{80} in a water material. Due to this, in this experience, a proton beam with 162 MeV was used, which corresponds to a R_{80} of 18.05 cm in water. The longitudinal profile of these simulations is presented in Figure 30.

When the beam encounters a 0.5 cm thickness of bone equivalent material, his R80 is at 17.75 cm, corresponding to a difference of 0.3 cm from the reference. When the beam crosses the 4 cm thickness block of bone equivalent material, his R_{80} is situated at 16.25 cm, corresponding to a difference of 1.8 cm from the reference. These values, compared to the ones of Bentefour E.H, et al. (27), have a percentual difference of 0% for 0.5 cm of bone thickness and -27,42% for 4 cm bone thickness.

In Figure 30 its possible to observe the longitudinal profile of the proton beam in the different simulated scenarios. The red line represents the longitudinal profile of the 162 MeV proton beam in water, without interacting with any other material. It is possible to observe that this has the biggest range among all the simulated scenarios. The blue line represents the longitudinal profile of the proton beam in water after crossing a block with 0.5 cm, made of bone equivalent material. It is possible to observe that this structure was positioned at 3<Z<3.5 cm, producing a perturbation in the deposited energy line. The green line represents the longitudinal profile of the proton beam in water after crossing a block with 4 cm, made of bone equivalent material. As with the blue line, is possible to observe that the block produced a perturbation in the deposited energy curve and it was positioned at 3<Z<7 cm. This line is the one with smaller range, since the proton beam crosses a material with bigger thickness than in the scenario represented in the blue line.

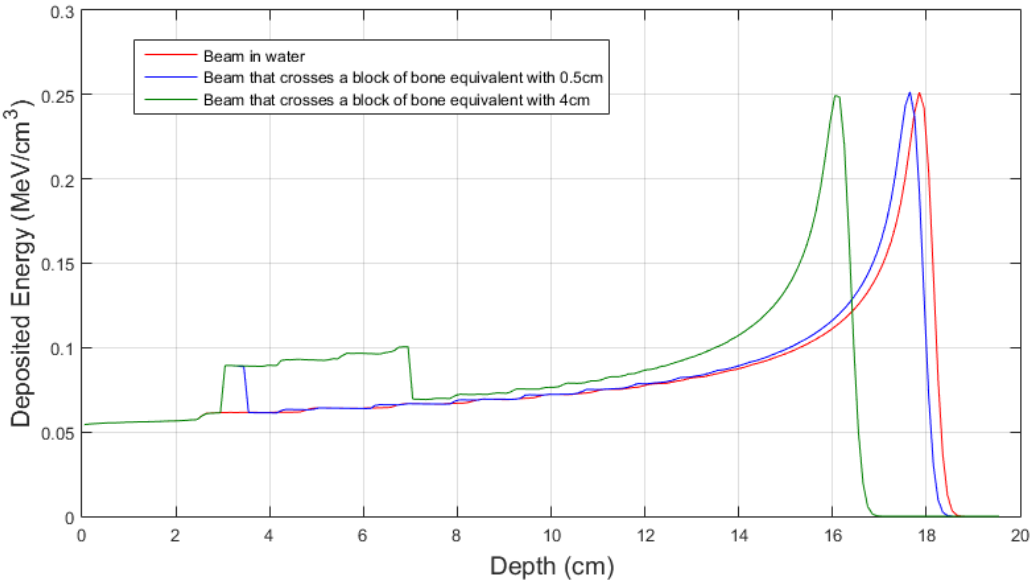

Figure 30 Deposited energy (MeV/cm³) results for the experiment recreation of Bentefour E.H (2012). The red line represents the longitudinal profile of the beam in water, without any interaction. The blue line represents the longitudinal profile of the beam after crossing 0.5 cm of bone equivalent material. The green line represents the longitudinal profile of the beam after crossing 4 cm of bone equivalent material.

As discussed above, the uncertainty in the protons range can arise from the lack of knowledge on the energy distribution or in the properties of all the range absorbers materials, such as the elemental composition, mass density and linear stopping power, in the beam path.(7) In this specific case, the elemental composition of the bone equivalent material was not given in detail by the authors. The mass density used was mentioned and considered in this simulation repetition, but the elemental composition was obtained from online library NIST(40). This reason can be the explanation for the difference seen in the results.

The simulations performed in MCNPX allowed us to review and verify the previous presented concepts. This tool, not only allowed the understanding of theorical concepts, its also supported the validation of published literature. This way, we can conclude that the coding tools of the Monte Carlo simulator are mastered in a certain level that allow us to trust in the future results from the uncertainty tests (chapter 9) and discuss them credibly.

8. Material and methods

In this chapter we will introduce the physical components simulated and the characteristics and specifications that justify their choice in the present context. It is important to mention that this is a subject under investigation and, because of this, the choices made while the thesis was being written may have underwent changes during that period.

8.1. Beam parameters

Protons in a beamlet incident on a patient or a phantom are very nearly monoenergetic and are distributed laterally essentially as a narrow Gaussian function of position relative to the beam's central axis. The lateral dimension of a beam is expressed in terms of the full-width-at-half-maximum (FWHM) of the Gaussian, or its standard deviation, σ. A smaller FWHM is desirable since it allows for a sharper penumbra and better dose distributions. In air, higher energy proton pencil beams have a smaller FWHM than the lower energy ones. Typically, the smallest achievable FWHMs in air for the highest energies (220 to 250 MeV) range from 7 to 12 mm (or σ of 3 to 5 mm) depending on the vendor and the machine model. Once the pencil beam enters a medium, such as a phantom or a patient, the FWHM increases substantially, especially near the end of the range of protons. (4)

For the IBA machine specification, it's known that the fluence, at the exit of the nozzle, has an elliptical shape. Which means that the σ in the X-direction is different from the σ in the Y-direction. This ellipse suffers scattering by interacting with the range shifter and the other materials in the path and becomes a circular gaussian.

8.2. Range shifter

The range shifter is a passive beam modifier. This is typically used to treat volumes at reduced depths using PBS since it may be clinically preferable to use a beam energy degrader than beam protons with less energy, due to wider Bragg peaks. This requires less energy layers and small spot sizes, since the spot size after the range shifter is larger. In addition, its utilization may be mandatory in cases where the lower energy available is not low enough to treat superficial volumes. (59)

Usually, it is a slice of plastic material located between the nozzle and the patient, as close as possible to the patient to minimize scattering of protons.

8.3. Ridge filter

The 3D non-uniform ridge filter (also called Conformal Energy Filter (CEF) or “hedgehog”), is obtained from treatment plans based on PBS technique and the use of a SOBP in the tumor. This approach has been confirmed by measurements that a ridge filter could be used to investigate possible FLASH effects in SOBP regions. (60) This applicator is designed and manufactured in a 3D printed plastic using a 3D printer. There are some studies that support the feasibility of this approach in PTR, highlighting the physical accuracy and dosimetrical characteristics compared to conventional compensators. (61–63) It is also known that the SOBP homogeneity strongly depends on the manufacturers accuracy to reproduce the CEF and that dose deviations tend to be observed most frequently in the distal SOBP edge, due to the higher difficulty in creating the area between the base towers.(60)

The use of 3D range modulators led to a decrease in the number of cyclotron energies used and the treatment time. In a study by Simeonov et al, (15) the authors used a 3D range modulator to irradiate a volume of 5 cm of diameter, placed at 25 cm depth in water, with a monoenergetic beam, during 3 seconds. In this study, the authors compared MC simulations with measurements obtained with a prototype, obtaining a good agreement between the simulations and measurements. According to the authors, a comparable dosimetrical plan with the same number of particles will need to use 16 energies to cover the irradiated volume. This will take 60-80 seconds of irradiation, which is approximately 20 times the irradiation time obtained with this 3D range modulator.(15) This technique has proven to be very promising in irradiating moving targets, when compared to PBS and passive scattering techniques, since it combines the advantages of both and can reduce the inherent artefacts and provide a homogeneous dose delivery to moving targets. This is especially important for tumors with a lot of associated motion (e.g., lung cancer) where the “interplay effects” between the tumor motion and the scanned ion beam leads to an inhomogeneous dose distribution. When using techniques like this, the short time of irradiation can make it reliable to apply respiratory techniques, such as breath-hold techniques, where the patient holds their respiration, always with the same air intake, during the irradiation period.

The range compensator is formed by many pyramid-shape base structures with specific lateral-dependent height. As shown in Figure 31 and Figure 32, the form of the range compensator and its specific amount of homogeneous material corresponds to the distal shape of the target; and the final shape of the filter corresponds to the proximal contour of the tumor, due to the arrangement of pins with different heights. What we mean by this is the height of each spike will influence the proximal conformation to the irradiated volume, and the base of the hedgehog will

influence the distal conformation to the irradiated volume. Those effects can be seen in Figure 31, represented with red and green lines, respectively.

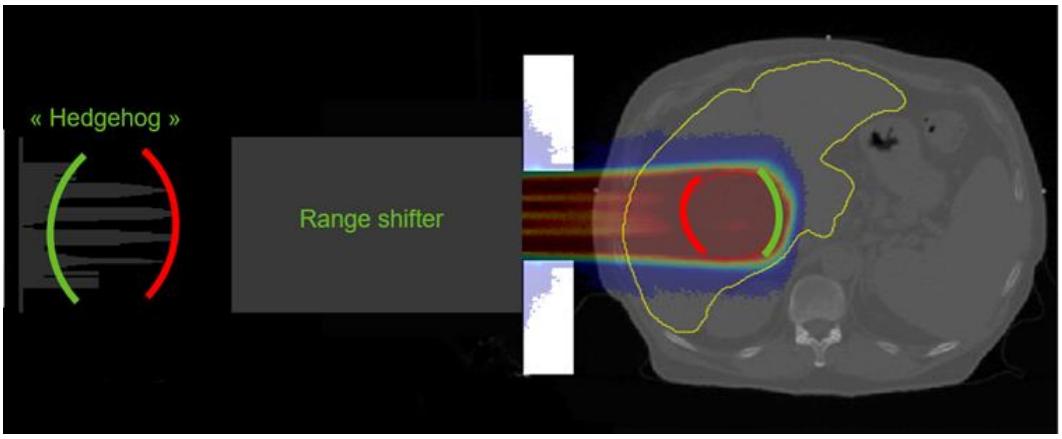

Figure 31 *Design of 3D ridge filter, also called "hedgehog", and his shape-influence on dose deposition on the tumor.* (50)

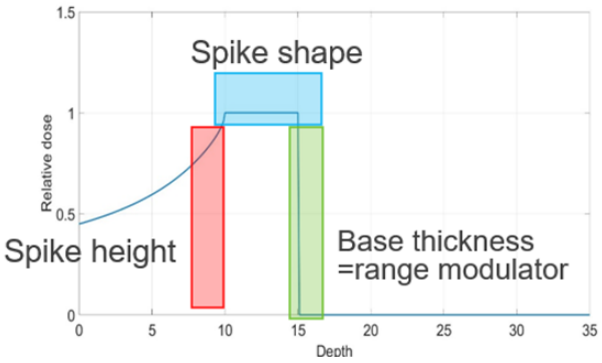

Figure 32 *Influence of the 3D ridge filter in the SOBP longitudinal profile.* (50)

The utilization of a modulator is important to blur the laterally induced fluence inhomogeneities that are characteristics of the modulators with fine and periodic structures. This effect is thought to be due to multiple scattering effects in the alternating thickness of the CEF. (64,65)

The increasing interest in FLASH techniques caused manufacturers to investigate a way to increase the accelerator intensity, improve dose delivery and monitoring systems. When considering conventional PBS techniques, the time necessary to change the primary beam energy can lead to relatively long irradiation time and, when considering conventional passive scattering techniques, their low efficiency results in a loss of particles and reduced intensity. Pondering these facts, a mono-energetic beam irradiation with a 3D ridge filter and a laterally scanned beam could be the answer to proton FLASH irradiation requisites. (60)

Figure 33 shows photographs of the latest CEF structures being tested at IBA, for clinical use.

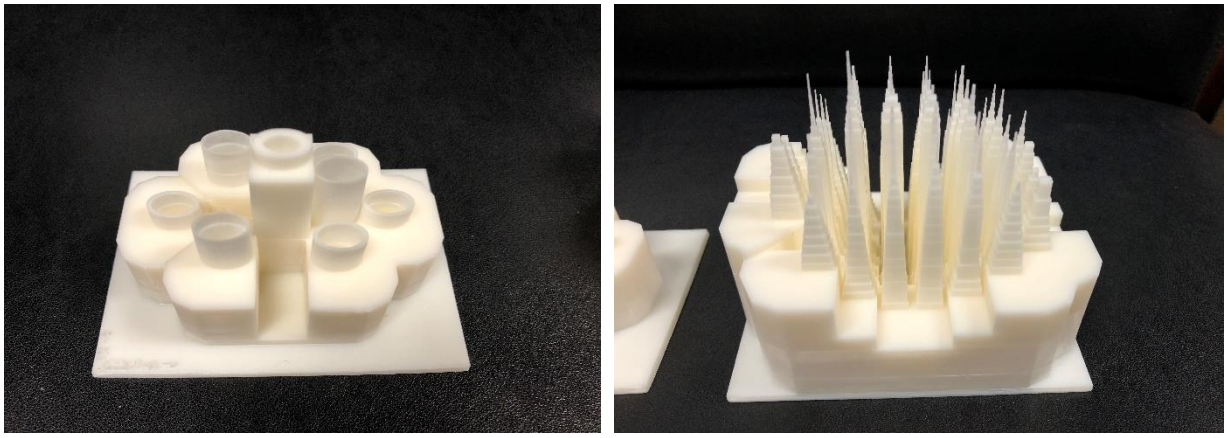

Figure 33 Photography of the latest versions of CEF under tests, at IBA.

One of the aims of this thesis is to study the feasibility and robustness of a CEF structure to different errors, such as manufacturing or beam placing, and investigate their impact on the dose distributions.

The CEF shape and sizing was done by IBA and the final geometry, in a numerical format, was sent to perform the simulation tests. The first step was to take the dimensions of each tower and create an MCNPX INP file, along with the rest of the test geometry (see chapter 9). As described before, the CEF structure is obtained from specific PBS treatment plans and the process of feature extraction was improved as this work was being done. Along with this, the final format of the towers was not decided during the elaboration of this thesis, and it was also a discussion factor. The geometries studied were rectangular and hexagonal towers, since these geometries allow covering the whole base of the hedgehog in a contiguous way.

8.3.1. Hexagonal CEF

The first geometry tested was a hexagon tower, as shown in Figure 34. The whole structure had a height of 15.3 cm (Z-axis dimension), and the bigger base has dimensions of 2.5 cm (X-axis) and 2.9 cm (Y-axis). The beam moves along the Z-axis, from the biggest hexagon to the smaller one, represented with an arrow in the figure.

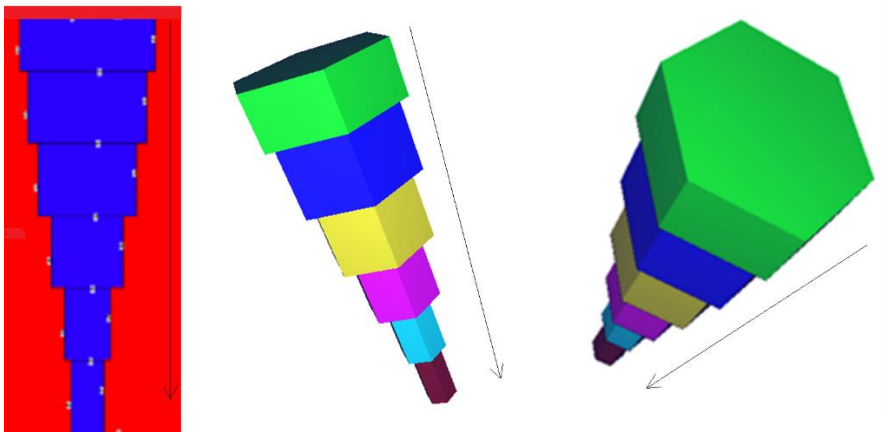

Figure 34 Representation of the hexagonal tower CEF. The image on the left was obtained with the visualization tool from MCNP. The blue geometry represents the CEF, and the red represents air. The image on the center and right was obtained with a program to plot 3D geometries, based on MCNP file code. The arrow in the images represent the proton beam direction

8.3.2. Inverted hexagonal CEF

The second geometry tested was an inverted hexagonal tower, shown in Figure 35. This one is called "inverted" since the main structure was a hexagon where the volume of a hexagon tower was subtracted from the inside. The structure had a height of 2.89 cm (Z-axis direction), and the base had dimensions of 0.69 cm in X-axis and 0.8 cm in Y-axis. The direction of the beam was the Z-axis, from the biggest aperture to the covered base of the hexagon, represented with an arrow in the figure.

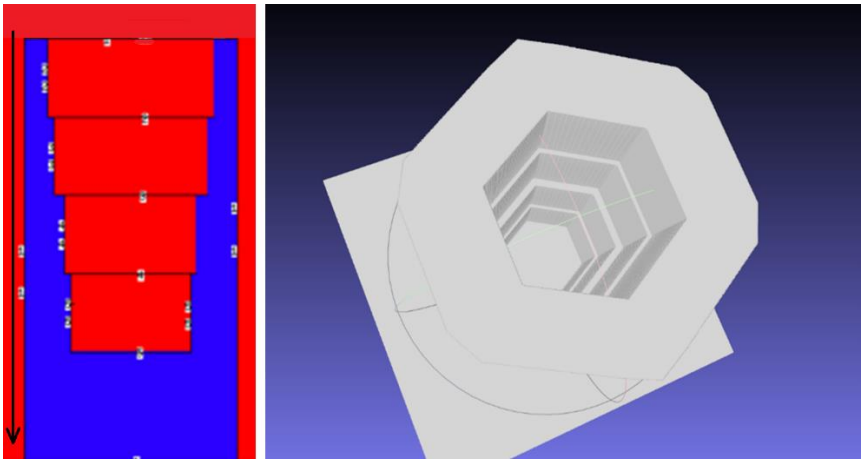

Figure 35 Representation of the inverted hexagonal tower. The image on the left is the 2D representation given by MCNP. The blue structure represents the CEF and the red one represent air. The image on the right is illustrative for this geometry, given by Dr. Lucian Hotoiu since the graphical tools of the program don't allow to show this structure in a 3D perspective.

8.3.3. Inverted rectangular CEF

The third geometry was an inverted rectangular tower, as shown in Figure 36. This structure was constructed using the same principle of the precedent. It's a parallelepiped, where the volume of a rectangular tower structure was subtracted from the inside. This tower has a height of 6.1 cm (Z-axis direction), and the base had 1.48 cm in X-axis direction and 1.48 cm in Y-axis direction. The direction of the beam was the Z-axis, from the aperture to the covered base of the inverted rectangular tower, represented with an arrow in the figure.

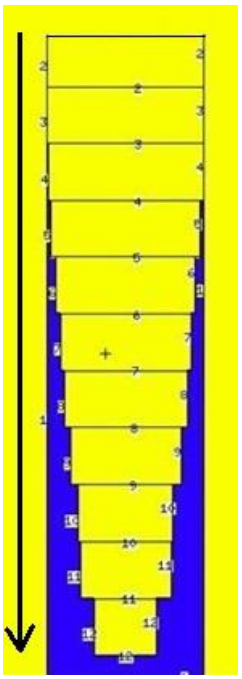

Figure 36 Representation of the inverted rectangular tower. The 2D image was obtained from graphical tools of MCNP. The blue geometry represents the CEF, and the yellow represents air.

The objective was to produce a SOBP from the irradiation of a single CEF. To observe this, each structure was simulated respecting the beam characteristics discussed above (δ_x and δ_y sizing, with sufficient beam aperture to cover the entire entry base of the structure). This simulation was performed with the assembly presented at chapter 9. This is composed by the inverted rectangular CEF with 6.1 cm, a PMMA range shifter with 12.9 cm, a lead collimator with a central aperture of 4.09 cm and a water phantom with 40 cm. The deposited dose results presented were obtained in the water phantom. The voxel size was $2 \times 2 \times 0.2 = 0.8\ cm^3$, meaning that the calculation mesh in MCNPX divided the volume of the water tank in rectangles with these dimensions and present the results of deposited energy in each.

In Figure 37 it is possible to observe that the structure that comes closer to the objective of producing a flat SOBP was the inverted rectangular tower. From this figure, we see that the inclusion, on the beam path, of a roughly 6 cm of CEF material shifts the position of the Bragg

peak by 15 cm. At this moment, more efforts are being done to obtain a plane SOBP through the irradiation of each CEF.

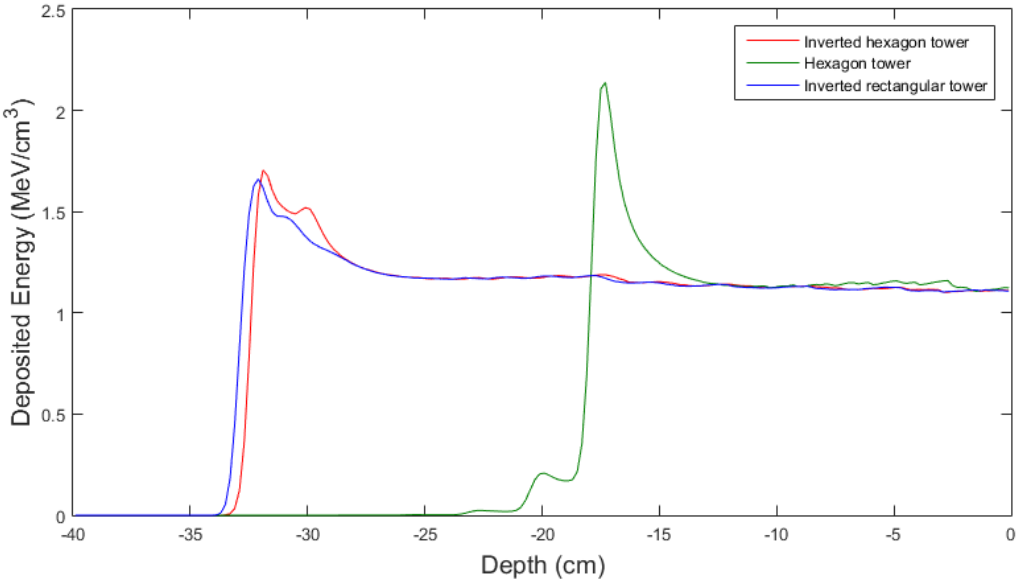

Figure 37 Longitudinal profile of deposited energy, in respect to the depth, by each CEF structure presented. The results were obtained with 1×10^6 *particles simulated.*

In terms of the longitudinal profiles, the Bragg peak created by the structure "inverted rectangular tower" is shown in Figure 38, as a representation of depth (Z-axis) per X-axis. By analyzing these plots, it's possible to observe that the SOBP happens between -35<Z<-34 cm, and -0.5<X< 0.5 cm. This area is of major importance for the robustness studies that will be performed once it will be evaluated the impact of different errors in the SOBP region.

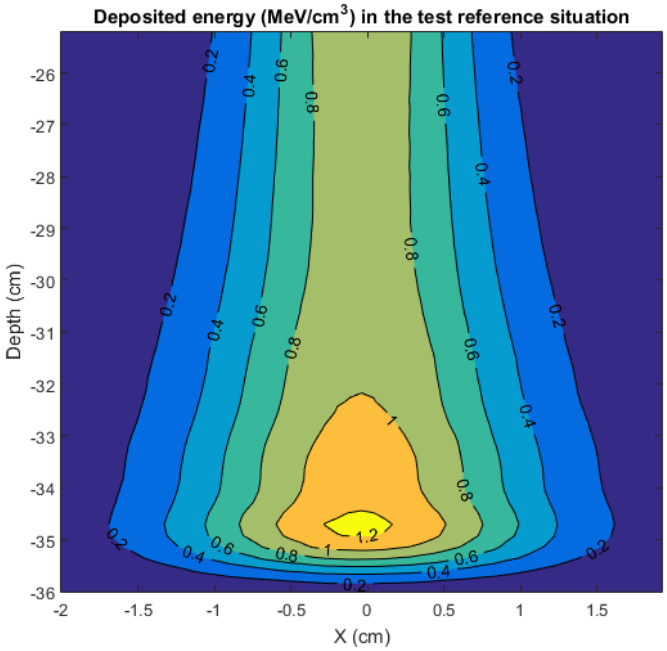

Figure 38 *Deposited energy (MeV/cm³) plots obtained with the "inverted rectangular tower" geometry. The figure is a contour plot with isolines that connect points with the same deposited energy.*

8.4. Contour plots of the percentage of deviations

The analysis of many of the results shown in the next chapter was made in MATLAB by creating contour plots of the differences between a given reference situation and several simulated situations. The percentage of difference is given by the following expression:

$$Difference\ (\%) = \frac{Test\ deposited\ energy\ - Reference\ deposited\ energy}{Reference\ deposited\ energy} \times 100 \qquad (8.1)$$

The contour function on MATLAB allows to display a plot with isodoses in a matrix. This function provides a 2D view in which all points that have the same response are connected and produce contour lines of constant responses. This plot displays two independent variables on the X and Y-axes and contour lines that connect points that have the same response value (dependent variable). (66)

9. Results and discussion

The objective of this chapter is to understand the impact of different uncertainties on the deposited energy distribution. For this, different errors were induced, regarding beam translation, beam angulation, material density changes, beam width estimation and CEF lateral dimensions. All these induced errors were made in relation to a standard geometry, described next, and the results of deposited energy were compared to those.

The studies were performed in relation to the geometry assembly presented in Figure 39. The proton beam was set at X,Y,Z=(0, 0, 6.1) cm and moves across the Z-axis direction, in the negative sense. The beam had energy of 230 MeV and an elliptical shape, with gaussian distribution, with $\sigma_x = 0.2386\ cm$ and $\sigma_y = 0.3698\ cm$. The lateral dimensions of the beam were set to cover the whole base of the CEF.

The structure A represents the inverted rectangular CEF (detailed description in chapter 8.3). This structure has 6.1 cm of depth (Z-axis), 1.48 cm in X-axis direction and 1.48 cm in Y-axis direction. The material chosen to create this structure was water.

The following structure in the beam path is a range shifter, represented in the figure by B, composed by polymethyl methacrylate (PMMA). This structure had dimensions of 12.29 cm in depth (Z-axis) and 12 cm in X and Y-axis direction.

The structure C represents a square collimator with dimensions of 4.09 cm of depth (Z-axis). The structure had 12 cm on X and Y-axis direction, with a square central aperture of 4.09 cm in X and Y-axis direction. Usually, the material used for this structure is brass but, in this work, the material chosen was lead. The material inside the aperture was set to air.

The final structure in the beam path, represented as D, is a 40 cm long water phantom, with a square section identical to that of B and C. All the results for energy deposition shown in the following section were calculated in this structure because, in PTR, this material mimics the properties of human tissues in terms of energy loss, MCS and nuclear interactions. (7)

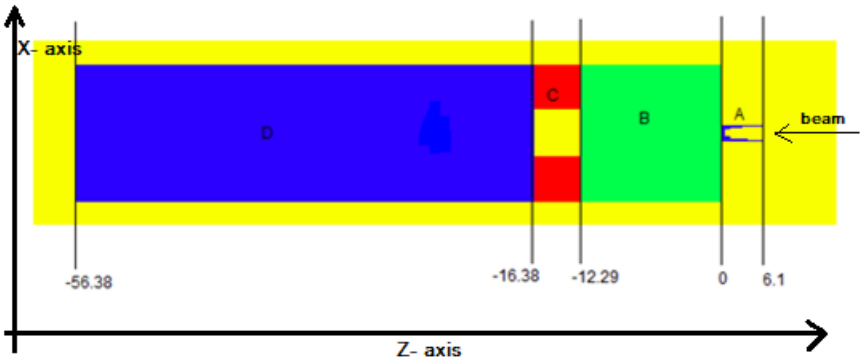

Figure 39 *Schematic representation of the simulated geometry assembly. A) CEF; B) range shifter; C) collimator with central aperture; D) water phantom.*

The material that surrounds the complete structure is air and is represented by yellow in Figure 39. The material density and the composition expressed in percentage of number of atoms of all materials used is presented in Table 8.

Table 8 *Description of materials used in the simulated geometry assembly.*

Material	Density (g/cm^3)	Number of atoms (%)
Water	0.997	H (66.67%) + O (33.33%)
PMMA	1.15	C (33.33%) + O (13.33%) + H (53.33%)
Lead	11.34	Pb (100%)
Air	0.001225	N (70.08%) + O (20.92%) + Ar (9%)

9.1. Uncertainty in beam translation

To quantify the deposited energy differences due to an alteration in the beam position in the simulated assembly, a beam shifting in the X-axis direction was made. In the reference simulation, the beam moves along the Z-axis, in the negative sense, and is generated at (X, Y) = (0, 0). The simulated scenarios contemplated 4 magnitudes of beam translation in the X-axis, relative to the beam origin: displacement of 0.02 cm, 0.05 cm, 0.07 cm, and 0.1 cm. In MCNPX, these changes were introduced in the definition of the source positioning, in the SDEF card.

In Table 9 the depth of R_{100} and the maximum deposited energy are presented. It is possible to observe that the depth of R_{100} only changed for a beam displacement of 0.1 cm by 2.31%. In contrast, the maximum deposited energy varied from the reference situation in all the simulated scenarios. Along with the augmentation of the beam shifting, a decrease in the maximum deposited energy in the water phantom is verified. Due to the high number of particles

simulated, the maximum relative error associated to the deposited energy and range was 0.07%. Notice that the percentual differences observed for the maximum deposited energies are well above the error bar of the simulations.

Table 9 Comparison of the results from R_{100} (cm) and maximum deposited energy (MeV/cm^3) between the reference and the beam shifting scenarios. The maximum relative error associated to the deposited energy was 0.07%

	Reference	0.02 cm	0.05 cm	0.07 cm	0.1 cm
R_{100} (cm)	-34.7000	-34.7000	-34.7000	-34.7000	-34.5000
Difference relative to the reference (%)		0	0	0	-2.3055
Maximum deposited energy (MeV/cm^3)	1.5420	1.5400	1.5302	1.5192	1.4763
Difference relative to the reference (%)		-0.1297	-0.7652	-1.4786	-4.2607

The Figure 40 shows a representation of the Bragg peak in each scenario. The calculation grid was $2 \times 2 \times 0.2\ cm = 0.8\ cm^3$.

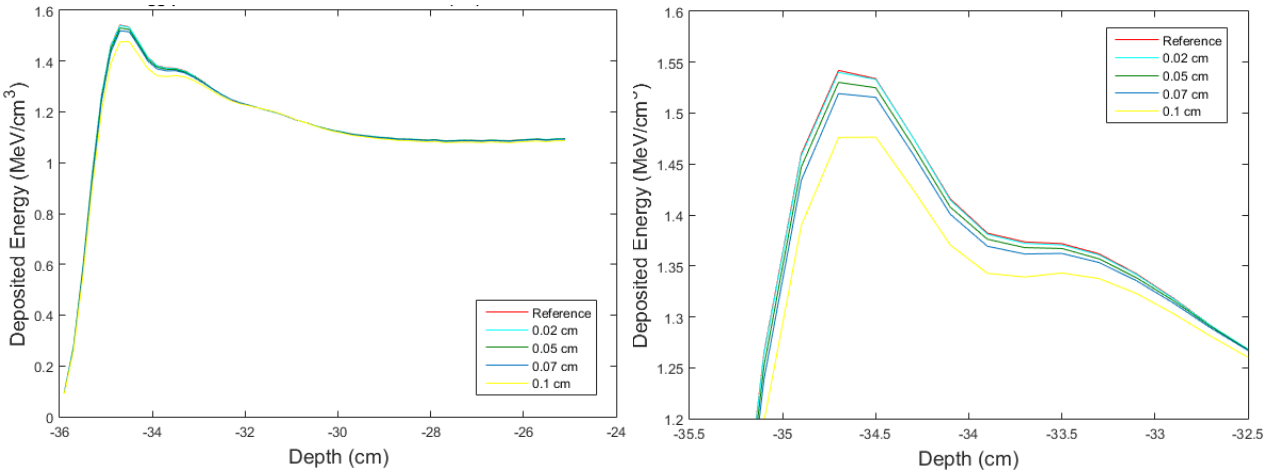

Figure 40 Bragg peak representation resulting from the different test scenarios. The image on the right shows an approximation of the Bragg peak region.

In Table 10 we present the averaged proton deposited energy (MeV/g) in each structure of the simulated assembly with the respective relative error, individually.

It is possible to observe that the averaged proton deposited energy increases in the CEF, as we augment the beam shifting. When the beam is shifted, the maximum of the fluence is shifted from the hole in the center of the chimney to the edge of the chimney. This leads to more energy being deposited in the wall of the chimney and less being deposited in the water phantom, as also shown in Table 10. This is due to the effect of moving the gaussian beam axis from the center of

the structure. Because it is an inversed CEF structure, in the reference scenario, the beam axis is centered in the CEF area with less absorbing material thickness. After moving the beam, and consequently moving the center of the gaussian, this part of the beam will encounter areas with more absorbing material thickness, and this leads to an augmentation on the deposited energy in the structure.

Besides the increase of deposited dose being more pronounced in the CEF, a slight augmentation in the range shifter and in the collimator is also observed. Due to the high number of particles used for the simulation, the maximum relative error associated to the deposited dose was 0.24%.

Table 10 Proton deposited dose averaged (MeV/g) in each structure that compose the simulated geometry, in the reference situation. The remaining values are the percentual difference (%) between the proton deposited dose averaged results in the reference simulation and the simulation results for each beam sift (0.02 cm, 0.05 cm, 0.07 cm, and 0.1 cm), in each structure.

	Reference (MeV/g)	0.02 cm (%)	0.05 cm (%)	0.07 cm (%)	0.1 cm (%)
CEF	0.8063	0.2326	1.5117	2.9645	6.0954
Range shifter	3.4071×10^{-2}	0.0845	0.0100	0.0252	0.0610
Collimator	1.00476×10^{-3}	0.0100	0.0965	0.1413	0.2488
Water phantom	2.24050×10^{-2}	-0.001	-0.0549	-0.1129	-0.2361

In order to confirm the beam shifting on X-axis, we created transversal plots of the deposited energy at different depths. Figure 41 and Figure 42 show that the decrease of energy observed in the water tank is not a numerical error. When the beam changes its position, the whole Gaussian remains inside the measurement window and, therefore, the results are not due to numerical errors. Meaning, since the grid used for the X-axis was divided in 0.1 cm segments the variation of position of deposited energy is real and not an artifact of the simulation.

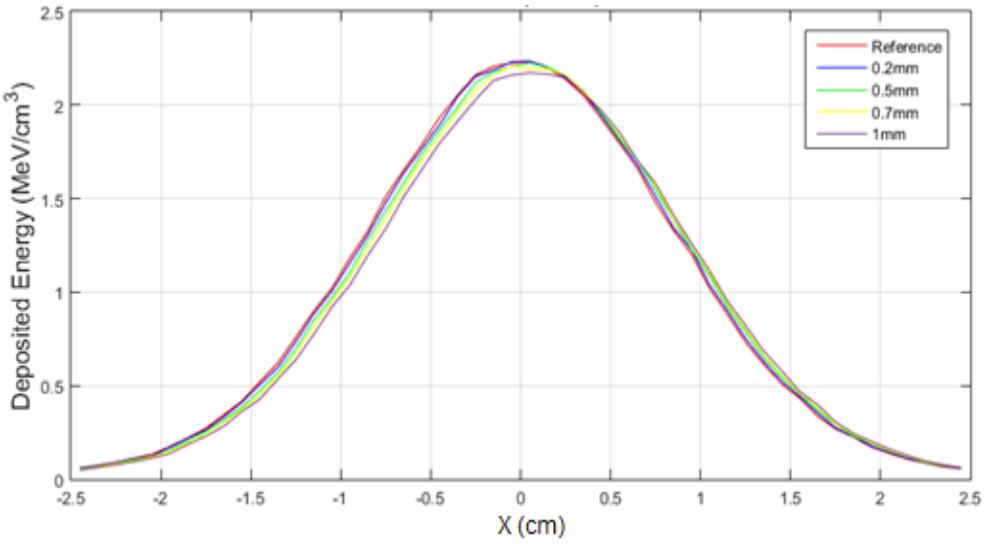

Figure 41 Lateral dispersion at the depth of Z= -34.6 cm, the SOBP region. The calculation grid volume had a value of $0.1 \times 1 \times 0.1\ cm\ = 0.01\ cm^3$.

The value of X-axis where the deposited energy is 50% of the maximum deposited energy (E_{max}) in the transversal plot, is called $X_{50\%Dmax}$. Because the transversal plot follows a gaussian distribution, we will have two points in the X-axis where the deposited energy has 50% the value of the maximum deposited energy in the graph. The point in X-axis where the maximum deposited energy is registered, is called X_{Emax}.

Table 11 Values of maximum energy (E_{max}), X-axis value where the maximum deposited energy is deposited (X_{Emax}) and values of X-axis where 50% of the maximum deposited energy is registered ($X_{50\%Emax}$), in transversal plot, for a depth of Z= -34.6 cm. The presented values allow to establish a comparison between the reference situation and the situations where uncertainties in the beam position were made (0.02 cm, 0.05 cm, 0.07 cm and 0.1 cm)

	Reference	0.02 cm	0.05 cm	0.07 cm	0.1 cm
$X_{50\%Emax}$ (cm)	-0.95 / 0.95	-0.95/0.95	-0.85/0.95	-0.85/0.95	-0.85/1.05
E_{max} (MeV/cm^3)	2.2310	2.2341	2.2252	2.2108	2.1714
X_{Emax} (cm)	0.05	0.05	0.05	0.05	0.05

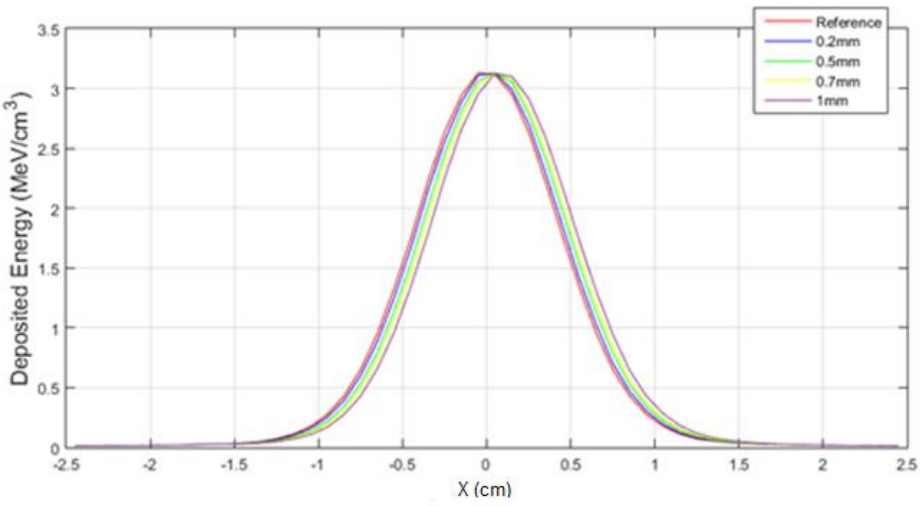

Figure 42 Lateral dispersion at Z= -20.7 cm, at water phantom entry. The calculation grid volume had a value of $0.1 \times 1 \times 0.1\ cm\ = 0.01\ cm^3$.

Table 12 Values of maximum energy (E_{max}), X-axis value where the maximum deposited energy is deposited (X_{Emax}) and values of X-axis where 50% of the maximum deposited energy is registered ($X_{50\%Emax}$), in transversal plot, for a depth of Z= -20.7 cm. The presented values allow to establish a comparison between the reference situation and the situations where uncertainties in the beam position were made (0.02 cm, 0.05 cm, 0.07 cm and 0.1 cm).

	Reference	0.02cm	0.05cm	0.07cm	0.1cm
$X_{50\%\ Emax}$ (cm)	-0.45 / 0.45	-0.45 / 0.45	-0.35 / 0.55	-0.35 / 0.55	-0.35 / 0.55
E_{max} (MeV/cm^3)	3.1312	3.1293	3.1274	3.1337	3.1269
X_{Emax} (cm)	0.05	0.05	0.05	0.05	0.05

By the analysis of Figure 41, Figure 42, Table 11 and Table 12, is possible to conclude that the lateral amplitude of the distribution is bigger at bigger depths. In this case, is bigger at the SOBP region than at the entrance of the water phantom. It is also possible to observe that this amplitude between $X_{50\%\ Emax}$ values didn't change at the same depth. When the beam position is shifted, this $X_{50\%\ Emax}$ values also change their position, but not the interval between them. In other words, as we see from Figure 42, the "gaussian" curves are shifted to the right, but their width remains the same.

Another effect that is possible identify is that, for shiftings larger than 0.07 cm, the shape of the SOBP changes. These changes can be visible in the Figure 43 where we compare the deposited energy distribution in the reference situation and with the beam position shifted by 0.1 cm.

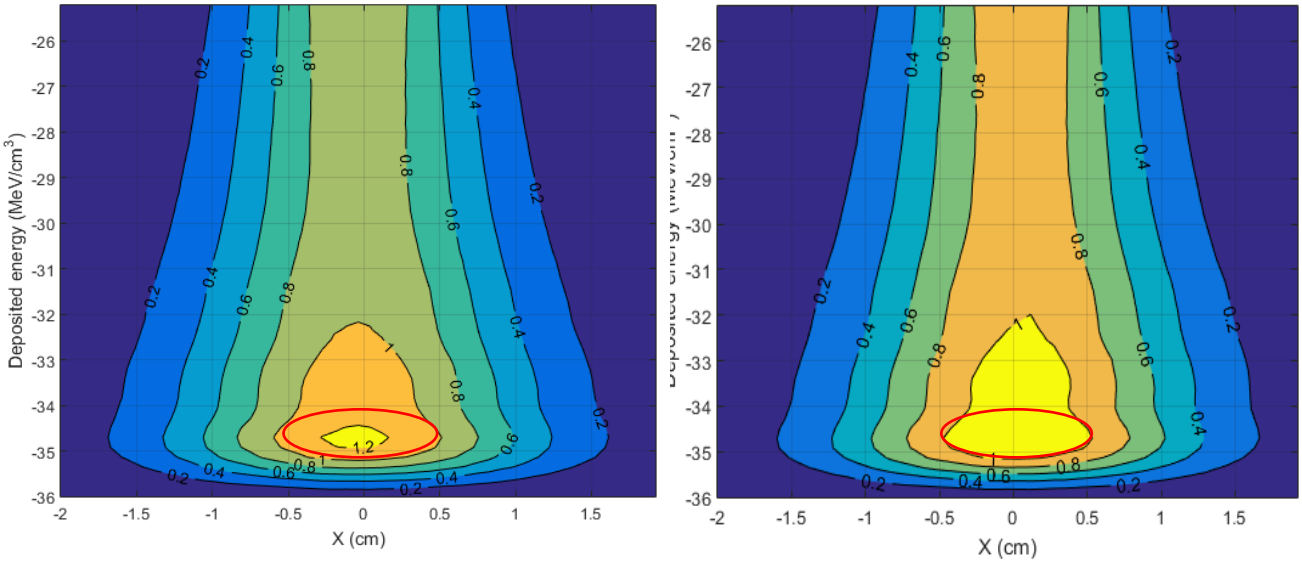

Figure 43 *The figure on the left represents the deposited energy in the reference situation. The figure on the right represents the deposited energy in the situation where the beam has been shifted by 0.1 cm. The red ellipse represents the SOBP area in the reference situation.*

Figure 44 shows the contour plot of deposited energy difference between the reference situation and each shifting of the position of the beam. Remember that the reference situation includes a beam of 230 MeV hitting the assembly represented in Figure 39, at position (0,0,0), along the Z-axis, as described in section 9. In the contour plot, each line joins points having equal percentage of difference to the reference situation.

The first effect that is possible to see is that the deposited energy map is shifting to the right – in fact, we observe negative percentages of difference in the left of the plot and positive ones in the right of the plot. This is explained by the fact that all the beam shiftings were made on the positive sense of the X-axis. For the fourth plot of Figure 44, which corresponds to the largest beam deviation considered (0.1 cm), notice that the percentage of deviation in deposited energy can reach 43% in upper corner of the plot.

Along with his, is also possible to observe in Figure 44 that the contour lines becomes curved in the SOBP area, when the shift is larger than 0.07 cm. This indicates that the shape of the SOBP has changed. This observation can be used to define the limit above which it is not acceptable to have a shift of the beam.

It is also possible to see that, in the SOBP region, a shift of 0.02 cm induces maximal differences of deposited energy of about 1%, a shift of 0.05 cm induces maximal differences of deposited energy of about 3%, a shift of 0.07 cm induces maximal differences of deposited energy of about 5% and a shift of 0.1 cm induces maximal differences of deposited energy of about 8%.

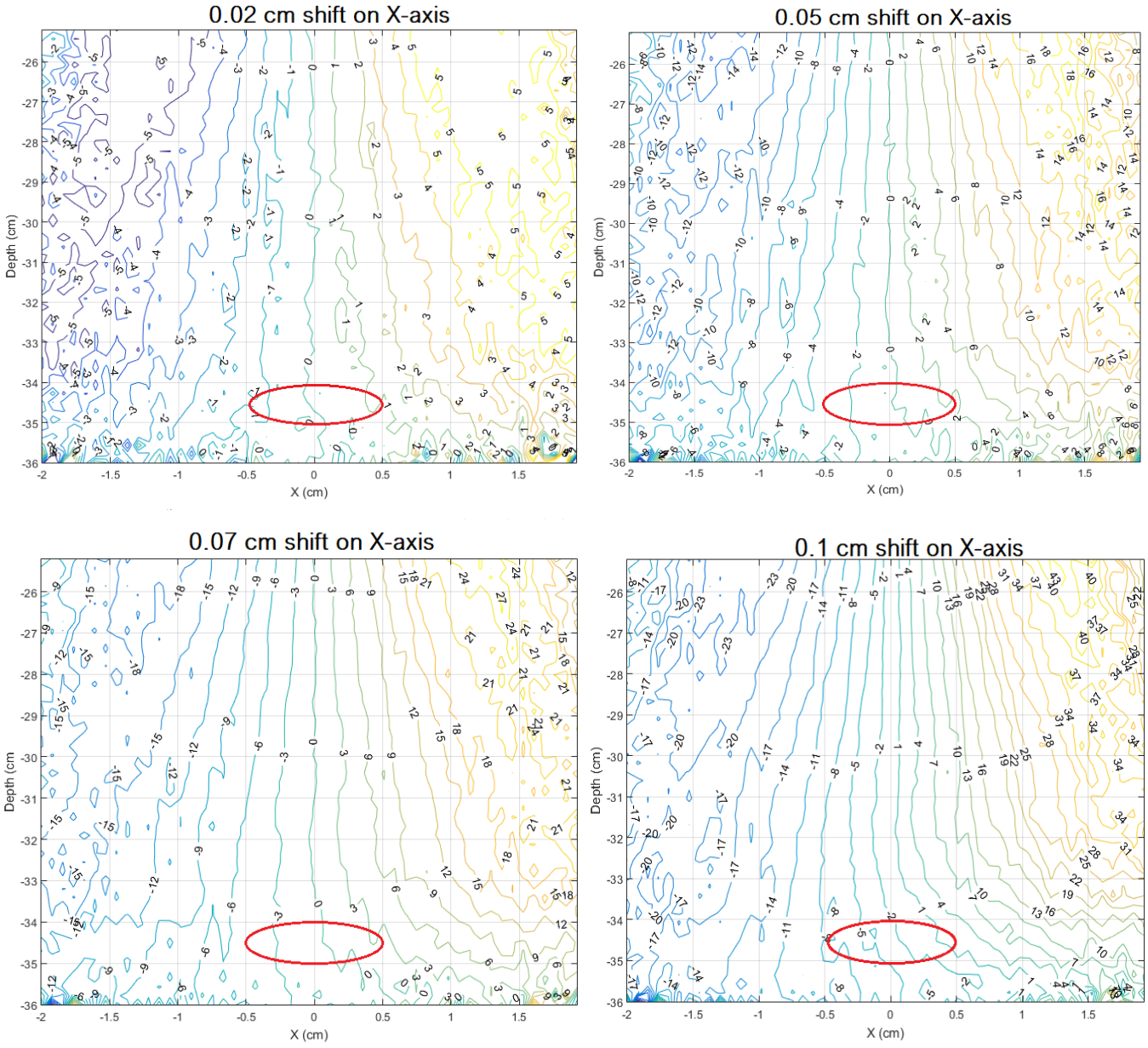

Figure 44 Contour plots of deposited energy (MeV/cm3) difference between the reference geometry and the beam shifting on X-axis. The results are shown in percentage The red ellipse in the graphs represents the SOBP region in the reference situation.

9.2. Uncertainty in beam angulation

This simulation aimed at quantifying the differences in deposited energy from different beam angulations, comparatively to the reference simulation assembly. For this purpose, we simulated three different beam angulations, in respect to the beam path (Z-axis) represented in Figure 39: deviations of 0.2º, 0.5º and 1º.

These changes were induced in MCNPX at the definition of the SDEF card. It was assumed that the beam was in the plane YZ and, to induce an angle of this with respect to Z-axis, the vector inserted was:

$$vec = 0 \quad \sin(angle) \quad \cos(angle)$$

Thus, an angle of 0º is a beam along the Z-axis and an angle of 90º would be a beam pointing along the positive Y-axis. The small deviations we considered therefore slightly rotate the direction of the beam from the Z-axis to the Y-axis.

The results of Table 13 point out that the values of R_{100} didn't change on the water phantom. Otherwise, it is possible to verify a decrease on the maximum deposited energy when the beam angulation becomes more pronounced. This is explained by the same principal highlighted on the discussion of chapter 9.1. When the center of the gaussian beam is moved, the energy deposited at the CEF increases and reduces in the water phantom. Notice that this variation observed is well above the uncertainty that we obtained from the simulation.

Table 13 Comparison of the results from R_{100} (cm) and maximum deposited energy (MeV/cm^3) between the reference and the three beam angulation scenarios, with respect to Z-axis. Due to the high number of particles, the maximum relative error associated to the deposited energy was 0.07%

	Reference	0.2 º	0.5 º	1 º
R_{100} (cm)	-34.7000	-34.7000	-34.7000	-34.7000
Difference relative to the reference (%)		0	0	0
Maximum deposited energy (MeV/cm^3)	1.5420	1.5314	1.4703	1.2640
Difference relative to the reference (%)		-0.6874	-4.6498	-18.0285

This diminution of deposited energy can also be observed in the longitudinal profile in Figure 45. Despite that, the overall shape of the energy curve has not been altered in the longitudinal profile.

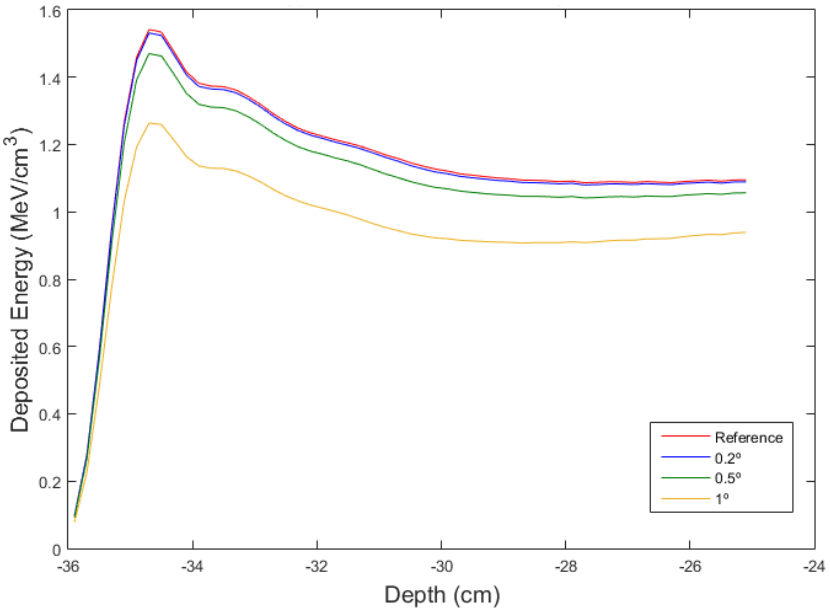

Figure 45 *Longitudinal profile of simulated SOBP curves. The results were obtained in the water phantom and are result of different beam angulations, with respect to Z-axis.*

The contour plots of the deposited energy difference presented in Figure 46 are relative to the X and Z-axis. As expected we do not observe major percentual differences, since the deposited energy distribution on Y and Z-axis is more affected by the induced beam angulations.

In Figure 46 it is possible to observe that a beam angulation of 0.2º will not lead to differences in the SOBP shape. When a beam angulation of 0.5º is induced, the deposited dose at the SOBP is changed by about 0.6%. For a beam angulation of 1º, it is visible that the deposited energy at the SOBP changed by about 5%. It is therefore possible to conclude that the acceptable limit for the beam angulation is situated between 0.5º and 1º. For this reason, it is recommended to do more simulations with beam angulations within these values.

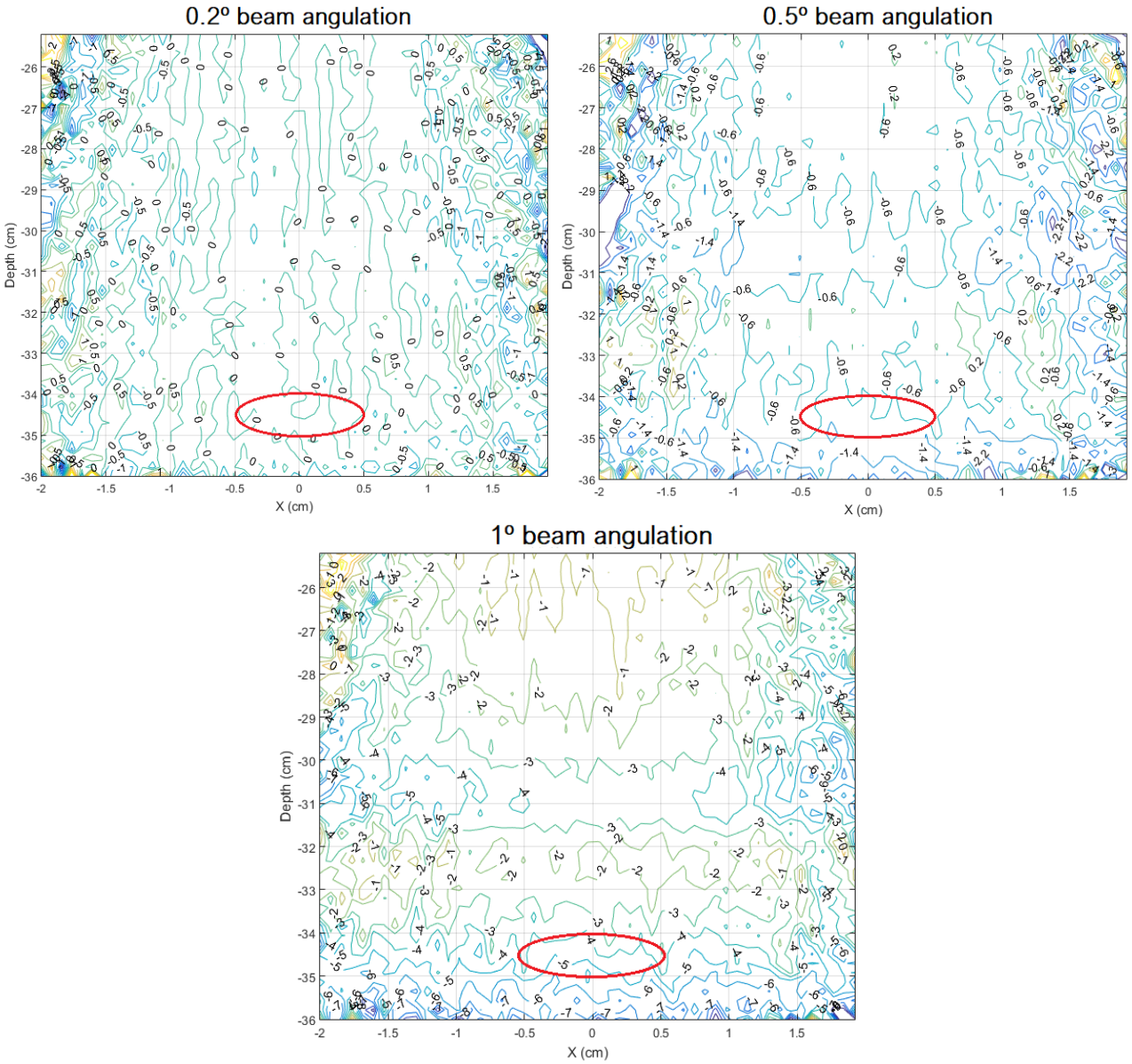

Figure 46 Contour plots of deposited energy (MeV/cm3) difference between the reference geometry between the reference structure and different degrees of beam angulation. The results are shown in percentage and the red ellipse in the graphs represents the SOBP region in the reference situation.

The Figure 47 show the contour plots of the difference, concerning the Y and Z-axis – we clearly see a shift in deposited energy towards the right of the plots, easily explained by the fact that the beam is hitting the assembly at increasing values of the Y coordinate as the angle increases.

It is possible to observe that a beam angulation of 0.5 º produces variations of 5% in the SOBP region of the reference situation and an angulation of 1 º produces variations of 40%, in the same region. Notice that, from the origin point of the beam to the SOBP region, the protons travelled around 56 cm in the reference situation. The most extreme angulation we considered

shifts the position of the SOBP in the Y-axis by 56 x tan(1º) ≈ 1 cm. In fact, we observe, in the plot corresponding to the 1º angulation, the isoline of +100% occurring very close to Y = 1 cm, thus confirming our geometrical expectations.

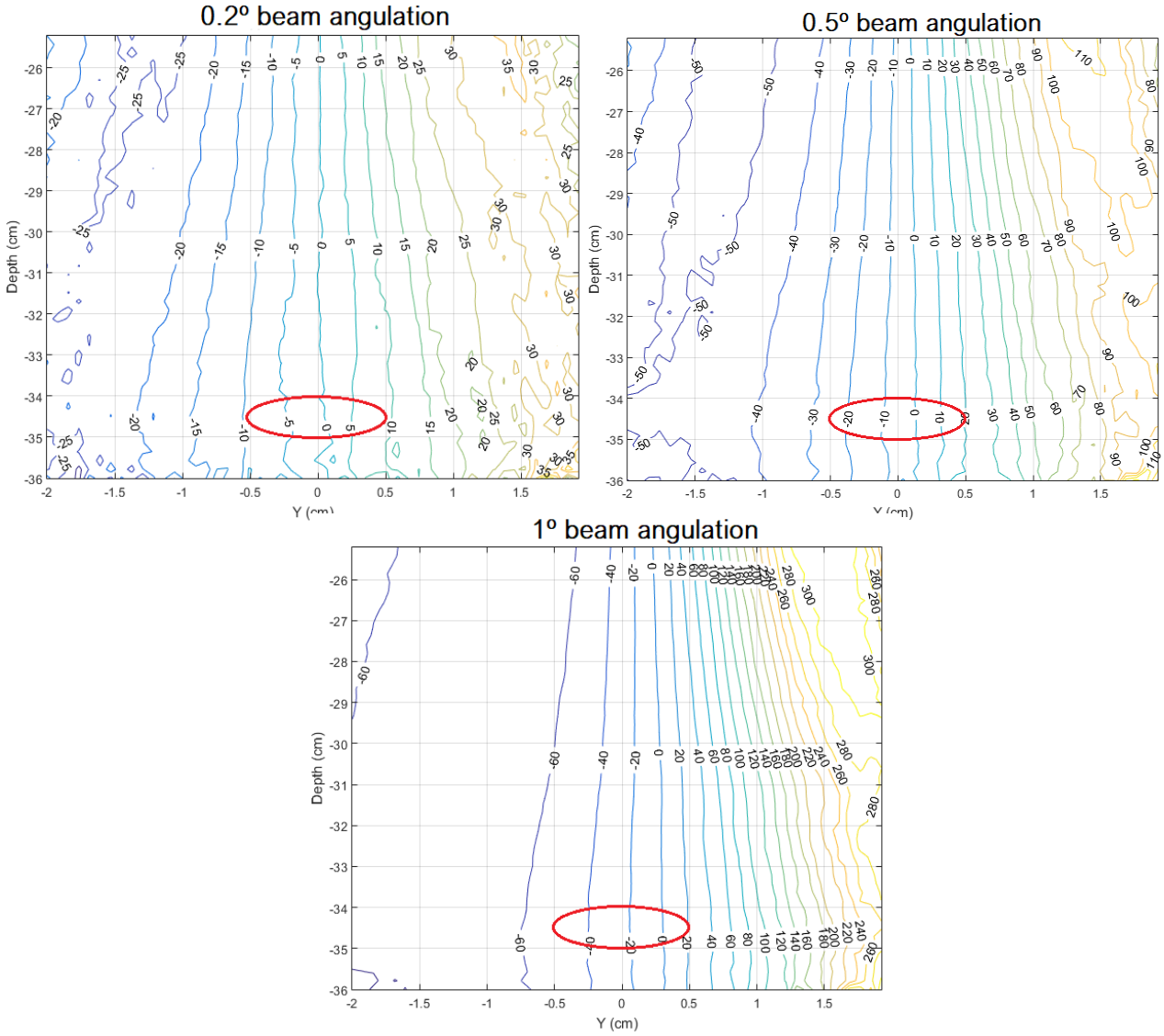

Figure 47 Contour plots of deposited energy (MeV/cm³) difference between the reference geometry between the reference structure and different degrees of beam angulation. The results are shown in percentage and the red ellipse in the graphs represents the SOBP region, in the reference situation.

The Figure 48 shows the deposited energy distribution of the reference situation beam and the deposited energy distribution produced by a beam with 1º of angulation. By comparing those graphs, it is possible to identify that the deposited energy distribution has changed to the right and, by consequence, the SOBP is no longer at the same position.

We can see from the Figure 48 that the center of the SOBP on the ref situation is located roughly at -0.1cm and the right 0.7, giving approximately a shift of 1cm.

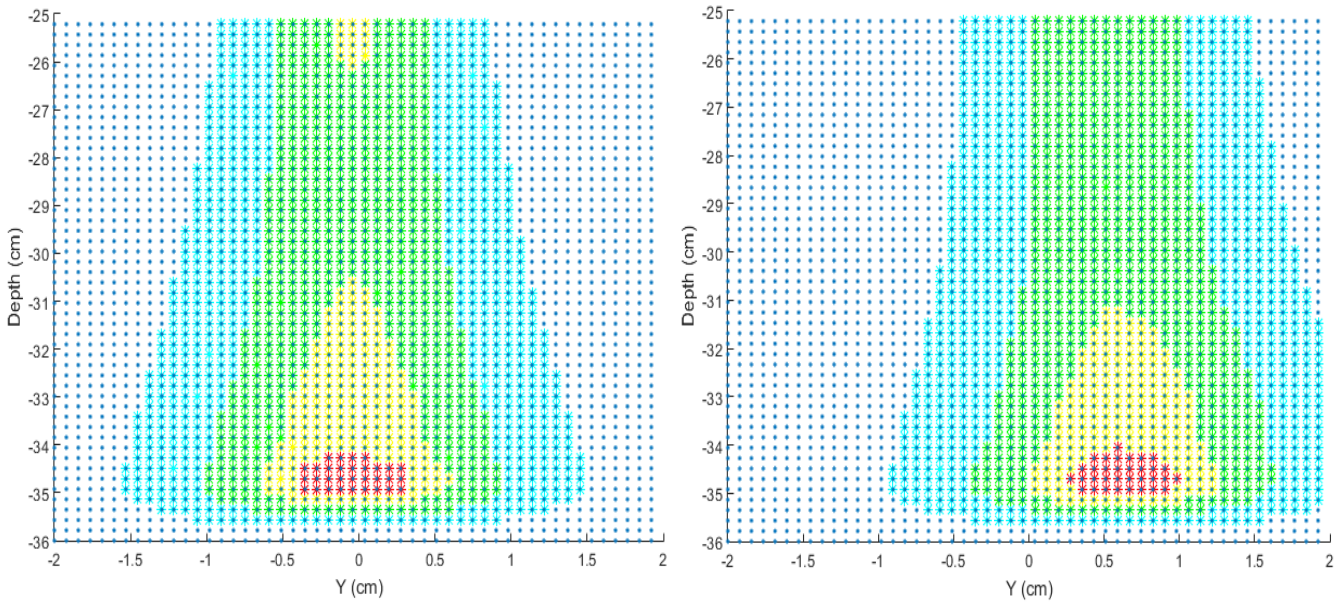

Figure 48 Comparison between deposited energy (MeV/cm^3) in the reference scenario (on the left) and beam angulation of 1º (on the right).

9.3. CEF material density change

This simulation aimed at quantifying the effect of heterogeneities in the CEF structure, on the deposited dose distribution. For this, an error of 1%, 2% and 3% in the density of the CEF material was introduced. Those percentual values are the variations of density due to the porosity presented by most 3D printer's manufacturers. In normal conditions, it's assumed the CEF is composed by water, with density of 0.997g/cm^3. For the simulation purposes, it was assumed that the material density was 0.98703 g/cm^3 (change of -1%), 1.00697 g/cm^3 (change of +1%), 0.97706 g/cm^3 (change of -2%), 1.01694 g/cm^3 (change of +2%), 0.96709 g/cm^3 (change of -3%) and 1.02691 g/cm^3 (change of +3%).

In Table 14 it is possible to observe that there is a difference in terms of deposited energy, but not in the position of the SOBP. The position of the distal fall-off depends on the Bragg peak with the largest energy. By using the design of the inverted rectangular CEF, the position of the distal fall-off will depend on the portion of the beam that went through the part of the CEF with least thickness (about 0.2 cm). It is the protons that cross the chimney wall that will suffer the largest influence of the density change. The observation of this results highlights that a variation of 3% on the CEF material is not sufficient to influence the distal fall-off.

Another observation made from Table 14 is that the bigger the value of heterogeneity, the bigger the deposited energy difference. When there is more density than the reference, the deposited energy decreases with the heterogeneity augmentation. The inverse happens when there is less density than the reference. Due to the high number of particles used in the simulation, the relative error associated to the range and maximum deposited energy is at most 0.1%.

Table 14 Summary of R_{100} and R_{80} position and energy deposited by different CEF densities, on the water phantom. The relative error associated to the range and maximum deposited energy is at most 0.1%.

	-3%	-2%	-1%	Reference	+1%	+2%	+3%
R_{100} (cm)	-34.675	-34.675	-34.665	- 34.665	-34.655	-34.645	-34.645
Difference relative to the reference (%)	-0.0289	-0.029	0		0	0.058	0.058
R_{80} (cm)	-35.125	-35.125	-35.125	-35.1150	-35.1150	-35.115	-35.105
Difference relative to the reference (%)	-0.029	-0.029	-0.029		0	0	0.029
Maximum deposited Energy (MeV/cm^3)	1.562	1.559	1.555	1.553	1.549	1.545	1.541
Difference relative to the reference (%)	-0.599	-0.393	-0.155		0.258	0.490	0.734

Figure 49 represents the longitudinal profile of the simulated SOBP curves and illustrates the results of Table 14.

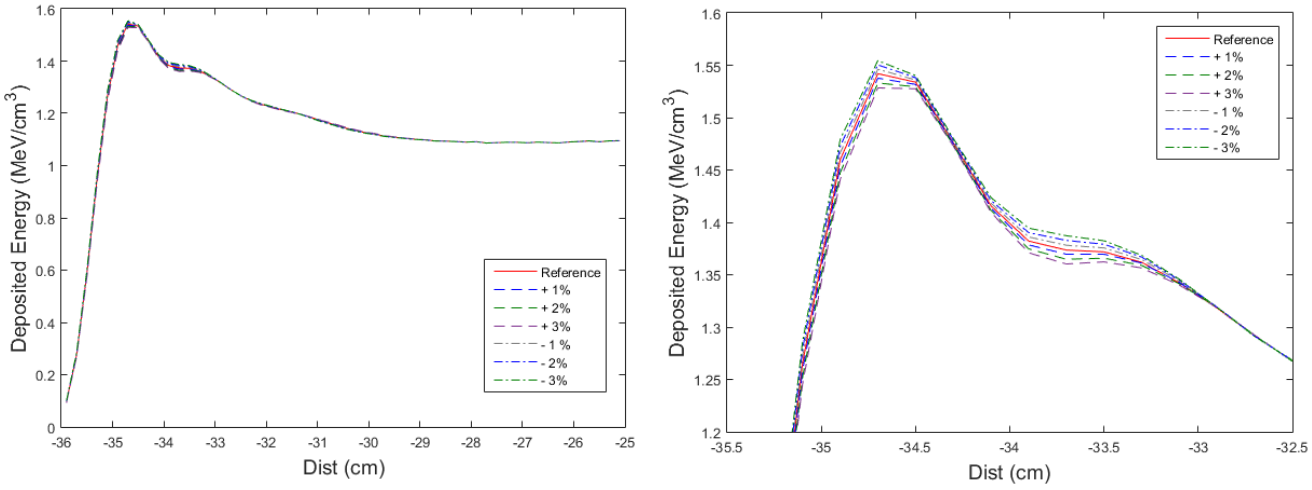

Figure 49 *Longitudinal profile of simulated SOBP curves. The results were obtained in the water phantom and are result of different density changes in the CEF material.*

Figure 50 presents the contour plots of the difference between the reference situation and the different simulated density changes in the CEF material. It is possible to observe that the percentual differences of deposited energy in the SOBP region are 0.2% and 0.3% for the CEF density change of -1% and 1%, respectively. For the case of -2% and 2% changes in the CEF density, the percentual difference of deposited energy is 0.5%. For the case of -3% and 3% changes in the CEF density, the percentual difference of deposited energy is 1%.

Another conclusion that is possible to make by the interpretation of the Figure 50 is that when the CEF has more density than the reference situation, the deposited energy is superior in the overall graph. The inverse happens when the CEF has less density than in the reference situation and the deposited energy in the overall graph is inferior. In other words, if the CEF density is superior/inferior to the reference situation, there is a greater/smaller energy deposition in the CEF, and therefore a smaller/greater value of energy at the SOBP region.

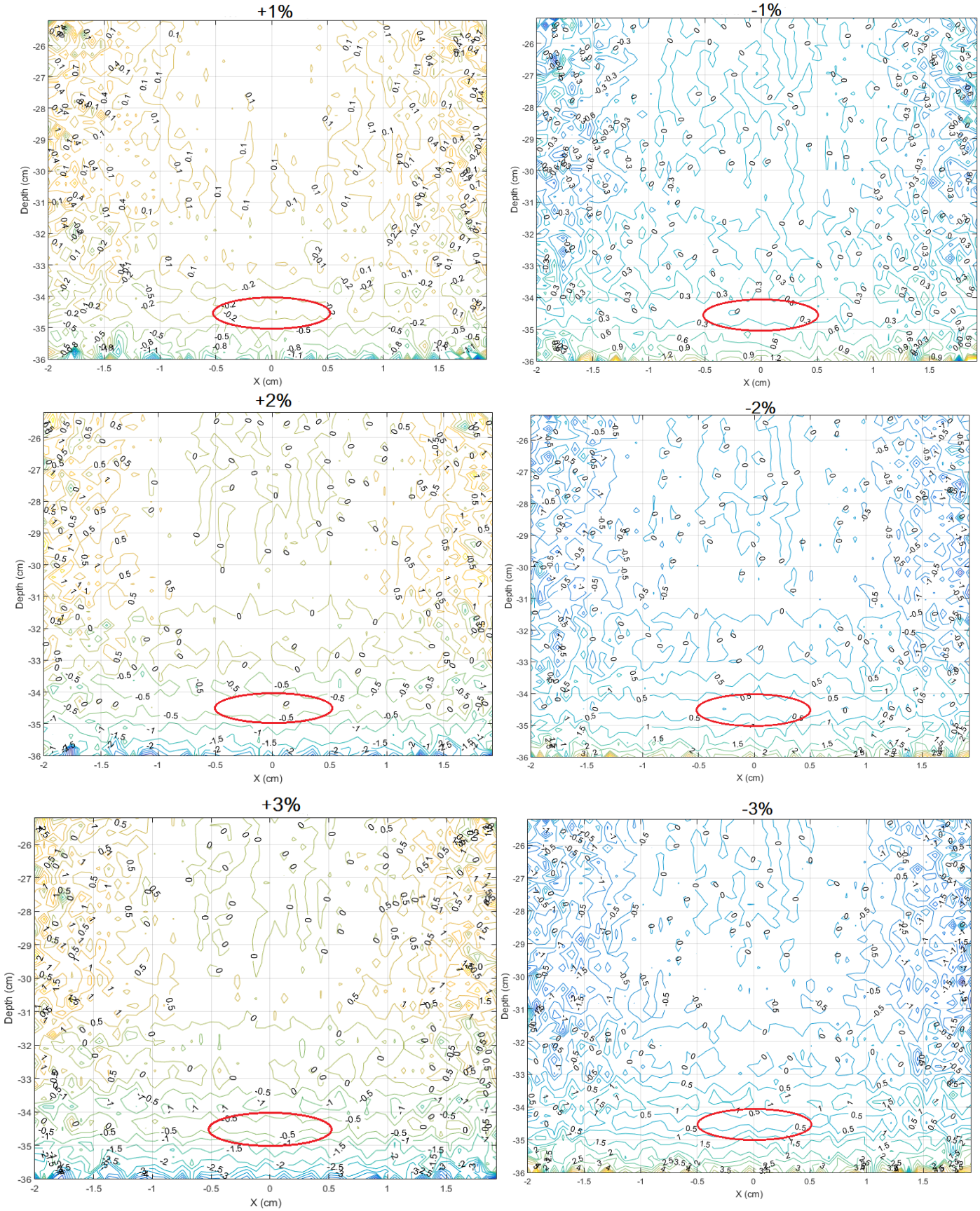

Figure 50 *Contour plots of deposited energy (MeV/cm^3) difference between the reference geometry structure and different CEF material density changes. The results are shown in percentage and the red ellipse in the graphs represents the SOBP region in the reference situation.*

9.4. Beam dimensions mis-estimation

This simulation aimed at verifying the impact of an error in beam transverse dimensions, i.e. the standard deviation σ of the gaussian distribution which describes the proton spread in the plane transverse to the beam direction. The beam sigma reference values for the simulations were:

$$\sigma_x = 0.2386\ cm$$

$$\sigma_y = 0.3698\ cm$$

The full width half maximum (FWHM) of the Gaussian, in either the X or Y direction, is calculated as follows:

$$f_x = (8\ ln2)^{1/2}\sigma_x = 2.35482 \times \sigma_x = 2.35482 \times 0.2386 = 0.5619\ cm$$

$$f_y = (8\ ln2)^{1/2}\sigma_y = 2.35482 \times \sigma_y = 2.35482 \times 0.3698 = 0.8708\ cm$$

To study the threshold of acceptance in the case of having an error in sigma estimation, 3 magnitudes of errors were simulated. The errors induced were ±0.01 cm, ±0.02 cm and ±0.03 cm for the σ_x values of the proton beam. The values of σ_y were left unchanged. The calculation of the FWHM in each case is summarized in Table 15. Those changes were introduced in the SDEF card, on MCNPX, when defining the beam.

Table 15 Magnitude of errors induced and calculation of FWHM in each case.

Error induced on σ_x	Resultant value of σ_x after error induction (cm)	FWHM (f_x) (cm)
±0.01 cm	0.2286	0.5416
	0.2486	0.5887
±0.02 cm	0.2186	0.5181
	0.2586	0.6123
±0.03 cm	0.2086	0.4945
	0.2686	0.6358

In Figure 51 and Table 16 it is possible to observe that changes in σ_x values have an impact in the deposited energy, but not in the beam range. The deposited energy decreases when using bigger σ_x values, and the inverse happens for smaller σ_x values. This phenomenon happens for the same reason explained in chapter 9.3.. In other words, a wider/thinner beam causes larger/smaller energy depositions at the CEF, and therefore there is less/more energy in the SOBP region.

The increase of σ_x values make the gaussian become larger. For this reason, and keeping the same number of protons sent per spot, the fluence is transferred from the center to the periphery of the chimney. There are less protons going through the center and more protons going through the walls of the chimney. Therefore, there are less protons contributing to the deepest Bragg peak and more contributing to the less deep Bragg peak. For that reason, it is possible to observe that the decrease of deposited energy happens mainly at the deepest section of the SOBP.

Due to the high number of particles followed, the maximum relative error associated to the range and deposited energy simulations is 0.09%. This indicates that the observed changes are statistically significant.

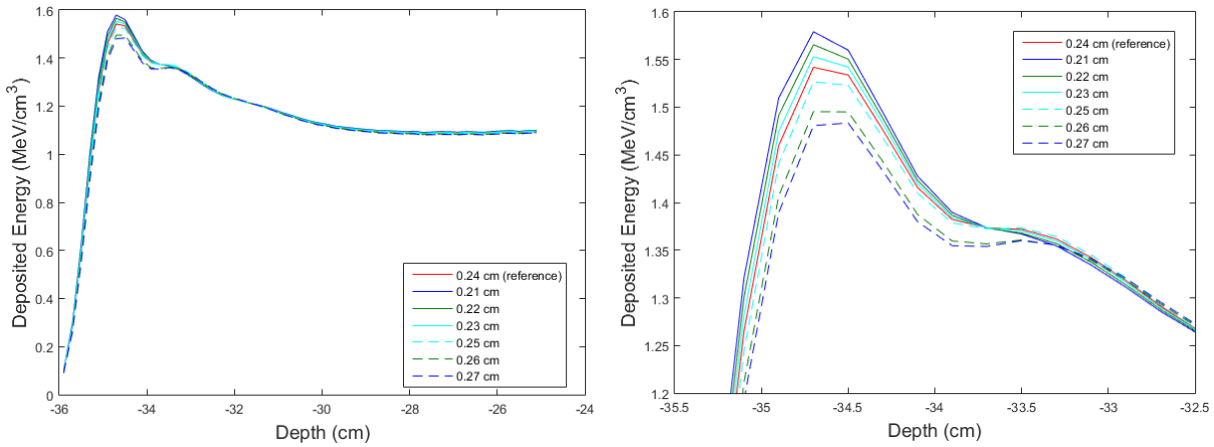

Figure 51 *Longitudinal profile of simulated SOBP curves. The results were obtained in the water phantom and are the results of different values of σ_x of the beam. The value of σ_y remains unchanged.*

Table 16 *Summary of R_{100} position and energy deposited by different values of σ_x, on the water phantom. The relative error associated to the simulations is 0.09%.*

σ_x (cm)	0.21	0.22	0.23	0.24	0.25	0.26	0.27
Maximum deposited energy (MeV/cm^3)	1.5792	1.5657	1.5530	1.5420	1.5266	1.4954	1.4835
Difference relative to the reference (%)	-2.412	-1.537	-0.713		0.999	3.022	3.794
R_{100} (cm)	-34.70	-34.70	-34.70	-34.70	-34.70	-34.70	-34.70
Difference relative to the reference (%)	0	0	0		0	0	0

Figure 52 shows the contour plots of the deposited energy difference between the reference situation and the different σ_x beam values simulated. It is possible to observe that, for σ_x values of 0.23 cm and 0.25 cm (error induction of ±0.01 cm), the percentual difference in the SOBP region is about 0.5% and 1%, respectively. For the σ_x values of 0.22 cm and 0.26 cm (error induction of ±0.02 cm), the percentual difference in the SOBP region is about 2% and 3%, respectively. For the σ_x values of 0.21 cm and 0.27 cm (error induction of ±0.03 cm), the percentual difference in the SOBP region is about 3% and 4%, respectively.

It is also possible to observe in Figure 52 that when the σ_x values used are superior to the reference, the deposited energy increases on the side zones of the graph, and the inverse happens when the σ_x values are inferior to the reference. This is explained by the distribution of protons that crosses the center and the chimney of the CEF, in each situation. When the σ_x values are superior to the reference situation, the values of deposited energy in the water phantom are superior to the reference situation, creating a positive percentual difference. When the σ_x values are inferior to the reference situation, the values of deposited energy distribution in the water phantom are inferior to the reference situation, creating a negative percentual difference.

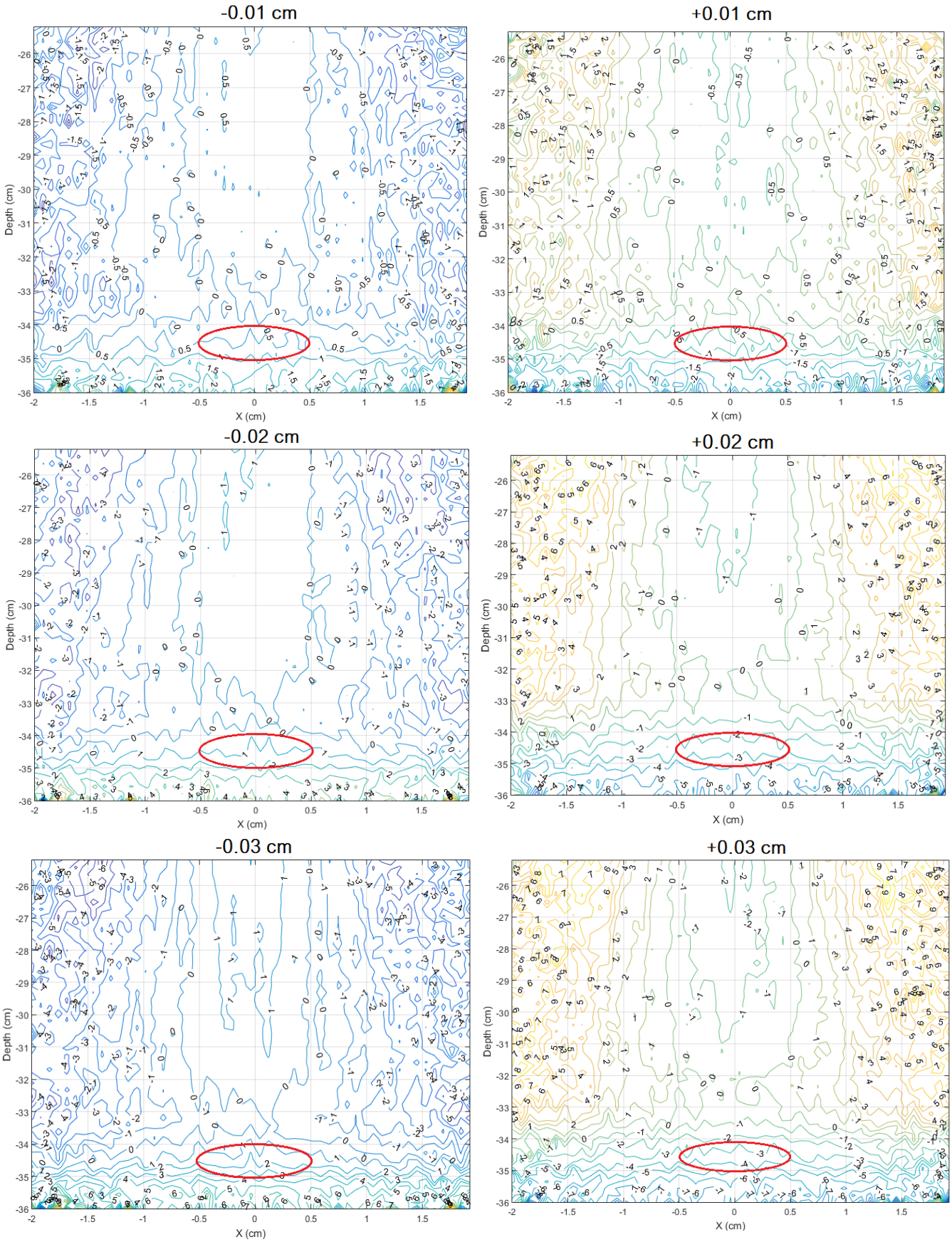

Figure 52 Contour plots of deposited energy (MeV/cm^3) difference between the reference geometry structure and the different values of σ_x simulated. The red ellipse represents the SOBP region, in the reference situation.

9.5. Lateral dimension change

This simulation aimed at quantifying the impact of alterations in the CEF lateral dimensions. For this purpose, two scenarios were simulated. On the first one, alterations on X and Y-axis were made, with respect to the reference dimensions. Those were reductions of 0.01 cm, 0.02 cm and 0.03 cm, at each step, from the top to the bottom, continually.

This means that for the reference situations, each of the several steps of the CEF have rectangular sections with dimensions:

Step 1:	0.7395<X<0.7395	0.7395<Y<0.7395
Step 2:	0.7389<X<0.7389	0.7389<Y<0.7389
Step 3:	0.7331<X<0.7331	0.7331<Y<0.7331
Step 4:	0.7068<X<0.7068	0.7068<Y<0.7068
Step 5:	0.6577<X<0.6577	0.6577<Y<0.6577
Step 6:	0.6136<X<0.6136	0.6136<Y<0.6136

from the top to the bottom. After the induced changes, they had values of

Step 1:	0.7395<X<0.7295	0.7395<Y<0.7295
Step 2:	0.7389<X<0.7189	0.7389<Y<0.7189
Step 3:	0.7331<X<0.7031	0.7331<Y<0.7031
Step 4:	0.7068<X<0.6968	0.7068<Y<0.6968
Step 5:	0.6577<X<0.6377	0.6577<Y<0.6377
Step 6:	0.6136<X<0.5836	0.6136<Y<0.5836),

from the top to the bottom. The values represent only the first 6 structures, the whole CEF being composed by 11 steps. On the second scenario, the alterations were made in the same order, but only in the X-axis.

By the results presented at Table 17, it is possible to conclude that the changes in CEF lateral dimensions didn´t impact the R_{100} but impacted the maximum deposited energy in the water phantom. In both situations, the changes led to more PMMA CEF volume than in the reference situation. When there is more material in the beam path, the protons attenuation is bigger, and the deposited energy will be inferior to the reference situation. Comparing both situations where changes were made, the alterations in X and Y-axis led to more CEF volume, comparatively to alterations in only X-axis. That is the reason why, the first one produces more proton attenuation than the second one. Due to the high number of particles followed in the simulation, the maximum relative error associated to range and deposited energy is 0.08%.

Table 17 Comparison of R_{100} and maximum deposited energy in the water phantom. The results refer to changes in the CEF lateral dimensions and reference simulation scenario. The maximum relative error associated to the simulation was 0.08%

Induced change	X and Y-axis changes	Reference	X-axis changes
Maximum deposited energy (MeV/cm^3)	1.5193	1.5420	1.5334
Difference relative to the reference (%)	-1.472		-0.558
R_{100} (cm)	-34.7	-34.7	-34.7
Difference relative to the reference (%)	0		0

Figure 53 presents the contour plots of the deposited energy difference between the reference and the CEF lateral dimension change on X and Y-axis. It is possible to observe that, in the SOBP region, the percentual difference produced is 2%. It is also possible to observe that the major differences are focused in the right area of the graphics since the changes were not made symmetrically, rather the variations we induced always increased sides of the rectangles with positive coordinates but not those with negative ones. Only the dimensions of one side of the CEF was changed, with the nominal values presented before.

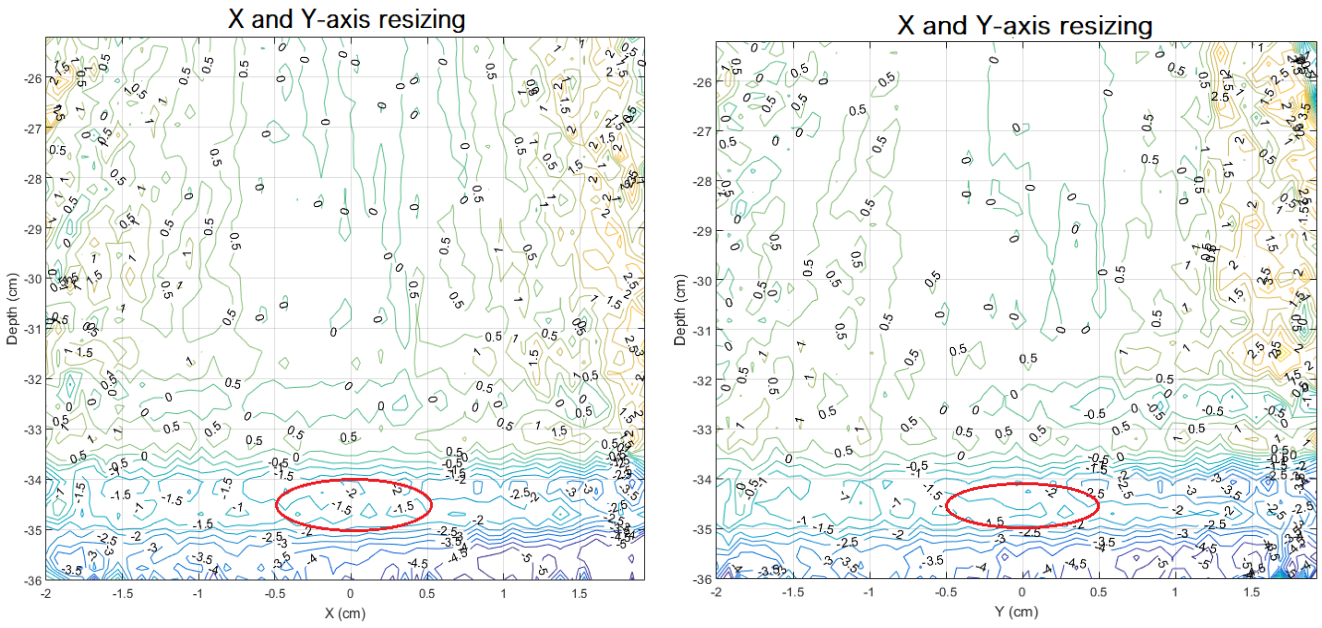

Figure 53 Contour plots of deposited energy (MeV/cm^3) difference between the reference geometry structure and lateral dimensions change in the CEF structure, on X and Y-axis. The red ellipse represents the SOBP area, in the reference situation.

Figure 54 presents the contour plots of the deposited energy difference between the reference and the CEF lateral dimension change on X axis. It is possible to observe that, in the SOBP region, the percentual difference produced is 0.5%. As in the previous graph, it is also possible to observe that the major differences are focused in the right area of the graphics since the changes were not made concentrically.

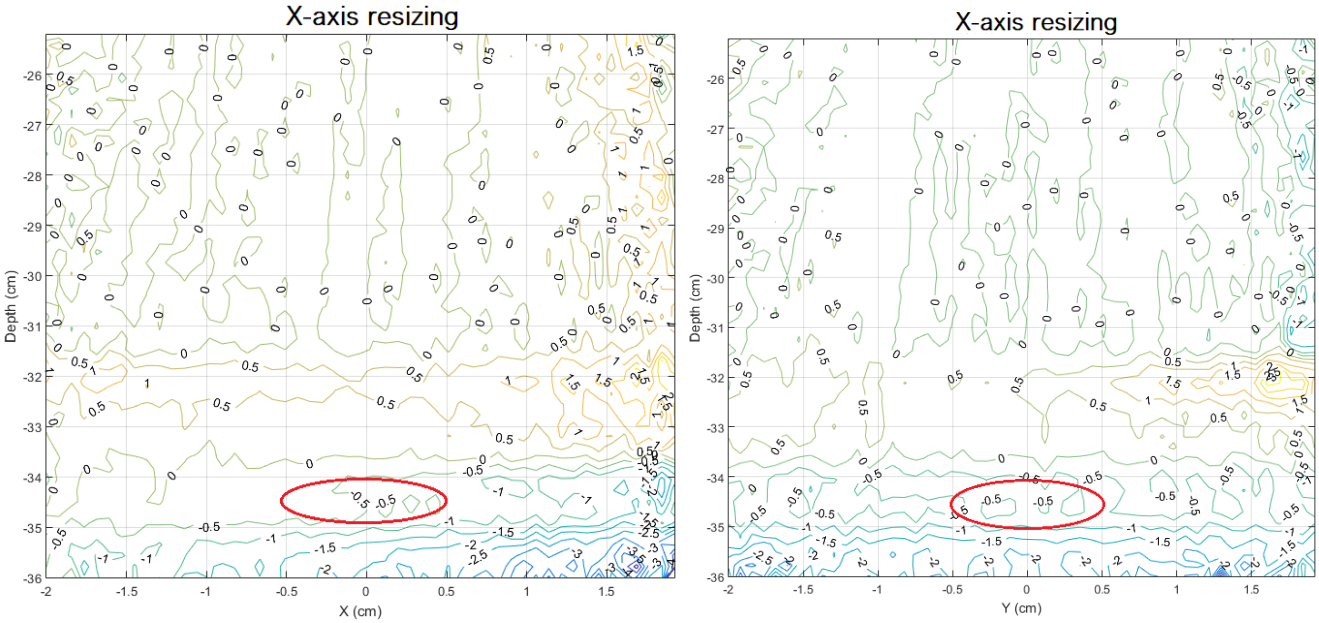

Figure 54 Contour plots of deposited energy (MeV/cm³) difference between the reference geometry structure and lateral dimensions change in the CEF structure, on X axis. The red ellipse represents the SOBP area, in the reference situation.

10. Neutron dose

Secondary neutrons are mostly generated by the interaction of the beam with the devices in the gantry, but also by the interactions of the radiation within the patient. The current knowledge shows that, in PTR, the neutrons are produced in a considerable amount for proton energies above 10 MeV. (8)

Despite the dose distribution of primary protons and secondary charged particles being limited around the target volume, the most concerning effect is the whole-body neutron dose exposure. The secondary neutrons can undergo significant scattering and cover 10 orders of magnitude in neutron energy, and their energy distribution is dependent of the proton beam energy and direction. (7,19) They are extremely penetrating particles and their RBE is about 20 times higher than for proton radiation. The neutron doses are typically <0.1% of the target dose and, since most TPS are not commissioned for low doses, their dose distribution is neglected in the majority of the cases. Therefore, it is not usually accounted for the induction of late effects.(19,67)

Studies on neutron RBE, neutron radiation quality factors, and neutron radiation weighting factors showed varying results and big errors. Therefore, it remains unclear how important the neutron contribution to the risk for late effects for a PTR patient is.(8)

Neutrons suffer elastic scattering processes at low energies (<1 MeV) and create protons and γ-rays by neutron capture. In an oxygen-rich medium, this is the most probable interaction, resulting in a loss of energy by the neutrons. In the low energy regions, the probability of neutrons slowing down is decreased because of the very few interactions with the material. The high energy neutrons transfer most of their energy via secondary protons in a few interaction events, resulting in protons with a wide range of energies (between zero and the incident neutron energies). These secondary protons can be produced anywhere inside the human body. This is translated in big exposure areas of small doses and, combined with the fact that the neutrons are uncharged particles, make the measurements and simulations very difficult and time consuming. Monte Carlo simulations are a powerful tool to determine neutron dose distributions within the patient and to study the influence of different devices in neutron production. (19)

The choice of dose quantity in neutron dosimetry is a point of controversy. There are different metrics to quantify the neutron dose in multiple contexts and many biologically weighted dose terms for radiation protection scenarios, and not RT. According to the International Commission on Radiological Protection (ICRP), the high-LET radiation should use absorbed dose weighted with an RBE for the investigated end point. In the case of neutrons this is difficult because the chosen end point might not have been measured and the reported neutron RBE has huge ranges. Due to this constraint, the AAPM task group 158 recommends using radiation protection quantities to report the neutron dose in Sv. (68)

Neutron ambient dose equivalent is an operational dose quantity for area monitoring and gives an estimate of the effective dose of a person standing at the point of interest in the neutron radiation field. Although a neutron detector can measure a value of neutron ambient dose equivalent in a specific location, the actual measurement value represents a whole-body neutron dose. Because of this, the values should be carefully interpreted and the limitations should be accounted in the context of RT. (8,69)

10.1. Standards for neutron doses

The standard criteria are established by “IEC60601-2-64 Type Test Grade B: clause 201.10.2.101.4.4 Neutron non-primary radiation outside the projection of the radiation field”.

The test requirement says that in the patient plane at distances lateral to the beam axis of 15 cm beyond the irradiated field, and less than 200 cm beyond the irradiated field (within region O in Figure 55), the estimated maximum absorbed dose from neutrons should not exceed 0,08 % of the dose that would be delivered at the central axis of the field.

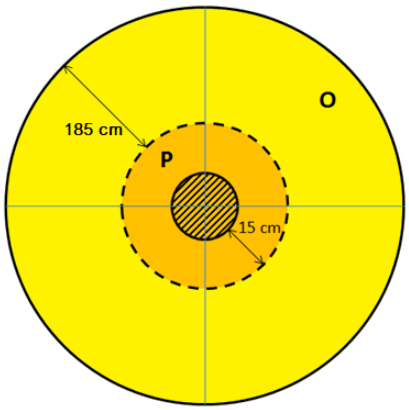

Figure 55 Definition of the different zones. The hatched area represents the irradiated field; zones "P" and "O" are defined respectively to that area.

The estimated value should be derived from measurements or calculations and the dose measurements or calculations should be done with an observer since the neutron dose measured without absorber would not be representative of the neutron dose in a typical patient treatment.

In our case, the center region of Figure 55 would be the center of the SOBP, and the beam would come from the top of the figure, vertically. Therefore, to be even more careful, we will take the values of the neutron dose at 15 cm from the center of the SOBP, along the X-axis.

10.1.1. Influence of the CEF material in neutron production

To study the influence of different CEF materials in neutron production, several simulations aiming at comparing 3 different materials were performed. The materials used for the CEF were PMMA, AL7050 and AISI4037, whose density and percentage of number of atoms is specified in Table 18.

The AL7050 is an alloy with good mechanical properties, good resistance to corrosion and very used in aerospace applications. The AISI4037 is a steel alloy with good response to heat treatments, also much used in aerospace industry.

Table 18 Specifications of the materials used in the simulation (PMMA, AL7050 and AISI4037), in terms of density and percentage of number of atoms. Carbon (c), Oxygen (O), Hydrogen (H), Aluminum (AL), Copper (Cu), Magnesium (Mg), Zinc (Zn), Zirconium (Zr), Iron (Fe), Manganese (Mn), Silicon (Si), Molybdenum (Mo), Sulfur (S) and Phosphorus (P).

Material	Density [g/cm^3]	Number of atoms (%)
PMMA	1.15	C (33.33%) + O (13.33%) + H (53.33%)
AL7050	2.6	Al (89%) + Cu (2.3%) + Mg (2.3%) + Zn (6.2%) + Zr (0.12%
AISI4037	7.85	Fe (97.98%) + Mn (0.7%) + C (0.35%) + Si (0.15%) + Mo (0.2%) + S (0.04%) + P (0.035%)

The simulations were performed in 2 different scenarios, as exemplified in Figure 56. The CEF dimensions were adjusted according to the material. In these simulations, the CEF was defined as a paralleliped shape, and the geometries presented before in earlier simulations were not used. In the case of using PMMA, the CEF dimensions were 3 x 3 x 6 cm. When using AL7050, the CEF dimensions were 3 x 3 x 3 cm. In the case of AISI4037, the CEF dimensions were 3 x 3 x 1 cm.

In the scenario where the range shifter was used, the material used for this structure was PMMA. The proton beam is represented by a black arrow in Figure 56. It moves along the Z-axis with an energy of 230 MeV and a uniform fluence distribution, covering the whole CEF in XY dimensions.

This approach was chosen for the results to represent the “worst-case scenario”, where the beam shapes, fluence distribution and CEF configuration was not optimized.

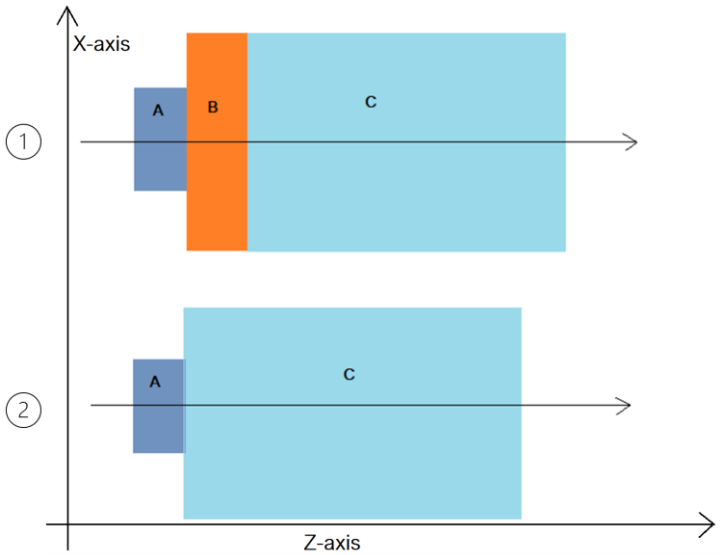

Figure 56 Illustration of the two simulation scenarios. The structure A is the CEF, whose dimensions were adjusted according to the material. The structure B represents the range shifter with dimensions of 40 × 40 × 12.29 cm. The structure C represents the water phantom, with dimensions of 40 × 40 × 40 cm. The figure is illustrative and is not on scale. The X and Z-axes are represented in the image and the arrow in the center of each assembly represents the beam direction.

The results of deposited energy per distance are presented in Figure 57. It is possible to observe that the Bragg peak range is smaller when the range shifter is used, compared to the cases where it isn’t. This is due to the presence of more material in the beam path, resulting in smaller ranges for the same initial energy.

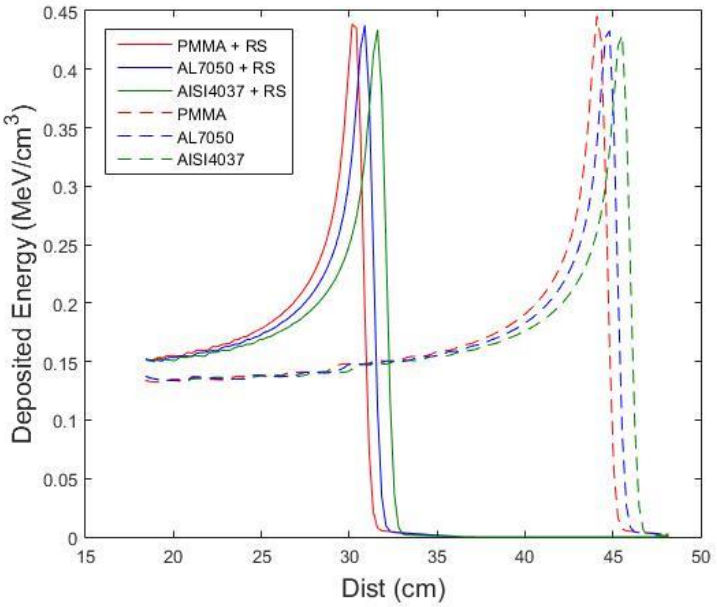

Figure 57 *Bragg peak representation for each simulation scenario.*

In Figure 58 we present the neutron dose as a function of the depth in the water phantom, in terms of effective dose (E) and ambient dose equivalent (H*(10)). Those values presented correspond to the whole X,Y plane, with values between -20 cm and 20 cm. The MCNPX calculate the neutron energy in each voxel and this value is presented as dose in Sieverts per Grays units, by using the conversion factors. The results presented are the effective dose (E) or ambient dose equivalent (H*(10)) of neutrons in mSv per Gy of proton dose.

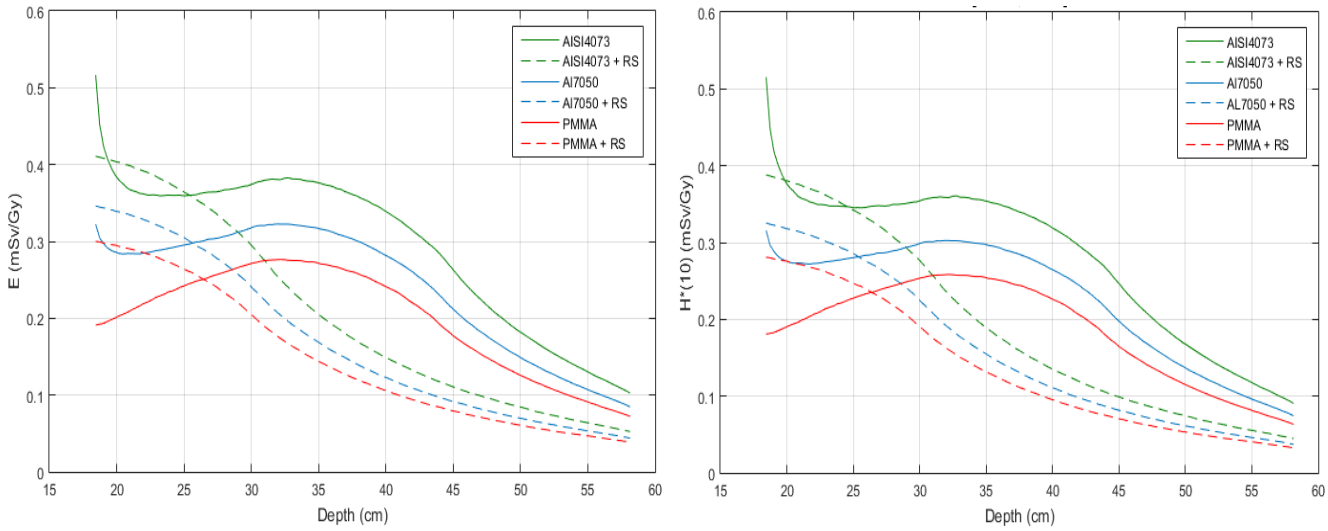

Figure 58 *Neutron production along the water phantom depth. The results are presented as neutron effective dose, E (on the left) and neutron ambient dose, H*(10) (on the right).*

The values of R_{100} of all particles, maximum effective dose (E), the depth z of maximum E, maximum H*(10), and the depth z of maximum H*(10) obtained in the different scenarios are presented in Table 19.

Table 19 Values of R_{100} of all particles, maximum E (E_{max}), R of maximum E (R_{Emax}), maximum H(10) ($H^*(10)_{max}$), and R of maximum H*(10) ($R_{H(10)max}$) obtained in the different scenarios*

	R_{100} (cm)	E_{max} (mSv/Gy)	R_{Emax} (cm)	$H^*(10)_{max}$ (mSv/Gy)	$R_{H(10)max}$ (cm)
AISI4037	45.5080	3.6743	18.29	3.5951	18.29
AISI4037+RS	31.6734	1.5471	18.29	1.4220	18.29
AL7050	44.6058	1.8282	18.29	1.7225	18.29
AL7050+RS	30.7712	1.3124	18.29	1.2087	18.29
PMMA	44.0043	1.0459	30.9216	0.9617	30.9216
PMMA+RS	30.1697	1.1453	18.29	1.0546	18.29

The results concerning each material and his combination with a RS are presented in Figure 59.

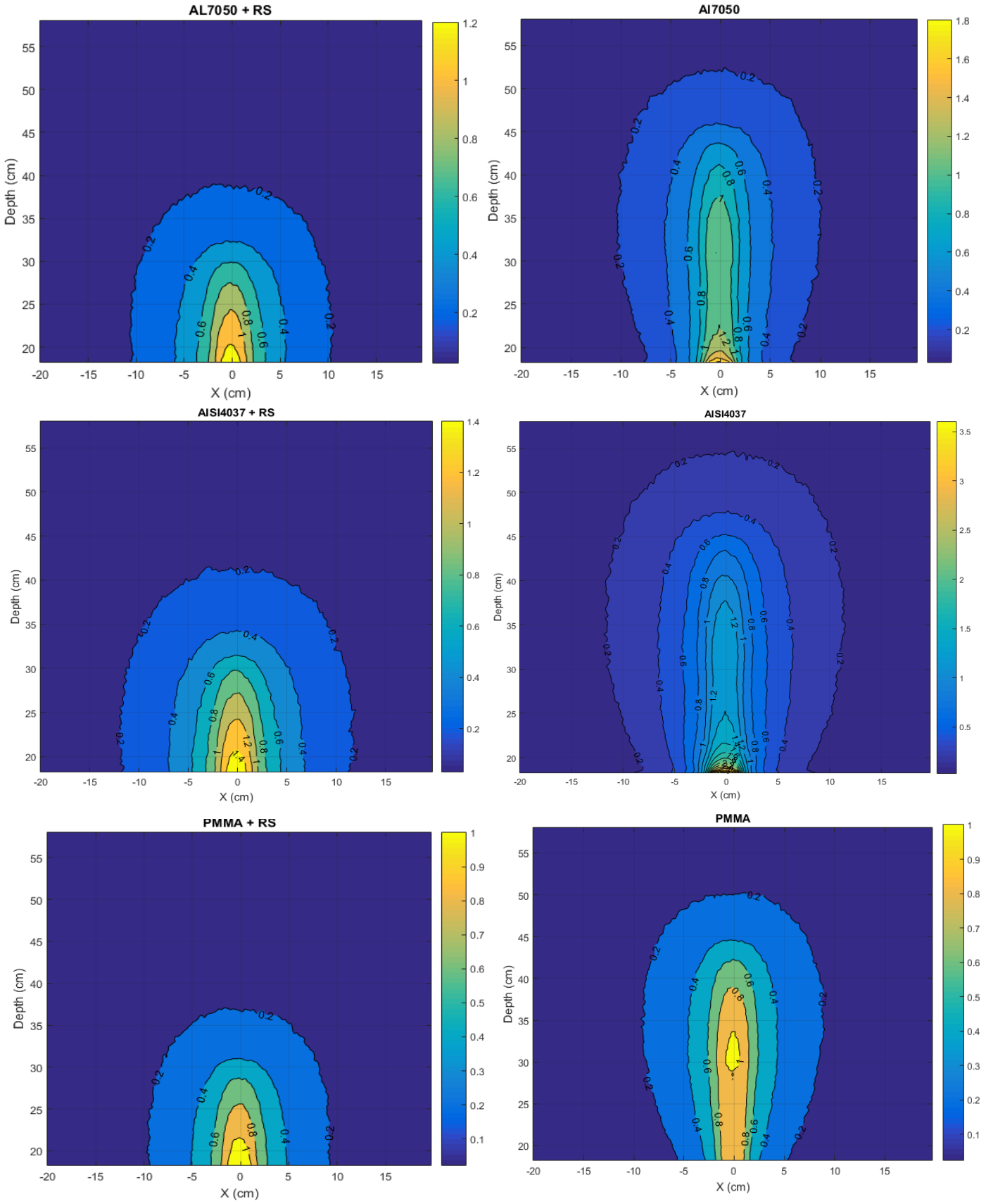

Figure 59 Neutron effective dose (mSv/Gy) distributions originated from different materials

There are two types of processes that explains the behavior observed in Figure 59. One is intra-nuclear cascade (INC) that is the first phase of proton-nucleus interactions, resulting in the production of high-energy neutrons (between 20 and 230 MeV). After the INC, the target nuclei are left in an excited state and they will go back to the ground state by emitting low-energy neutrons (between 0 and 20 MeV), called the evaporation phase. (70)

The neutrons with smaller energy will rapidly thermalize in a H-rich material such as PMMA or water. Contrary to INC neutrons, the yields of evaporation neutrons increase rapidly with the Z of the target material, what explains the fact of having much more neutrons produced in AISI compared to Al and PMMA. Thus, in the results obtained without RS, the differences seen at the beginning of the water phantom are due to the thermalization of evaporation neutrons produced in the CEF. After a few cm, those neutrons have been captured and we start to see the contribution from the INC neutrons. But, for the results obtained with RS, the evaporation neutrons produced in the CEF (and also the RS) are thermalized and captured inside the RS itself and are not able to reach the water phantom. Then, only the INC neutrons reach the water phantom. As they have lost some of their energy in the RS, it's not possible to observe the build-up as in the case of results without RS.

About the lateral spreading, neutrons are suffering from more scattering in the presence of RS than in the case of water alone.

It is also important to refer that AL alloys will rapidly get activated due to the production of unstable isotopes. If the usage of such material is considered, it is necessary to take into consideration that it is possible to end up with components that need to be treated as nuclear waste.

10.1.2. Influence of brass block in neutron production

This simulation aimed at seeing the influence of a brass block collimator to the neutron dose given to the patient. For this, we performed two simulation scenarios, as shown in Figure 60. The first simulated scenario is composed by the inverted rectangular CEF, a PMMA range shifter and a water phantom. The second simulated scenario is composed by the inverted rectangular CEF, a PMMA range shifter, a brass block with an aperture in the center and a water phantom. This aperture in the brass block has the same dimensions on X and Y-axis as the inverted rectangular CEF geometry.

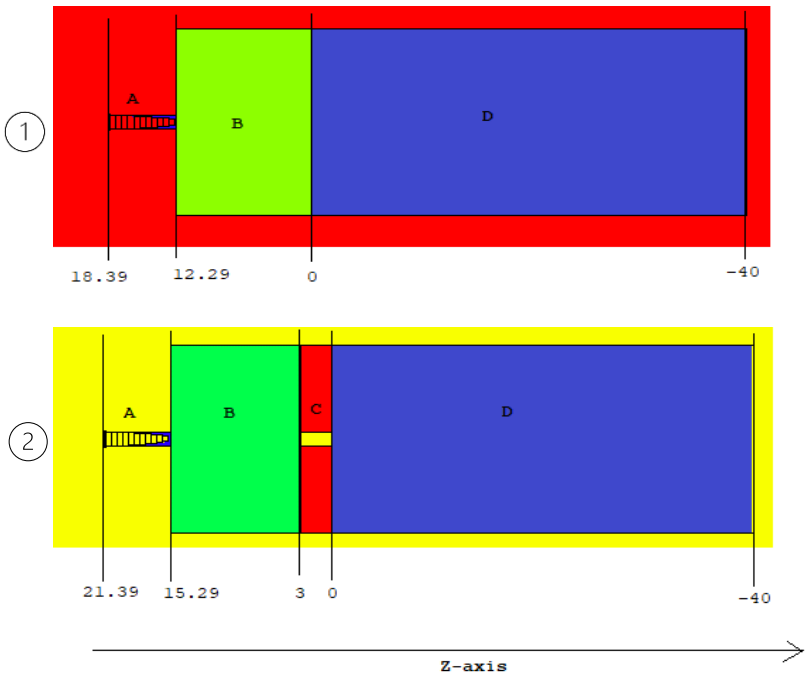

Figure 60 *Scheme of the two simulated scenarios. Image 1 is the first scenario, and the red zone represents air. Image 2 represents the second scenario, and the yellow zone corresponds to air. The A structure is the inverted rectangular CEF, with 6.1cm of length. The B structure correspond to the PMMA range shifter with 12.29 cm of length. The C structure correspond to the brass block, with 3 cm of length. In the center is visible a hole with the same dimensions of the inverted rectangular CEF, in X and Y-directions. The D structure correspond to the water phantom, with 40 cm of length.*

Table 20 specifies the brass composition, in terms of density and percentage of number of atoms. The values of percentage of number of atoms were given by IBA.

Table 20 *Specification of the materials used in the experiment, in terms of density and percentage of number of atoms. Copper (Cu), zinc (Zn) and lead (Pb).*

Material	Density [g/cm^3]	Percentage of number of atoms
Brass	8.52	Cu (57%) + Zn (40.5%) + Pb (2.5%)

Figure 61 shows the comparison between the simulation results of neutron effective dose (E), in mSv/Gy, between the two scenarios presented, scored in the water phantom. In the longitudinal representation, it is possible to observe that the neutron E is superior in the second scenario. This superiority is more pronounced at the entrance of the water phantom, at depth=0 cm, where the neutron E in scenario 1 is about 34% superior to the neutron E in scenario 2. This difference tends to diminish, and the values tend to equalize at bigger depths in the water phantom, at depth ≤ -30 cm.

This effect is due to the interaction of the incident protons with the brass block, which increase the number of nuclear reactions and leads to the formation of more secondary neutrons.

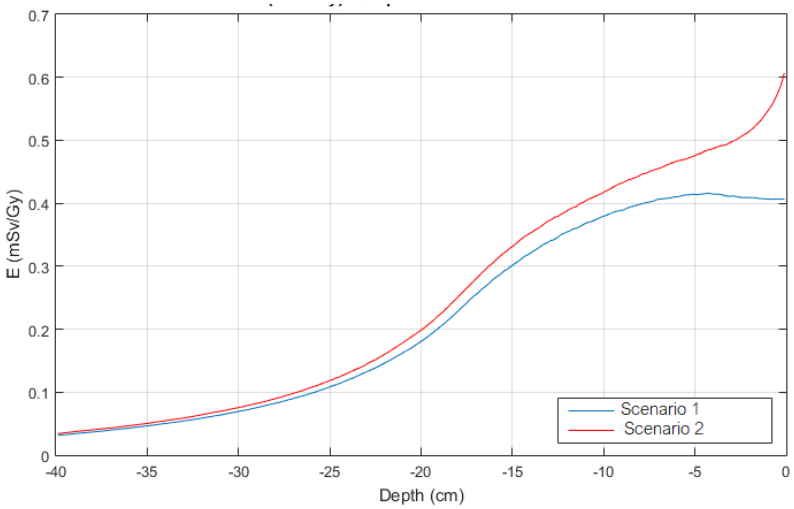

Figure 61 Neutron effective dose (mSv/Gy) simulation results between the two tested scenarios. The simulation results presented were obtained in the water phantom.

Figure 62 shows the contour plot of the neutron E (mSv/Gy) in the two simulated scenarios, in the transverse plane XZ. It is observed that in situation 2, the lateral dispersion of the dose is superior then in scenario 1. Also, the maximum neutron E is about 8.6% superior in scenario 2. For scenario 1, the maximum E is 1.452 mSv/Gy and for scenario 2 it is 1.5882 mSv/Gy.

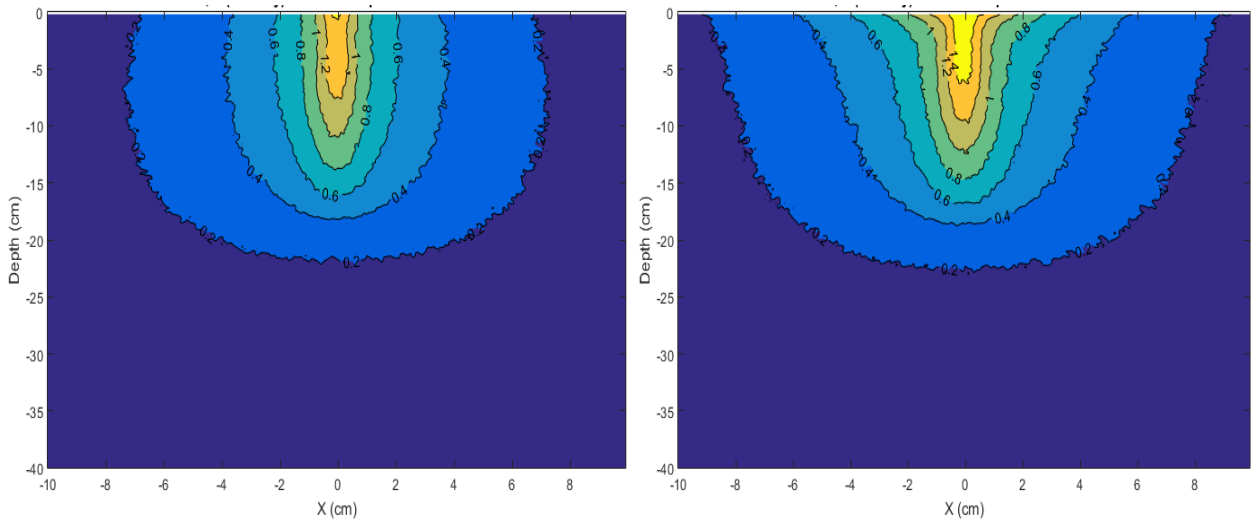

Figure 62 Transversal plot of neutron effective dose (mSv/Gy) in the water phantom. The figure on the left refers to simulation scenario 1 and the figure on the right refers to the simulation scenario 2.

Those simulation results cannot be compared with the ones from chapter 10.2.1 because in that scenario we have 6 cm of PMMA and here we have roughly the double, plus we use the CEF.

To verify the compliance with the neutron dose standards presented at chapter 10.2, we performed the calculation with values resulting from the simulations. For scenario 1, we took the

values of neutron dose percentage at 15 cm from the SOBP centre (1.204×10^{-15} Gy/source particle) and compared to the deposited dose from all the particles in the centre of the SOBP (2.142×10^{-11} Gy/source particle). With those values, we concluded that the neutron dose is 0.0056% of the dose given in the centre of the SOBP and the simulation of scenario 1 meet the requirements for acceptance.

For scenario 2, we took the values of neutron dose percentage at 15 cm from the SOBP centre (1.094×10^{-15} Gy/source particle) and compared to the deposited dose from all the particles in the centre of the SOBP (2.141×10^{-11} Gy/source particle). With those values, we concluded that the neutron dose is 0.0051% of the dose given in the centre of the SOBP and the simulation of scenario 2 meet the requirements for acceptance.

Those results can be justified by the fact that the collimator aperture is so big that it is only interacting with low dose penumbra of the spot. Despite this, in scenario 2 the beam interacts with more material than in scenario 1 but this will not have an impact on the neutron dose results.

10.1.3. Influence of beam positioning in neutron production

This simulation was performed to study the influence of beam positioning in proton and neutron dose distributions. The underlying idea was to make the proton beam incident at the edge of the collimator aperture and not in the center of the aperture, as is the case of a normal set-up. The configuration of the two simulated scenarios is represented in Figure 63.

The beam source was placed at (0, 0, 9.6) cm, and moves along in the Z-axis, in the negative sense. This beam had lateral dimensions that cover the CEF base and a gaussian particle distribution with $\sigma_x = 0.2386\ cm$ and $\sigma_y = 0.3698\ cm$.

The structure A represents the inverted rectangular CEF, with dimensions specified in section 8.3.

The structure B represents the range shifter, with 1.3 cm of thickness. The material used was AL7050 because it can produce a high proton scattering, resulting in a large beam spot size at the collimator.

The collimator, represented as C in the figure, is a 5×5 cm brass block. In the center of the structure was inserted a square hole with 2×2 cm in the inside. The width of the brass ring is 3 cm, and the thickness of the collimator is 2.2 cm. For the simulation of scenario 2, the collimator structure was shifted, in a way that the beam axis was incident at the border of the collimator inner aperture.

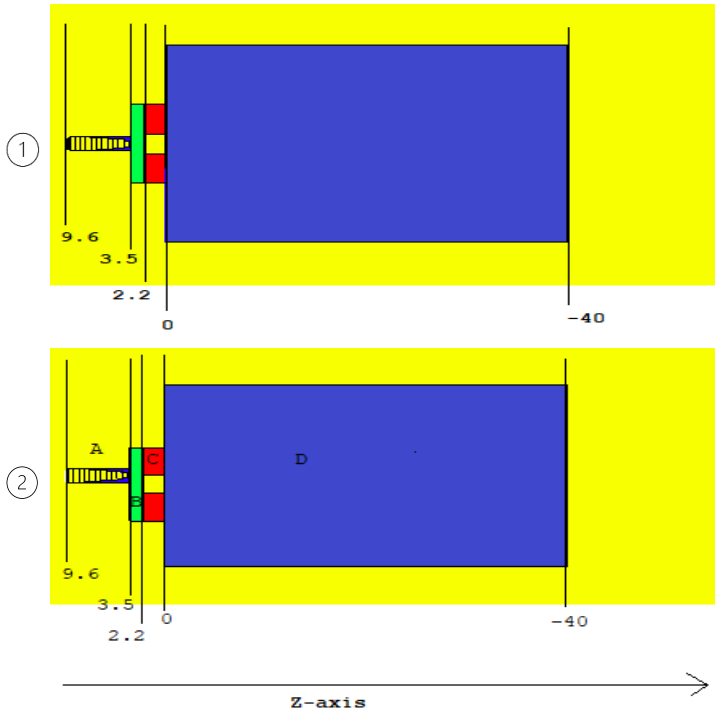

Figure 63 Simulation configuration. In the scenario 1, the beam is incident in the center of the brass block aperture; in the scenario 2, the beam is incident in the corner of the brass block aperture. The structure A represents the CEF, the structure B represent the range shifter, the structure C represent the collimator with an aperture in the center, the structure D represents the water phantom. The area colored as yellow is defined as air.

The energy deposition by all the particles in the problem (protons and neutrons) is represented below, in Figure 64. The calculation grid had a value of 20×20×0.2 cm = 80 cm^3. Due to the high number of particles used, the maximum relative error associated was 0.14%.

The large increase in deposited energy for scenario 2 observed at the depth of about -12 cm is obviously due to the fact that, in this scenario, the beam hits the brass block directly after crossing the range shifter. The interactions of the protons with the heavy nuclei of the brass block completely changes the profile of energy deposition compared to scenario 1.

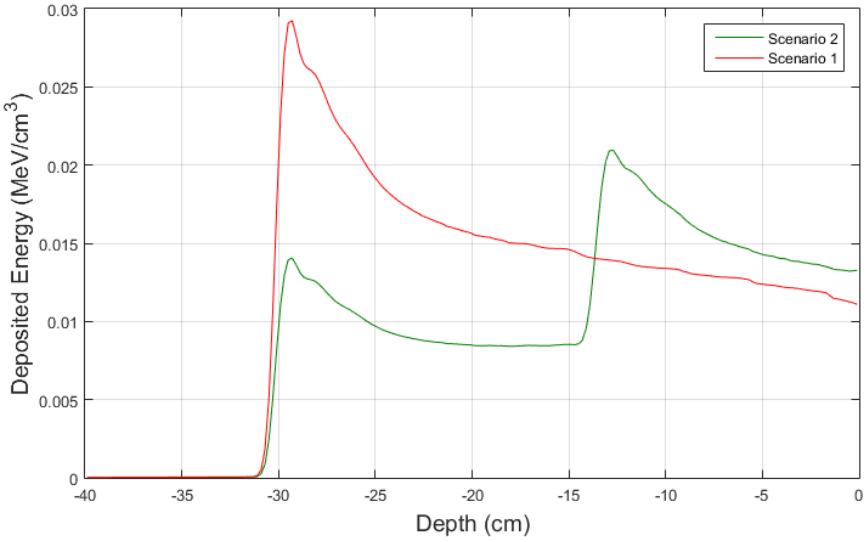

Figure 64 *Longitudinal profile of deposited energy (MeV/cm^3) by all the particles in the problem. The red line represents scenario 1 and the green line represents scenario 2.*

Table 21 summarizes the information of R_{100} (cm) and deposited energy at R_{100} (MeV/cm^3), in both simulated scenarios. It is possible to observe that R_{100} is equal in both scenarios and the main difference is in terms of the deposited energy at the point R_{100}. The deposited energy at R_{100} in scenario 1 is about 52% superior to scenario 2.

Table 21 *Comparison of R_{100} and deposited energy at R_{100}, in both simulated scenarios.*

	Scenario 1	Scenario 2
R_{100} (cm)	-29.3	-29.3
Deposited Energy at R_{100} (MeV/cm^3)	0.02924	0.01406

The deposited energy, as a function of depth, in scenario 1 is represented in Figure 65. The calculation grid had a value of 0.4 cm^3 and the contribution of all particles in the problem were considered.

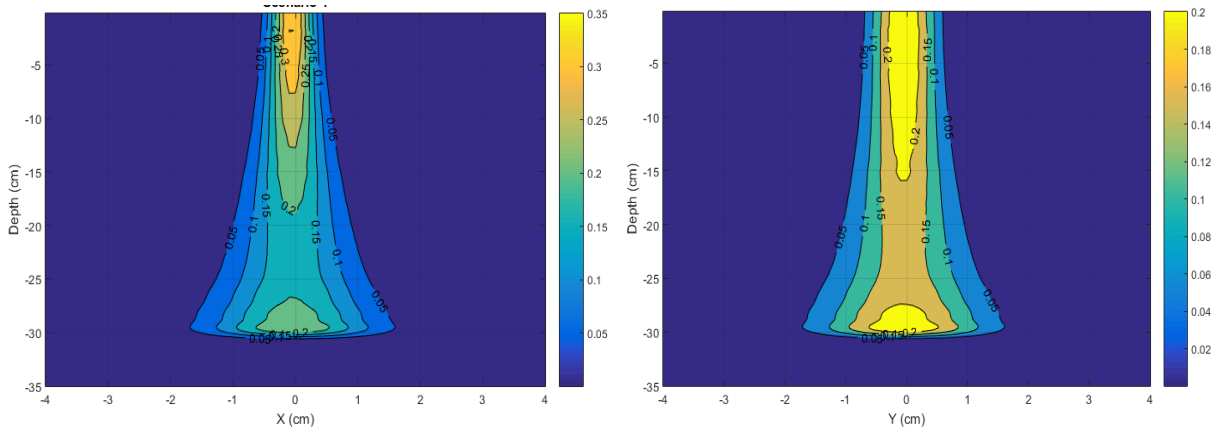

Figure 65 *Deposited energy (MeV/cm^3), as function of depth, in the water phantom by all particles in the problem. Both figures represent scenario 1.*

The deposited energy, as function of depth, in the scenario 2 is represented in Figure 66. The calculation grid had a value of 0.4 cm^3 and the contribution of all particles in the problem were considered. The irregularity observed in the distribution corresponds to the one observed in Figure 64.

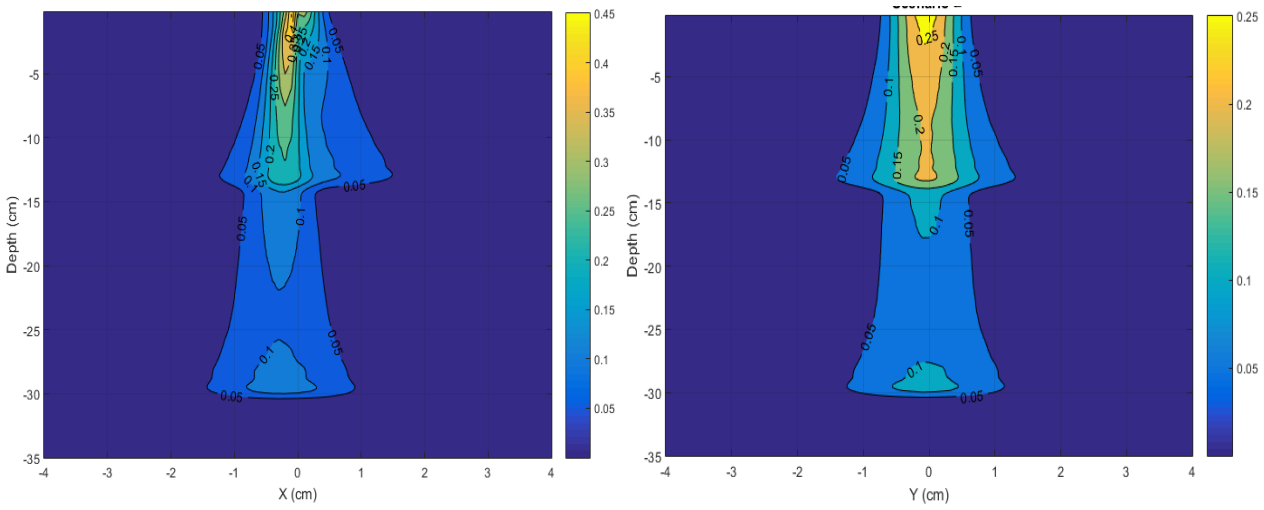

Figure 66 *Deposited energy (MeV/cm^3), as function of depth, by all particles in the problem. Representation of scenario 2.*

The neutron effective dose of both scenarios is represented in Figure 67. The calculation grid had a value of 20×20×0.2 cm = 80 cm^3. Due to the high number of particles used, the maximum relative error associated was 0.81%. The calculations to obtain the results in mSv/Gy from the results units given by MCNPX, in MeV/g per source particle, can be found in appendix 3

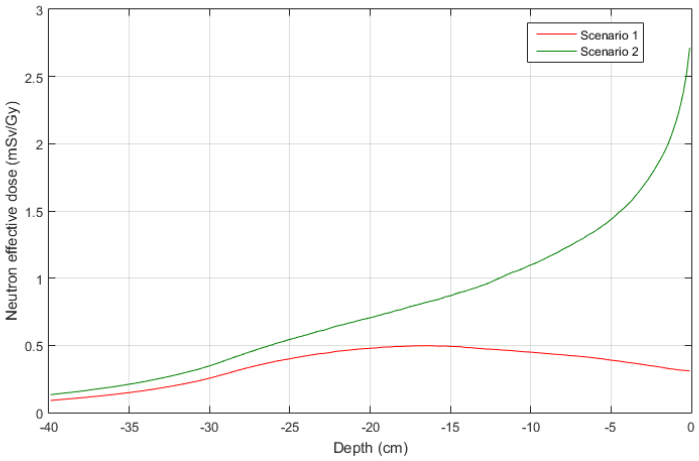

Figure 67 Longitudinal profile of neutron effective dose, as function of depth. The red line represents the scenario 1 and the green line represents the scenario 2.

It is possible to observe that the neutron effective dose in scenario 1 is 5.4 times superior than in scenario 2. These results are explained by the beam positioning and the materials that are present in the beamline. In scenario 2, the beam axis is incident in the corner of the collimator inside aperture. As explained before, the presence of more material in the beam line translates into more neutron production.

$$\frac{maximum\ in\ scenario\ 2}{maximum\ in\ scenario\ 1} = \frac{2.7}{0.5} = 5.4$$

The neutron effective dose, as function of depth, in scenario 1 is represented in Figure 68. The calculation grid had a value of 0.4 cm^3.

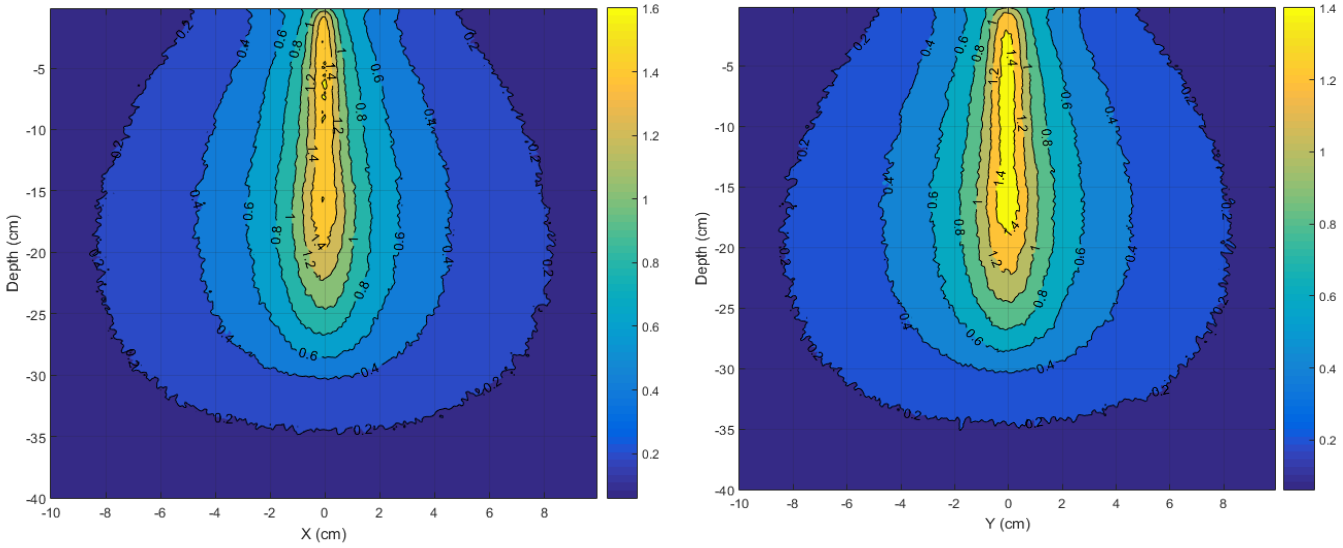

Figure 68 Neutron effective dose (mSv/Gy) in the water phantom, as function of depth. The results are from the simulation of scenario 1.

The neutron effective dose, as function of depth, in scenario 2 is represented in Figure 69. The calculation grid had a value of 0.4 cm^3.

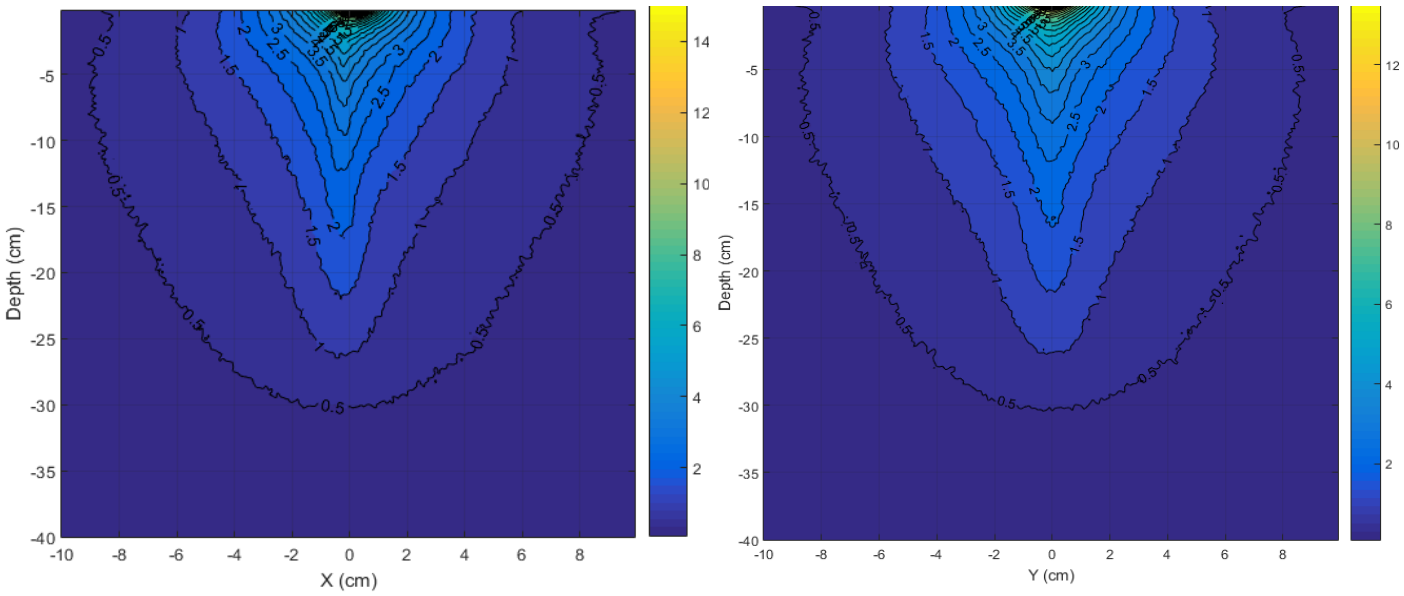

Figure 69 Neutron effective dose (mSv/Gy) in the water phantom, as function of depth. The results are from the simulation of scenario 2.

Table 22 shows the maximum neutron effective dose and the depth in the water phantom where that maximum is registered. In concordance with Figure 69, the maximum neutron E is registered in a more proximal region, closer to the region where the beam enters, in scenario 2, than in scenario 1.

Table 22 Maximum neutron energy and his depth on the water phantom.

	Scenario1		Scenario 2	
	XX	YY	XX	YY
Maximum neutron Energy (mSv/Gy)	1.6325	1.5458	15.2095	13.7328
Depth of maximum energy (cm)	-6.6	-15.4	-0.2	-0.2

To verify the compliance with the neutron dose standards presented at chapter 10.2, we performed the calculation with values resulting from the simulations. For scenario 1, we took the values of neutron dose percentage at 15 cm from the SOBP centre (1.193×10^{-15} Gy/source particle) and compared to the deposited dose from all the particles in the centre of the SOBP (1.957×10^{-11} Gy/source particle). With those values, we concluded that the neutron dose is

0.0061% of the dose given in the centre of the SOBP and the simulation of scenario 1 meets the requirements for acceptance.

For scenario 2, we took the values of neutron dose percentage at 15 cm from the SOBP centre (1.066×10^{-15} Gy/source particle) and compared to the deposited dose from all the particles in the centre of the SOBP (9.168×10^{-12} Gy/source particle). With those values, we concluded that the neutron dose is 0.012% of the dose given in the centre of the SOBP and the simulation of scenario 2 also meets the requirements for acceptance.

11. Conclusions

This work investigated the sensitivity of the CEF structure to several uncertainties. The CEF primary studied application was to be able to administer FLASH-RT. Besides that, the FLASH component was not much addressed in this work but it is the key purpose to develop the CEF. The focus was the robustness study of the hardware solution, by using Monte Carlo simulations.

The Monte Carlo simulator used was MCNPX, a very complex program that requires a big learning curve. Nevertheless, the results obtained have statistical significance to support the conclusion process.

The simulations were made with a CEF structure from January 2021. Because this is a ongoing investigation within IBA, the CEF prototype suffered amelioration changes that were not contemplated in this work. It is therefore recommended to repeat these simulations with the latest version of the CEF and the eventual actualization in the other components. However, because the results presented are a percentual comparison between an unchanged situation and a situation with uncertainty associated, the resultant impact can be extrapolated.

We started by simulating three CEF structures in MCNPX and choose the one that produces SOBP results closer to the desired ones. The goal was to observe a SOBP in the water phantom, after the proton beam crosses the simulated assembly. This test assembly is composed by a CEF tower, a range shifter and a collimator with a central aperture (see figure 39 in chapter 9). The simulation results obtained with each CEF structure are presented in figure 37 (chapter 8.3.3) and justify the choose of the inverted rectangular CEF to perform the simulations, since it allows to obtain the flatter SOBP.

The robustness tests were made with a lead collimator. Usually, the collimator material is brass. In terms of density, the materials are similar and, because of this, their influence in proton range is almost equivalent. It is acceptable to do the robustness tests with this material, without too much interference in the results. When studying the neutron dose production, the two materials are not equivalent and that's why the collimator material is different in the two situations.

Figure 70 shows the relative difference for the deposited energy at the SOBP region from the reference simulation and the simulations where uncertainties in beam positioning were made. In this simulation, the proton beam was positioned in different points. For this purpose, the Z and Y-axis coordinates were left the same in all scenarios and the X-coordinate was changed from simulation to simulation. It is possible to see that as we increase the magnitude of the beam translation, we increase the relative difference between the scenarios. This relative difference reaches 8% in the situation where the beam had a shift of 0.1 cm in X-axis.

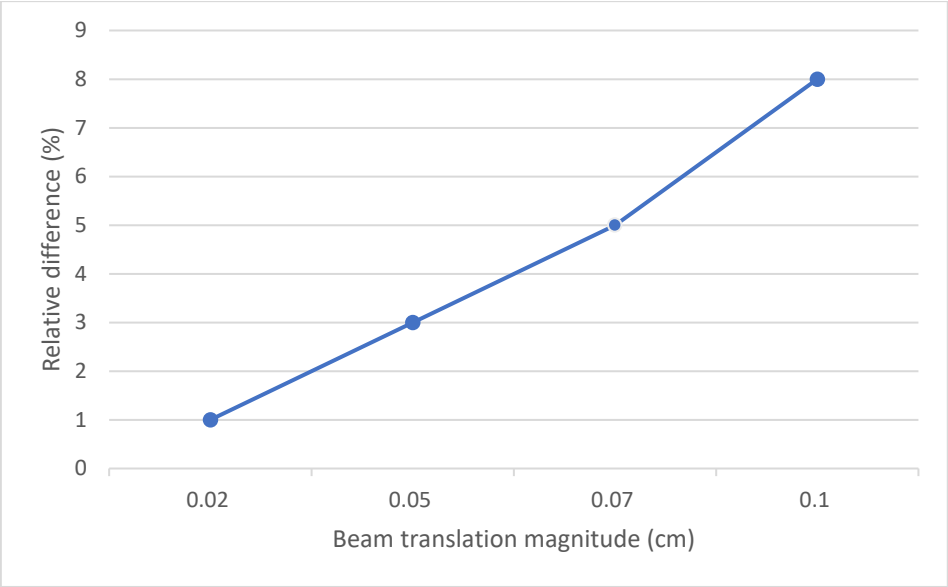

Figure 70 *Simulation results for the relative difference of deposited energy in the SOBP region as a function of uncertainties in beam translation (0.02, 0.05, 0.07 and 0.1 cm).*

Figure 71 shows the relative difference results of deposited energy, when inducing different beam angles. For this purpose, there were induced different beam angulations (0.2º, 0.5º and 1º), relative to the beam path, Z-axis. The simulations show that there is no difference from the reference situation and the 0.2º beam angulation situation. For a beam angulation of 0.5º, the relative difference observed was 0.6%, and for 1º it was 5%. Because we have such different values for the deposited energy relative difference produced by 0.5º and 1º, it is therefore important to simulate more beam angulations between those values, in order to identify the acceptance threshold.

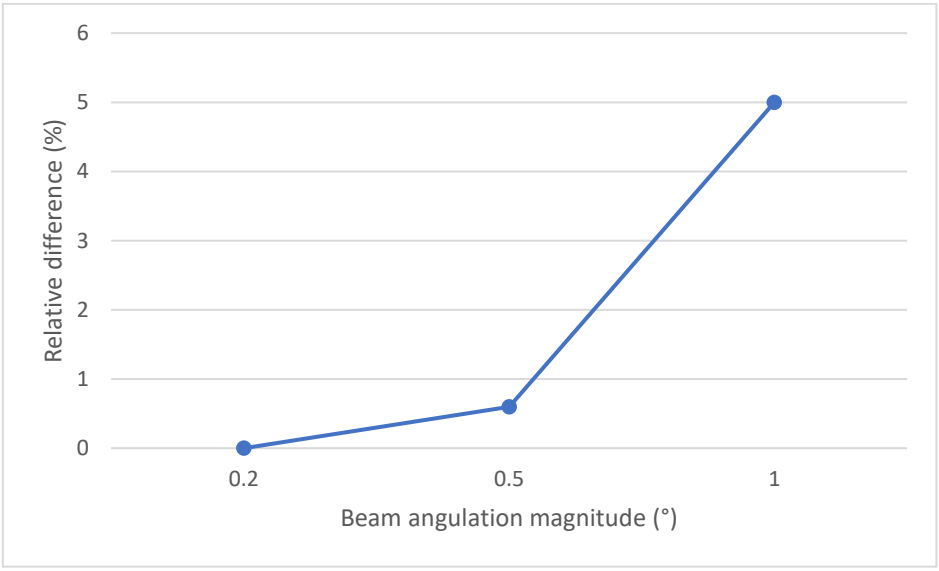

Figure 71 *Simulation results of the relative difference of deposited energy in the SOBP region as a function of uncertainties in the beam angulation (0.2º, 0.5º and 1º).*

Figure 72 present the relative difference of deposited energy results when comparing the simulated results from a reference scenario with standard material density reported to the CEF material and situations where this density was altered. The differences in the CEF material were calculated in terms of percentage, in the positive and negative sense. Meaning that we simulated scenarios where the CEF had less material density than the reference (-1%, -2% and -3%), and scenarios where the CEF had more material density than the reference (1%, 2% and 3%). By analyzing the simulation results, it is possible to conclude that the cases where the biggest relative difference was observed was in the extreme case (-3% and 3%). If we observe Figure 50 (chapter 9.3), we can see that in the case where we have less CEF material density (-3%), we will have more deposited energy in the SOBP area, and in all the proximal region to that. In the same figure, if we observe the situation where the CEF has more material density (3%) than the reference scenario, we will have less deposited energy in the SOBP area. This is explained by the fact of having more or less material in the beam path and the energy attenuation that this will produce.

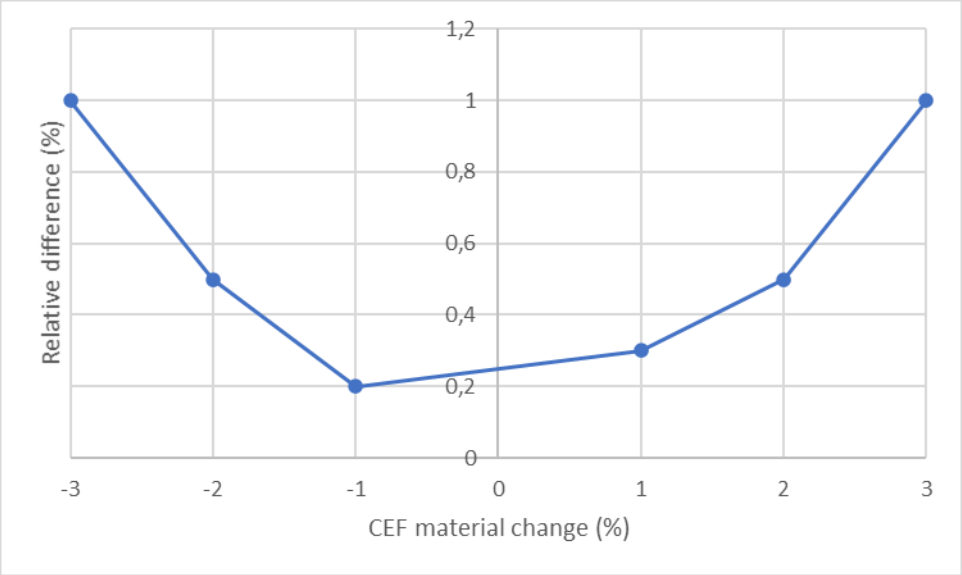

Figure 72 Simulation results of the relative difference of deposited energy in the SOBP region as a function of uncertainties in the CEF material density.

In Figure 73 we present the results of uncertainty in the beam dimensions. We simulated scenarios where the beam had smaller dimensions than the reference situation (-0.01, -0.02 and -0.03 cm) and where the beam had bigger dimensions than the reference situation (0.01, 0.02 and 0.03 cm). Those values were changes with respect to the σ_X, and the values of σ_Y were kept the same through the simulations. It is possible to observe that in the extreme cases, where we have -0.03 cm and 0.03 cm in the beam size, the percentual difference is 3% and 4%,

respectively. It is important to refer that, for changes that make the beam larger, the fluence can be stopped by the collimator, if the interior whole has dimensions coincident with the CEF ones.

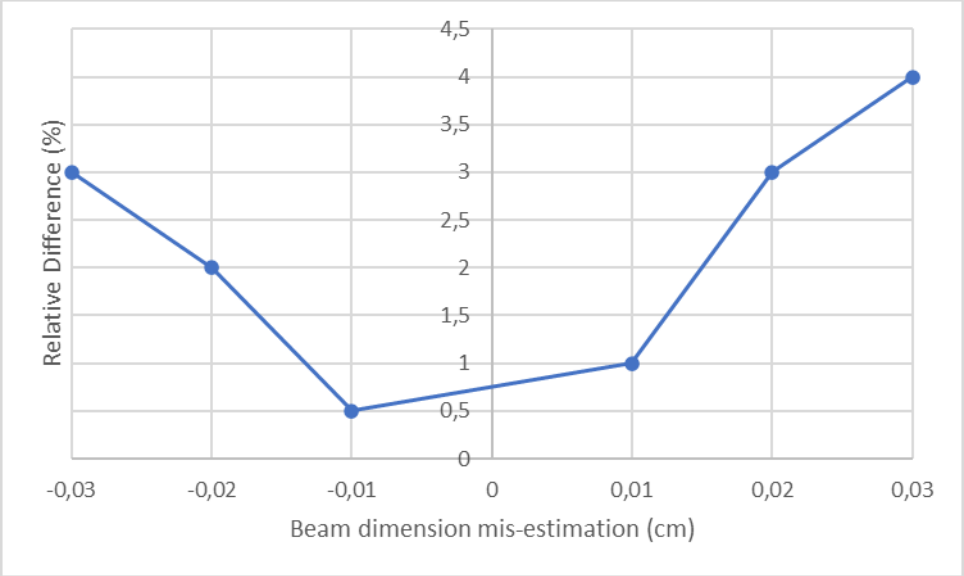

Figure 73 Simulation results of the relative difference of deposited energy in the SOBP region as a function of uncertainties in the beam dimensions.

For the scenario where we simulated CEF lateral dimensions change, the percentual difference in the SOBP area observed was -0.5% for X-axis reshaping and -2.5% for X and Y-axis reshaping.

We should assume that those errors can occur in a random way, with the same individual probability. That said, we can conclude that the uncertainty that mostly impacts the dose deposition in the SOBP area is the beam translation of 0.1 cm with 8% percentual difference, followed by beam angulation of 1º with 5% percentual difference. It could also be important to study the impact of having multiple errors happening at the same time and what is the effect of the summed errors.

We also simulated different scenarios to observe the influence of secondary neutrons in the dose distribution. To this purpose, and unlike what was done in this work, it would be important to simulate the whole beamline since the majority of neutrons are created by the interaction of the proton beam with the devices in the way. In this work, we considered that the proton beam comes from the nozzle and didn't take into account any interactions before that.

In the neutron simulation where we compare 3 materials (PMMA, AL7050 and AISI4037) to see the impact on neutron production, we can conclude that the PMMA is the one that contributes less to this effect. We conclude also that we could exclude the AL7050 from the considerations, because this material can become activated during the irradiation process and

will increase the quantity of nuclear waste, since the CEF is personalized and individualized for every patient and beam angulation.

We also conclude that the usage of a brass block influences the neutron production in the entrance proximal region of the beam but not in a significant way. The simulation results were compared to the standard of acceptance of secondary neutron doses and the conclusion was that both scenarios (with or without brass block) produce values within the acceptance threshold. The requirement for neutron dose acceptance says that at 15 cm from the central axis of the field, the estimated maximum absorbed dose from neutrons should not exceed 0,08 % of the dose that would be delivered at the central axis of the field. The results can be influenced by having a brass block aperture too big. The brass block will only interact with the penumbra region of the beam, that has smaller energy and, therefore, the neutron production will not be substantial.

On the other hand, we observed that by changing the position of the CEF to a spot not centered with the brass block aperture, the neutron dose production will be influenced. By changing the CEF position from the center of the aperture to a point where his axis was centered with the corner of the aperture, we observed that the percentage of the neutron dose produced at 15 cm from the center of the SOBP relative to the total dose in the center of the SOBP increased from 0.0061% to 0.012%, respectively. This meets the requirements for neutron dose protection and the values are within the established threshold.

For all the simulations performed, we can conclude that the neutron dose requirements were always within the acceptance threshold.

In future works, it would be important to simulate the effects of uncertainties and neutron production with the latest version of the CEF.

12. Bibliographical references

1. Ebrahimi Loushab M., Mowlavi A. A HMH, Izadi R. JSB. Impact of Various Beam Parameters on Lateral Scattering in Proton and Carbon-ion Therapy. J Biomed Phys Eng. 2015;51–60.
2. Paganetti H. Proton beam therapy. In: Physics World Discovery. IOP Publishing; 2017. p. 1–13.
3. Goitein M. Radiation Oncology: A Physicist's Eye View. [Internet]. Br J Radiol. Springer; 2009. Available from: http://bjr.birjournals.org
4. Mohan R, Grosshans D. Proton therapy – Present and future. Adv Drug Deliv Rev [Internet]. 2016;109:26–44. Available from: http://dx.doi.org/10.1016/j.addr.2016.11.006
5. Valdivieso M, Kujawa AM, Jones T, Baker LH. Cancer survivors in the united states: A review of the literature and a call to action. Int J Med Sci. 2012;9(2):163–73.
6. Moor JS De, Mariotto AB, Parry C, Alfano CM, Padgett L, Kent EE, et al. Cancer Survivors in the United States: Prevalence across the Survivorship Trajectory and Implications for Care. Cancer Epidemiol Biomarkers Prev. 2013;1–17.
7. Newhauser WD, Zhang R. The physics of proton therapy. Phys Med Biol. 2015;60(8):R155–209.
8. Hälg RA, Schneider U. Neutron dose and its measurement in proton therapy- current State of Knowledge. Br J Radiol. 2019;93(1107).
9. Particle Therapy Co-Operative Group (PTCOG). Particle therapy facilities in clinical operation [Internet]. [cited 2021 Apr 20]. Available from: https://www.ptcog.ch/index.php/facilities-in-operation
10. Particle Therapy Co-Operative Group (PTCOG). Particle therapy facilities under construction [Internet]. [cited 2021 Apr 20]. Available from: https://www.ptcog.ch/index.php/facilities-under-construction
11. Souris K. Accurate assessment of proton therapy treatments: fast Monte Carlo dose engine and extensive robustness tests [Internet]. Université Catholique de Louvain; 2018. Available from: https://dial.uclouvain.be/pr/boreal/object/boreal:192917
12. Montay-Gruel P, Petersson K, Jaccard M, Boivin G, Germond JF, Petit B, et al. Irradiation in a flash: Unique sparing of memory in mice after whole brain irradiation with dose rates

above 100 Gy/s. Radiother Oncol [Internet]. 2017;124(3):365–9. Available from: http://dx.doi.org/10.1016/j.radonc.2017.05.003

13. Favaudon V, Caplier L, Monceau V, Pouzoulet F, Sayarath M, Fouillade C, et al. Ultrahigh dose-rate FLASH irradiation increases the differential response between normal and tumor tissue in mice. Sci Transl Med. 2014;6(245).

14. Vozenin MC, De Fornel P, Petersson K, Favaudon V, Jaccard M, Germond JF, et al. The Advantage of FLASH Radiotherapy Confirmed in Mini-pig and Cat-cancer Patients. Clin Cancer Res. 2018;25(1):35–42.

15. Simeonov Y, Weber U, Penchev P, Ringbæk TP, Schuy C, Brons S, et al. 3D range-modulator for scanned particle therapy: Development, Monte Carlo simulations and experimental evaluation. Phys Med Biol. 2017;62(17):7075–96.

16. Patriarca A, Fouillade C, Auger M, Martin F, Pouzoulet F, Nauraye C, et al. Experimental Set-up for FLASH Proton Irradiation of Small Animals Using a Clinical System. Int J Radiat Oncol Biol Phys. 2018;102(3):619–26.

17. Ciangaru G, Polf JC, Bues M, Smith AR. Benchmarking analytical calculations of proton doses in heterogeneous matter. Med Phys. 2005;32(12):3511–23.

18. Newhauser W, Fontenot J, Koch N, Dong L, Lee A, Zheng Y, et al. Monte Carlo simulations of the dosimetric impact of radiopaque fiducial markers for proton radiotherapy of the prostate. Phys Med Biol. 2007;52(11):2937–52.

19. Paganetti H. Proton Therapy Physics. CRC Press; 2012.

20. Paganetti H. Nuclear interactions in proton therapy: Dose and relative biological effect distributions originating from the primary and secondary particles. Phys Med Biol. 2002;47(5):747–64.

21. DeLuca PM. ICRU REPORT 78: Prescribing, Recording, and Reporting Proton-Beam Therapy. Vol. 7, International Comission on Radiation Units and Measurements. Oxford University Press; 2007.

22. International Comission on Radiation Units and Measurements. ICRU Report 62: Prescribing, recording and reporting photon beam therapy (Supplement to ICRU Report 50). USA; 1999.

23. Lee CC, Lee YJ, Chen SK, Chiang BH, Tung CJ, Chao TC. MCNPX simulation of proton dose distributions in a water phantom. Biomed J. 2015;38(5):414–20.

24. Appendix: Significance of Calculated Quantities [Internet]. National Institute of Standards and Technologies (NIST). [cited 2021 Jul 12]. Available from: https://physics.nist.gov/PhysRefData/Star/Text/appendix.html

25. Parodi K, Paganetti H, Shih HA, Michaud S, Loeffler JS, DeLaney TF, et al. Patient Study of In Vivo Verification of Beam Delivery and Range, Using Positron Emission Tomography and Computed Tomography Imaging After Proton Therapy. Int J Radiat Oncol Biol Phys. 2007;68(3):920–34.

26. Nischwitz SP, Bauer J, Welzel T, Rief H, Jäkel O, Haberer T, et al. Clinical implementation and range evaluation of in vivo PET dosimetry for particle irradiation in patients with primary glioma. Radiother Oncol [Internet]. 2015;115(2):179–85. Available from: http://dx.doi.org/10.1016/j.radonc.2015.03.022

27. Bentefour EH, Shikui T, Prieels D, Lu HM. Effect of tissue heterogeneity on an in vivo range verification technique for proton therapy. Phys Med Biol. 2012;57(17):5473–84.

28. Seuntjens JP, Strydom W, Shortt KR. Dosimetric principles, quantities and units. In: Podgorsak EB, editor. Radiation Oncology Physics: a handbook for teachers ans students. International Atomic Energy Agency; 2005. p. 45–70.

29. Mayles P, Nahum A, Rosenwald JC, editors. Handbook of Radiotherapy Physics: Theory and Practice. Taylor & Francis Group, LLC; 2007.

30. Petoussi-Henss N, Bolch WE, Eckerman KF, Endo A, N. H, Hunt J, et al. Conversion Coefficients for Radiological Protection Quantities for External Radiation Exposures. ICRP Publication 116. Vol. 40, Annals of the ICRP. 2010.

31. VolumeViz. What is VolumeViz? [Internet]. [cited 2021 Dec 1]. Available from: https://developer.openinventor.com/UserGuides/Oiv10/Users_Guide/VolumeViz/Overview/What_is_VolumeViz.html

32. Sayah R, Donadille L, Aubé A, Hérault J, Delacroix S, De Marzi L, et al. Monte Carlo simulation of a proton therapy beamline for intracranial treatments. Radioprotection. 2013;48(3):317–39.

33. Bellinzona VE, Ciocca M, Embriaco A, Fontana A, Mairani A, Mori M, et al. On the parametrization of lateral dose profiles in proton radiation therapy. Phys Medica [Internet]. 2015;31(5):484–92. Available from: http://dx.doi.org/10.1016/j.ejmp.2015.05.004

34. Han SE, Cho G, Lee SB. An Assessment of the Secondary Neutron Dose in the Passive Scattering Proton Beam Facility of the National Cancer Center. Nucl Eng Technol [Internet].

2016;49(4):801–9. Available from: http://dx.doi.org/10.1016/j.net.2016.12.003

35. Mather SJ, Mansi L. Absorbed Dose Determination in External Beam Radiotherapy. Vol. 398, International Atomic Energy Agency (IAEA). 2000.

36. Berger MJ, Coursey JS, Zucker MA, Chang J. Stopping-Power & Range Tables for Electrons, Protons, and Helium Ions [Internet]. NIST Standard Reference Database 124. 2017 [cited 2021 Jul 1]. Available from: https://www.nist.gov/pml/stopping-power-range-tables-electrons-protons-and-helium-ions

37. Moyers MF, Coutrakon GB, Ghebremedhin A, Shahnazi K, Koss P, Sanders E. Calibration of a proton beam energy monitor. Med Phys. 2007;34:1952–66.

38. Park SH, Jung WG, Suh TS, Jang HS, Choi BO, Rah JE, et al. Variation of Bragg curve characteristic induced by changing the position of inhomogeneous material: Geant4 simulation study. J Korean Phys Soc. 2011;58(2):187–97.

39. Shirmardi SP, Saniei E, Erfani M, Shafiei M, Sepehri B. Tissue inhomogeneity in proton therapy and investigation of its effects on BRAGG peak by using MCNPX code. Int J Radiat Res. 2014;12(4):335–41.

40. National Institute of Standards and Technology (NIST). Composition of bone, cortical (ICRP) [Internet]. [cited 2021 Jul 2]. Available from: https://physics.nist.gov/cgi-bin/Star/compos.pl?refer=ap&matno=120

41. Kaiser A, Eley JG, Onyeuku NE, Rice SR, Wright CC, McGovern NE, et al. Proton Therapy Delivery and Its Clinical Application in Select Solid Tumor Malignancies. J Vis Exp. 2019;(144):1–12.

42. O'Steen L, Indelicato DJ. Advances in the management of craniopharyngioma. F1000Research. 2018;7(0):1–8.

43. Verhaegen F, Wanders RG, Wolfs C, Eekers D. Considerations for shoot-through FLASH proton therapy. Phys Med Biol. 2021;66(6).

44. Edwards C. Fundamental quantities and units for ionizing radiation (revised). ICRU report nº 85. J ICRU. 2011;11(1).

45. Bourhis J, Montay-Gruel P, Gonçalves Jorge P, Bailat C, Petit B, Ollivier J, et al. Clinical translation of FLASH radiotherapy: Why and how? Radiother Oncol [Internet]. 2019;139:11–7. Available from: https://doi.org/10.1016/j.radonc.2019.04.008

46. Wilson JD, Hammond EM, Higgins GS, Petersson K. Ultra-High Dose Rate (FLASH)

Radiotherapy: Silver Bullet or Fool's Gold? Front Oncol. 2020;1–12.

47. Harrington KJ. Ultrahigh dose-rate radiotherapy: Next steps for flash-RT. Clin Cancer Res. 2019;25(1):3–5.

48. Montay-gruel P, Acharya MM, Petersson K, Alikhani L, Yakkala C, Allen BD, et al. Long-term neurocognitive benefits of FLASH radiotherapy driven by reduced reactive oxygen species. Proc Natl Acad Sci U S A. 2019;117(41):25946–7.

49. Diffenderfer ES, Verginadis II, Kim MM, Shoniyozov K, Velalopoulou A, Goia D, et al. Design, Implementation, and in Vivo Validation of a Novel Proton FLASH Radiation Therapy System. Int J Radiat Oncol Biol Phys [Internet]. 2019;106(2):440–8. Available from: https://doi.org/10.1016/j.ijrobp.2019.10.049

50. IBA. Internal document.

51. Bossier V. IBA Proton Therapy [Internet]. 2015. Available from: http://homepages.ulb.ac.be/~odebeir/projh500/IBA_PT_Biomed_2015.pdf

52. Chang KP, Hsieh HH, Chao TC, Wu CH. Effects of modulation materials for lung dose distribution in proton therapy. Radiat Phys Chem [Internet]. 2020;167(April 2019):108264. Available from: https://doi.org/10.1016/j.radphyschem.2019.04.014

53. Safai S, Bula C, Meer D, Pedroni E. Improving the precision and performance of proton pencil beam scanning. Transl Cancer Res. 2012;1(3):196–206.

54. Amato E, Lizio D, Baldari S. Applications of the monte carlo method in medical physics. Med Phys. 2013;(March 2013):105–13.

55. Pelowitz DB, editor. MCNPX user's manual. Los Alamos National Laboratory; 2008. 1–551 p.

56. Hérault J, Iborra N, Serrano B, Chauvel P. Monte Carlo simulation of a protontherapy platform devoted to ocular melanoma. Med Phys. 2005;32(4):910–9.

57. Newhauser W, Koch N, Hummel S, Ziegler M, Titt U. Monte Carlo simulations of a nozzle for the treatment of ocular tumours with high-energy proton beams. Phys Med Biol. 2005;50(22):5229–49.

58. Smith H. Conversion Coefficients for use in Radiological Protection against External Radiation. ICRP Publication 74. Vol. 6, Annals of the ICRP. 1996.

59. Trinkl S, Mares V, Englbrecht FS, Wilkens JJ, Wielunski M, Parodi K, et al. Systematic out-of-field secondary neutron spectrometry and dosimetry in pencil beam scanning proton

therapy. Med Phys. 2016;44(5):1912–20.

60. Simeonov Y, Weber U, Schuy C, Engenhart-Cabillic R, Penchev P, Durante M, et al. Monte Carlo simulations and dose measurements of 2D range-modulators for scanned particle therapy. Z Med Phys [Internet]. 2021;31(2):203–14. Available from: https://doi.org/10.1016/j.zemedi.2020.06.008

61. Lindsay C, Kumlin J, Martinez DM, Jirasek A, Hoehr C. Design and application of 3D-printed stepless beam modulators in proton therapy. Phys Med Biol. 2016;61(11):N276–90.

62. Lindsay C, Kumlin J, Jirasek A, Lee R, Martinez DM, Schaffer P, et al. 3D printed plastics for beam modulation in proton therapy. Phys Med Biol. 2015;60(11):N231–40.

63. Ju SG, Kim MK, Hong CS, Kim JS, Han Y, Choi DH, et al. New technique for developing a proton range compensator with use of a 3-dimensional printer. Int J Radiat Oncol Biol Phys [Internet]. 2014;88(2):453–8. Available from: http://dx.doi.org/10.1016/j.ijrobp.2013.10.024

64. Ringbaek TP, Brons S, Naumann J, Ackermann B, Horn J, Latzel H, et al. Fluence inhomogeneities due to a ripple filter induced Moiré effect. Phys Med Biol. 2015;60(3):N59–69.

65. Ringbæk TP, Weber U, Petersen JB, Thomsen B, Bassler N. Monte Carlo simulations of new 2D ripple filters for particle therapy facilities. Acta Oncol (Madr). 2014;53(1):40–9.

66. The MathWorks I. Contour plot of a matrix [Internet]. [cited 2021 Jul 12]. Available from: https://uk.mathworks.com/help/matlab/ref/contour.html

67. International Commission on Radiological Protection (ICRP). Annals of the ICRP. Publication 103. The 2007 Recommendations of the International Commissionin on Radiological Protection. 2007.

68. Kry SF, Bednarz B, Howell RM, Dauer L, Followill D, Klein E, et al. AAPM TG 158: Measurement and calculation of doses outside the treated volume from external-beam radiation therapy. Med Phys. 2017;(10).

69. Schneider U, Hälg R. The impact of neutrons in clinical proton therapy. Front Oncol. 2015;(OCT).

70. Uozumi Y, Yamada T, Nakano M. Intranuclear cascade model for 50-MeV-region (p, p′x) reactions over a wide target mass range. J Nucl Sci Technol [Internet]. 2015;52(2):264–73. Available from: http://dx.doi.org/10.1080/00223131.2014.945505

13. Appendix 1

The objective of this appendix is to describe the calculations to obtain the results in mSv/Gy from the results units given by MCNPX, in MeV/g per source particle.

To calculate the effective dose in units of mSv/Gy it is necessary to specify a PTV volume and multiply for enough number of particles to give 1Gy in this volume. The PTV volume was specified in the Bragg peak region, for each simulation scenario, with a volume of $1 \times 1 \times 2 = 2\ cm^3$. A PTV cell was added in the MCNPX INP file and a F6 tally for this volume requested. The simulation was run, and the energy deposited at the PTV volume was accessed. The number of particles chosen for the simulations was 4×10^6 protons.

For the case of AISI4073, the result of the F6 tally was 8.58025×10^{-1} MeV/g per source particle. Following the formula presented at 2.4.1.1:

$$D = \frac{E}{m} = \frac{(8.58025 \times 10^{-1}) \times (1.6021 \times 10^{-13})\ J}{0.001\ kg} = \frac{1.37464 \times 10^{-13}\ J}{0.001\ kg} \quad (13.1)$$
$$= 1.37464 \times 10^{-10}\ Gy$$

After this calculation, it is known that 1 primary proton gives $1.37461 \times 10^{-10}\ Gy$ in the PTV volume, because the results of the F6 tally in MCNPX is given in MeV/g per source particle. After this, it is necessary to know how many particles are necessary to give 1 Gy in the PTV. Using a rule of three:

$$1\ particle \rightarrow 1.37461 \times 10^{-10}\ Gy \quad (13.2)$$
$$x\ particles \rightarrow 1\ Gy$$

$$x = \frac{1\ particle \times 1\ Gy}{1.37464 \times 10^{-10}\ Gy} = 7.275 \times 10^9\ particles \quad (13.3)$$

The graphs in mSv/Gy are obtained by multiplying the results in mSv/proton for $7.275 \times 10^9\ particles$.

The same calculations were performed for the remaining scenarios and the results are presented in Table 23.

Table 23 Calculation results for all the simulated scenarios, under the scope of chapter 10.2.1.

	F6 tally result (MeV/g per source particle)	Dose of 1 proton in the PTV (Gy)	Number of particles to give 1 Gy in the PTV
AISI4073 + RS	0.878661	1.408×10^{-10}	7.104×10^{9}
AISI7050	1.00589	1.61154×10^{-10}	6.2053×10^{9}
AISI7050 + RS	1.02722	1.64571×10^{-10}	6.0764×10^{9}
PMMA	1.12753	1.80642×10^{-10}	5.5358×10^{9}
PMMA +RS	1.13583	1.8197×10^{-10}	5.4954×10^{9}

14. Appendix 2

The objective of this appendix is to describe the calculations to obtain the results in mSv/Gy from the results units given by MCNPX, in MeV/g per source particle.

The calculations made follows the same formulae presented at annex 1. For this reason, the resultant values are presented in Table 24.

Table 24 Calculation results for all the simulated scenarios, under the scope of chapter 10.2.2.

	F6 tally result (MeV/g per source particle)	Dose of 1 proton in the PTV (Gy)	Number of particles to give 1 Gy in the PTV
CEF + RS	2.20974	3.5402×10^{-10}	2.8247×10^{9}
CEF + RS + brass block	1.81244	2.9037×10^{-10}	$3{,}4439 \times 10^{9}$

15. Appendix 3

The objective of this appendix is to describe the calculations to obtain the results in mSv/Gy from the results units given by MCNPX, in MeV/g per source particle.

The calculations made follows the same formulae presented at annex 1 and 2. For this reason, the resultant values are presented in Table 25.

Table 25 Calculation results for all the simulated scenarios, under the scope of chapter 10.2.3.

	F6 tally result (MeV/g per source particle)	Dose of 1 proton in the PTV (Gy)	Number of particles to give 1 Gy in the PTV
Scenario 1	1.73277	2.7761×10^{-10}	3.6022×10^{9}
Scenario 2	0.836331	1.3399×10^{-10}	7.4633×10^{9}